# FIELD EMISSION MICROSCOPY OF CARBON NANOTUBE FIBERS

Ву

Taha Yasin Posos

# A DISSERTATION

Submitted to
Michigan State University
in partial fulfillment of the requirements
for the degree of

Electrical Engineering—Doctor of Philosophy

2023

#### **ABSTRACT**

Large-area field emission cathodes made from carbon nanotube (CNT) fiber have long been promising as the next generation electron sources for high-power radio frequency (rf) or microwave vacuum electronic devices (VEDs). CNTs have excellent field emission properties such as low turn-on voltage and high output current at electric fields as low as ~10 MV/m, as compared to the legacy metal emitter technology. Therefore, CNT technology has the potential to decrease the operating voltage and simplify VED systems. However, in addition to high beam charge, beam-driven radiation sources require electron beams with low emittance (i.e. high brightness), which must be provided in a stable continuous fashion. Although there have been many studies on CNT fibers' emission current performance, there is not sufficient research on their emission uniformity, emittance, brightness, and overall upper performance limitations specific to the CNT material itself. The lack of these important characterization metrics led to the work presented in this thesis. Not only were the conventional current-voltage (I-V) relations measured and evaluated, but also the electron beams carrying the currents were monitored in situ in real-time by projecting the beam onto a scintillator screen in a custom field emission microscope. These enabled the measurement and evaluation of emittance and brightness. The existing bottlenecks limiting the fiber's performance were uncovered for the first time and new advanced CNT fiber cathode designs were proposed and engineered accordingly.

In Ch.2, various standard (previously attempted) designs of CNT fiber cathodes were tested in the field emission microscope. The results showed that all cathodes had high emittance, low brightness, a large beam spread, non-uniform emission, current saturation, and instability. Hot spots and microbreakdowns were observed during emission. Analysis of the data revealed that all these problems were due to the formation of stray emitters on the cathode surface during emission. It was concluded that the tested fibers failed to provide any reasonable beam quality regardless of the cathode geometry.

Exceptionally non-uniform current emission observed in the experiments raised the question about the mechanism of current saturation when the output charge failed to keep up with the increasing electric field. In Ch.3, a computational method was developed to extract the emission area from the emission micrographs and then calculate the emission current density. It was found that the current density saturated quickly and stopped obeying the Fowler-Nordheim law. It was demonstrated that the saturation effect occurred because the local current density reached a maximum level limited by the number of carriers and their finite transit time inside the bulk material's depletion region. It was concluded that overcoming the saturation issue is only possible if uniform emission can be achieved.

In Ch.4, a brand new and unique cathode design was developed that successfully solved all the problems caused by stray emitters. It was demonstrated that the new design provided a uniform and stable electron beam with a small divergence angle, resulting in a beam with low emittance and high brightness. This result is a significant advancement that outlines a feasible path toward utilizing CNT fiber electron sources for practical VED applications. More specifically, it was observed that the entire cathode surface of a radius of approximately 75  $\mu$ m emitted uniformly (with no hot spots) in the direction of the applied electric field. From this, the normalized dc current brightness was estimated as  $B_{\rm N} = 3.7 \times 10^{10} \frac{\rm A}{\rm m^2 rad^2}$  using the estimated emittance of 52 nm rad. From this, the brightness in the pulsed mode, the preferable mode in most VED HPM applications, was predicted to attain a notable value of  $B_{\rm N} = 4.4 \times 10^{15} \frac{\rm A}{\rm m^2 rad^2}$ .

Copyright by TAHA YASIN POSOS 2023 To Eminem, there is no me without you!

#### **ACKNOWLEDGEMENTS**

First of all, I would like to thank God for all the blessings He has bestowed upon me, which have led me to the completion of this thesis. I am thankful for His guidance, for igniting my curiosity, passion, and patience in the pursuit of science and knowledge, for giving me a wonderful family which supported me in every aspect of my life, and for making me meet with very valuable people at Michigan State University.

As humans, we are inherently weak, but through our collective efforts, we become stronger and achieve great things. I would like to thank all people who helped me throughout this journey and acknowledge their efforts.

I am deeply grateful to my advisor, Prof. Sergey Baryshev. This expression of gratitude is not merely a formal one, but a sincere acknowledgement. Prof. Baryshev has been more than just someone I could turn to for scientific questions and guidance. He has always been available to offer support and assistance in every aspect of life. He consistently strives to provide his students with the best opportunities to prepare them for their professional lives after graduation. His patience, calm demeanor, and kindness are truly remarkable. He has granted his students a great deal of freedom to develop their own ideas and become independent researchers. I have learned invaluable lessons from him. Most importantly, he has taught me that good work can only be achieved in an environment that fosters freedom, respect, grace, passion, and patience.

I would like to thank my wife Emine and our little kid Zeynep. Without them, I am nothing. Their smiles every morning have been a source of power and motivation for me. Although my extensive working hours limited the time I could spend with them, they have always supported me and forgiven me. Emine is not just my wife but also my lifelong friend and therapist. She has been by my side through every struggle. I would like to thank my parents and siblings as well. Their pray and support have always been with me.

I would also like to express my appreciation to all my labmates. Our lab is comprised of wonderful individuals in a supportive and nurturing environment. I would like to extend special thanks to Tanvi Nikhar for dedicating countless hours to conducting Raman measurements for my

samples, and Benjamin Sims for teaching me how to use GPT.

I collaborated with excellent people in other institutions as well. Specifically, I would like to thank Prof. Oksana Chubenko (Northern Illinois University) for her assistance with image processing, Dr. Steve Fairchild (Air Force Research Laboratory) for providing fibers, and Jack Cook (Cambridge University) for electroplating fibers.

# TABLE OF CONTENTS

LIST OF FIG	GURES	X
LIST OF AE	BBREVIATIONS	νi
1.1 1.2 1.3 1.4	Overview and Thesis Outline	1 2 6 7
2.1 2.2 2.3 2.4	EVALUATING AND INTERPRETING SPATIAL EMISSION OF CNT FIBERS	23 25 28
3.1 3.2 3.3 3.4 3.5	CONFIRMATION OF TRANSIT TIME-LIMITED FIELD EMISSION IN ADVANCED CARBON MATERIALS 4 Introduction 4 Experimental Methods 4 Image Processing Algorithm 4 Results and Discussion 5 Conclusions 6	-1 -3 -4
4.1 4.2 4.3 4.4 4.5	BRIGHT SPATIALLY COHERENT BEAM FROM ELECTROPLATED CNT FIBERS 6 Introduction 6 Experimental 6 Field Emission Imaging and Conditioning 6 Emittance and Brightness 7 Conclusion 7	3 5 6 7 0
CHAPTER 5 5.1 5.2	5 CONCLUSION AND OUTLOOK	1
RIBI IOGR	APHY 8	1

# LIST OF FIGURES

Figure 1.1	A diverging beam and its trace-space representation. When the particles in the diverging beam are plotted in the phase space of $x$ - $x'$ , they form a positive correlation. A converging beam would form a negative correlation, rotating 90 degrees in $x$ - $x'$	4
Figure 1.2	A comparison of the focusability between low and high emittance beams. To achieve a small spot size at the beam waist, the high emittance beam requires a strong lens with a shorter focal length. However, using a lens with a shorter focal length results in a wider beam divergence angle immediately after the focal point. In contrast, a low emittance beam can achieve the same spot size using a lens with a longer focal length, and maintain its small diameter of the waist order along longer distances after the focal point.	5
Figure 1.3	This power-frequency chart is comparing vacuum electron devices and solid-state devices [11]. At low frequencies and power, solid-state devices are preferred, whereas, at high frequencies and power, vacuum electron devices perform better	7
Figure 1.4	A vacuum triode. It consists of an electron emitter (cathode), a control grid, a collector (anode), and an antenna circuitry serving as the output load. The grid signal modulates the current flowing from the anode to the cathode, leading to amplification	8
Figure 1.5	A schematic of a two-cavity klystron. The gun generates an electron beam, which, after acceleration, undergoes velocity modulation in the buncher cavity when an input rf signal is applied to the buncher. The bunches are formed in drift space. The bunched beam radiates its energy coherently in the catcher cavity. The beam loses its energy to radiation and is simply dumped into the collector.	10
Figure 1.6	Linear vs helix transmission line. When an rf signal is applied to the linear line, it forms periodic high and low potential regions with the wavelength $\lambda$ alternating with time. The field around the wire has both longitudinal and transverse components. On the other hand, when a helical shape is formed from the linear line, the wavelength reduces to $\lambda_w$ , while the helical shape leads to a stronger longitudinal field at the center, as compared to the linear design	11
Figure 1.7	A simple traveling wave tube structure. The gun generates an electron beam and accelerates it to a certain energy. The beam then enters the helix. An input signal to be amplified is coupled into the helix wire, which results in bunching and deceleration of the beam, thereby causing the beam to radiate. The radiation amplifies the signal progressively. The beam with degraded energy is collected by the collector.	12

Figure 1.8	The red curve shows the phase of the helix wave along the central axis at a given time. The gray is the beam. The blue arrows indicate the direction of the forces. Initially, the beam is longitudinally uniform (dc). It is compressed by the wave into bunches. The bunches interact with the electrons inside the helix wire such that they settle at the decelerating phase of the signal. Because the wave and bunches travel at the same speed, the bunches are decelerated progressively. The beam converts its energy into radiation, which couples to the helix, and progressively amplifies the output signal	12
Figure 1.9	This schematic shows the operation of a free-electron laser. The inset image shows a zoomed view of a wiggle period. The electron beam generated by the gun reaches almost the speed of light in the accelerator, and then it is deflected to an undulator. Under the static undulator magnetic field, the beam makes a wiggle motion with the wavelength $\lambda_u$ (the red trajectory). The wiggling electrons emit synchrotron radiation with a wavelength $\lambda_r$ and a magnetic field $\vec{B}_x$ in the $\pm x$ direction (the blue wave). The magnetic field of the radiation and the wiggling motion creates longitudinal Lorentz forces $(\vec{F}_z = \mathbf{q}_e \vec{v}_y \times \vec{B}_x)$ , compressing the beam into bunches (the forces are shown by black arrows). The decelerating bunches radiate coherently. The radiation is transmitted to the output and partially reflected back by an optical cavity to reinforce the bunching. The beam with reduced energy is deflected to a beam dumper	14
Figure 1.10	Electrons inside the material are bound in the potential well and cannot be emitted into a vacuum. In field emission, a high potential is applied to the cathode so that the electrons can tunnel through the modified potential barrier. By ignoring the image-charge effect, the applied potential result in a triangular barrier with a profile given by $q_eFx$ where $q_e$ is the negative electron charge, $F$ is the electric field normal to the surface, and $x$ is the normal distance from the surface. A stronger field results in a thinner barrier, which leads to more emission. By solving the Schrodinger equation with the given profile, the current density of the emission can be calculated	17
Figure 1.11	By plotting experimental data that includes the applied field $F_a$ and the measured emission current $I$ in Fowler-Nordheim coordinates as shown in the plot, the filed enhancement factor $\beta$ can be found from the slope $\theta$	18
Figure 1.12	In this thesis, three main criteria were studied and used self-consistently to propose and engineer the most advanced CNT fiber cathodes to maximize their brightness	20

Figure 2.1	SEM images of sample A (flat cut sample), sample B (folded sample), sample C (wound geometry sample), and optical microscope image of sample D (looped sample). Bottom row: side camera views of samples A, B, C and top camera view of sample D when the samples are placed against the imaging YAG:Ce screen. All these images are taken before starting the experiments. There were no visible signs of unfolded stray fibrils on the samples	25
Figure 2.2	Experimental setup cartoon	27
Figure 2.3	Semilog $I$ - $E$ curves and FN plots for the studied fibers. The solid black curves show the difference between the set voltage of the electrometer ( $V_s$ ) and the actually measured feedback voltage ( $V_f$ ) applied to the sample. Horizontal black arrow indicates axis for the $V_s - V_f$ curve. Capital letter A is the flat cut sample, B is the folded sample, C is the wound geometry sample, and D is the looped sample. Small letter "b" corresponds to emission "before" initial conditioning, "a" corresponds to emission "after" the very last test run. Error bar regions for the dotted blue and solid red curves are shown in light blue and light red, respectively	29
Figure 2.4	Laterally resolved field emission pattern on YAG screen taken at the same electric field before and after conditioning for sample A $(0.67V/\mu m)$ , B $(0.72V/\mu m)$ , C $(0.36V/\mu m)$ , and D $(0.16V/\mu m)$ . The white dashed circles and line show actual position and orientation of the samples with respect to the YAG screen. The white arrows show the location of the red spot. The black arrows point at the halo. The outstanding image at the bottom (Ca2) illustrates the source of the halo background: it is a stray emitter pair projected to be nearly parallel to the screen plane thus generating electron rays that have long path across the screen resulting in intense halo	31
Figure 2.5	(a) Emission curve after noise reduction processing (solid blue), third order polynomial fitting (dashed red), deduced FN-like section of the $I$ - $E$ curve used for calculation of the $\beta$ -factor (dot-dashed black), zoom in view of the deduced FN-like section is shown in the inset plot. (b) The vector family used in the knee point calculation	33
Figure 2.6	Comparison of the emission area on the applied electric field for the folded sample B before conditioning, as extracted from <i>I-E</i> curves using the FN equation versus from the field emission micrograph dataset using an image processing algorithm (Ref.[35]) developed elsewhere	34
Figure 2.7	Demonstration of various types of unfolded and differently aligned stray CNT fibrils that are formed after conditioning breakdowns—all taken by the top-view camera, except for sample C, which was inspected by the side-view camera to reveal the origin of the red spot	37

Figure 2.8	Close-ups of emission patterns of sample A before and after the conditioning runs. The dashed line circles depict the actual fiber location with respect to the YAG screen. Solid line circles of the same diameter are to illustrate that major emission pattern fits within the size of the fiber even though there is a parallel shift caused by slight misalignment.	. 39
Figure 3.1	(A) Typical micrograph obtained from an UNCD film under the applied DC field [35]. A $450\times450\mathrm{px^2}$ image represents a projection of spatial distribution of electron emission sites onto a YAG anode placed $106\mu\mathrm{m}$ from a $4.4\mathrm{mm}$ -diameter cathode. The FOV seen in the micrograph is $4.4\times4.4\mathrm{mm^2}$ . (B) Detected LMs (shown with blue plus signs) overlaid with emission spots shown on the micrograph. (C) Emission pixels (shown in blue), which represent the projected emission area, overlaid with emission spots shown on the micrograph	. 45
Figure 3.2	(A) Decision plot of extracted features for the micrograph obtained from an UNCD cathode operated under the DC field. The unit of the distance is pixel (px), and the unit of the pixel value is arbitrary (a.u.). Green, black, and brown dashed regions show locations of LMs, background pixels, and emission pixels in the decision plot, respectively. There is no overlapping between an LM cluster and a uniform background. (B) The black curve shows the Gaussian decision boundary. The pixels shown in red are classified as LMs.	. 45
Figure 3.3	3D plot of the micrograph shown in Figure 3.1A. $i$ and $j$ axes are pixel coordinates, and the $p$ axis is for the pixel value	. 46
Figure 3.4	(A) Typical micrograph obtained from a CNT fiber under the DC field. The FOV seen in the micrograph is $12.4 \times 12.4 \mathrm{mm^2}$ . (B) Detected LMs (shown with blue plus signs) overlaid with emission spots shown on the micrograph. (C) Emission pixels (shown in blue), representing the projected emission area, overlaid with emission spots shown on the micrograph	. 48
Figure 3.5	(A) Decision plot of extracted features for the micrograph obtained from a CNT fiber under the DC field. Green, black, and brown dashed regions show locations of LMs, background pixels, and emission pixels, respectively. The red dashed region shows overlapping between LMs and a background cluster. (B) The black curve is the applied Gaussian decision boundary. Red points are detected LMs. Notice that not all points above the boundary are red; this is because some false LMs were filtered out.	. 48

Figure 3.6	Typical micrograph obtained from a CNT fiber under the DC field with a glowing high-gradient background. The emission domains appear as bright peaks on the glow. The exact source of the glow is unknown. The FOV seen in the micrograph is $11.2 \times 11.2 \mathrm{mm}^2$ . (B) Detected LMs (shown with blue plus signs) overlaid with emission spots shown on the micrograph. (C) Emission pixels (shown in blue), representing the projected emission area, overlaid with emission spots shown on the micrograph	53
Figure 3.7	(A) Decision plot of extracted features for the micrograph obtained from a CNT fiber under the DC field with a glowing high-gradient background. Unlike the previous cases, the background does not form a cluster. Instead, it is distributed over a wide pixel range shown in a black dashed region. The green dashed region consists of well-separated LMs. The red region includes both background pixels and LMs, so the boundary should be drawn so that the region includes all candidate LMs. Any false LMs are to be filtered out by Gaussian surface fitting. (B) A black curve shows the applied decision boundary. All points above the curve are candidate LMs. Red points label the finalized LM list after false LMs are filtered out by the surface fitting	53
Figure 3.8	(A) SEM image of the UNCD film grown on a Ni/Mo/SS substrate. (B) SEM image of the CNT fiber. The twisted and folded yarn structure is clear from the image	54
Figure 3.9	Apparent emission area estimated using the algorithm (blue dots) and the measured current (red dots) as a function of the applied electric field (A) for the UNCD film, (B) for the CNT fiber before conditioning, and (C) for the CNT fiber after conditioning	55
Figure 3.10	Experimental current densities (the lower limit is shown with green dots; the upper limit is shown with blue dots) compared with the theoretical estimations (the elementary FN equation is shown with magenta dots; the MG extension is shown with cyan dots) and the space charge limited emission (dashed red line) and the transit time-limited emission (dashed orange line) as a function of the applied electric field (A) for the UNCD film, (B) for the CNT fiber before conditioning, and (C) for the CNT fiber after conditioning	56
Figure 4.1	Typical micrograph showing large beam transverse spread and nonuniformity. The blue circle marks the cathode's position behind the imaging screen and its size.	64
Figure 4.2	(A) Raman spectra of the cathode surface showing a crystalline graphitic peak. (B) Electroplated CNT fiber welded on a Ni base; H=4.8 mm for Sample A and H=4.6 mm for Sample B. (C) and (D) SEM images of Sample A and Sample B, where scale bars are $50 \mu m. \dots \dots \dots \dots \dots \dots \dots$	66

Figure 4.3	This is an illustration of the measurement setup. The coated fiber cathode was mounted across a scintillator anode screen made of yttrium aluminum garnet (YAG). The screen was biased positively, and the cathode and body of the vacuum chamber were grounded. The emitted electrons, under the applied field, struck the screen, which formed emission micrographs. The micrographs were captured by a camera behind the screen. The emission current and feedback voltage were recorded. All data acquisition was done synchronously and automatically by computer control.	67
Figure 4.4	A) Sample A seen through the YAG screen when the lights are on in the chamber. Its fiber core is marked with a red circle (the shiny gray region is the metal shell, and the darker center is the core). B) FE micrograph of the same region at the gap of $200  \mu \text{m}$	68
Figure 4.5	A) Sample B seen through the YAG screen when the lights are on in the chamber. Its fiber core is marked with a red circle. B) FE micrograph of the same region at the gap of $200  \mu \text{m}$	68
Figure 4.6	A) The conditioning scheme of Sample A. Both ramp up and down curves are shown. There is a clear decrease in performance. B) Conditioning scheme of Sample B. Only ramp-up curves are shown. There is no considerable change in performance.	69
Figure 4.7	Series of field emission micrographs of Sample B with the screen moved away progressively from $200 \mu\text{m}$ gap to $1600 \mu\text{m}$ gap with $200 \mu\text{m}$ steps. At each step, a micrograph is captured	71
Figure 4.8	The color surface shows the beam spot for $200 \mu\text{m}$ gap in 3D. The black mesh surface shows its mathematical fit in Eq.4.7	73
Figure 4.9	Comparison of experimental and computational final beam spot size as the screen is moving away from the cathode. MTE <sub>i</sub> of 250 meV and $r_i$ of 75 $\mu$ m were used in GPT modeling	73
Figure 4.10	Illustration of electric field computed in COMSOL for a 1 mm gap. The color plot shows the field magnitude and contour. The dark region is the fiber core, and the gray region is the Ni shell.	73
Figure 4.11	In GPT: (A) Initial uniform beam distribution at the cathode surface in real space, where $r_i$ is the radius of the beam. (B) The initial distribution in momentum-space, where $\beta_x = v_x/c$ , $\beta_y = v_y/c$ , and $r_\beta$ is the radius. Final distribution in (C) real space and (D) momentum space when the screen is at	71
	1 mm	74

Figure 5.1	ness are interconnected. Non-uniform emission leads to a local high current density, which eventually results in current saturation, local heating, breakdowns, and unstable performance. Emission non-uniformity was caused by the formation of stray emitters, which enhanced the radial field and increased	77
Figure 5.2	The plots show the radial and normal surface fields right above the cathode for different Ni shell thicknesses. A) The solid red line indicates the line where the fields were plotted, which extends from the center axis to the edge of the fiber core. $T_{\text{shell}}$ represents the thickness of the Ni shell. B) It shows the radial field $E_r$ over the surface, with $r$ denoting the distance from the center axis of the fiber. Doubling the shell thickness results in a five-fold decrease in the radial field $E_r$ on the surface. C) It shows the normal field $E_z$ over the	
	surface	81

# LIST OF ABBREVIATIONS

**CNT** Carbon nanotube fiber

YAG Yttrium aluminum garnet

**MWT** Microwave tube

**FEL** Free-electron laser

rf Radio-frequency

MTE Mean transverse energy

**RMS** Root mean square

**FET** Field-effect transistor

#### CHAPTER 1

#### INTRODUCTION

#### 1.1 Overview and Thesis Outline

This thesis researches carbon nanotube (CNT) fiber field electron emitters made using state-of-the-art technologies. Their emission properties were studied, the underlying physics was thoroughly understood, performance limitations were realistically identified, and finally, visionary designs were proposed and demonstrated that can potentially be reduced to practice as future electron sources for the next generation of free electron X-ray and microwave sources. A motivating starting question was "Can CNT electron sources provide a beam quality that is good enough to allow high charge beams to be transmitted through millimeter apertures and/or over kilometer length scales?"

The field electron emitter releases free electrons into vacuum when a strong electric field is applied. CNT fibers attract particular attention from many researchers because of their excellent field emission properties: CNTs (in general) and fibers made thereof have low turn-on voltage/field, emit high charge even at low fields, and inherently have high electrical and thermal conductivities. Due to their high aspect ratio form factor, they naturally enhance the applied electric field, acting as an antenna (when placed in a parallel capacitor). CNT fibers are light and flexible, allowing for manufacturing large-scale high-power integrated circuits. However, these properties, while necessary, are not enough to make CNT fiber a perfect choice for high-power radiation sources. Studies on CNT fibers in the literature primarily focused on how much current they could provide at as low a voltage as possible through analyzing their I-V (current-voltage) curves. At the same time, studies of their spatio-temporal emission properties, such as transverse emittance and uniformity, and longitudinal energy spread, and hence the resulting brightness—which is the key figure of merit of any electron source for high-power rf applications—are scarce in the literature. Additionally, current saturation behavior was observed for CNT. This is when their current stops growing with the applied voltage/field. Because this effect is universal and lacks fundamental understanding, it casts a shadow on the future high current applications of CNT.

In this thesis project, emitted beam imaging using a custom-made field emission microscopy

setup [1], along with conventional I-V curves, was analyzed. This allowed for observation and measurement of transverse beam spread, emission angle, spatial coherence, and emission uniformity, and, from that, quantification of emittance, brightness, and mean transverse energy. In Ch 2, a series of initially promising CNT emitter designs were evaluated. It was discovered that the emission produced by the initial cathode designs was non-uniform regardless of its design, that is, a limited number of randomly distributed spots were actively emitting electrons. The cathodes also emitted off-axis with a very large beam spread and demonstrated current saturation at high applied fields. It was found that tiny stray fibrils emerged during emission even at relatively low fields. It was concluded that the described active spots were, in fact, loose isolated CNT fibrils. Acting like point-like sources of electrons, they led to non-uniform emission with a large beam spread and various additional anomalies seen in I-V curves. In Ch 3, by considering bulk CNT material properties, the underlying physics of the saturation effect and its connection to local emission spots were studied and understood. To compute local current densities from the sets of hundreds of micrographs, a fast and efficient image processing algorithm was developed. This allowed for comparing experimental and theoretical current densities, which led to a discovery that local current/charge density emitted from the active spots saturates at the levels limited by the depletion i.e. by the transit time of a given carrier concentration moving at the saturated drift velocity. Based on the obtained observations and results, in Ch 4 a new cathode design was proposed and engineered successfully that had orders of magnitude improved emission uniformity and brightness. The new design was a CNT core/nickel shell flat cut with a laser. The metal provided strong mechanical support, which halted the stray fibril unfolding issue experienced before.

### **1.2** Important Electron Beam Parameters

While it is fairly easy to design a cathode that would emit free electrons, not every such beam is practically useful when there is a need for directed energy applications. One could compare an incandescent bulb emitting light of a range of wavelengths in all directions, creating a low spatio-temporal power density, and a laser that focuses all the energy in one direction at a singular wavelength. High power high frequency devices can only benefit from using free electrons if specific

requirements are met. In this section, the terminology for the most important beam qualities is established to be used for the remainder of this thesis.

## 1.2.1 Beam Energy

Beam energy refers to the longitudinal kinetic energy of the electron beam. When the beam is accelerated under the action of an applied field force, it gains energy. Higher energy results in higher power gain and higher frequency in beam-driven microwave radiation sources. With the accelerating gradient, measured in MeV per meter, being the figure of merit, there is a trade-off between the voltage and the length of the vacuum power device. High gradients are limited by rf-induced plasma breakdown [2], while longer tubes are bulky and costly. Because both device concepts, whether they have high gradient or extended length, degrade the beam brightness via different mechanisms, the initial beam emittance (or tightness), a product of the emitter spot size and the angular divergence, must be kept as low as possible. [3].

## 1.2.2 Energy Spread

When electrons leave the emitter surface, they do not have the same energy, i.e due to 1) statistical variations, 2) external field transverse and longitudinal nonuniformities as well as 3) the non-stationary nature of the external fields. All these factors result in an electron energy distribution in the beam, referred to as the energy spread. The energy spread is a measure of beam quality in beam-driven radiation sources, and thus, affects the extracted power and frequency response. Compared to thermionic emission and photoemission, field emission tends to have the lowest energy spread because, statistically, most of the electrons are emitted near the Fermi level.

### 1.2.3 Emittance and Brightness

In beam-driven radiation sources, an intense electron beam must be transported through a series of apertures along a beamline, consisting of optics lattice, while maintaining minimal transverse growth to minimize the beam loss and generate radiation most efficiently [4]. Here, the transverse emittance and brightness serve as the figures of merit [5]. Emittance is proportional to the area formed by an ensemble of beam particles in trace space. The direction of beam propagation is

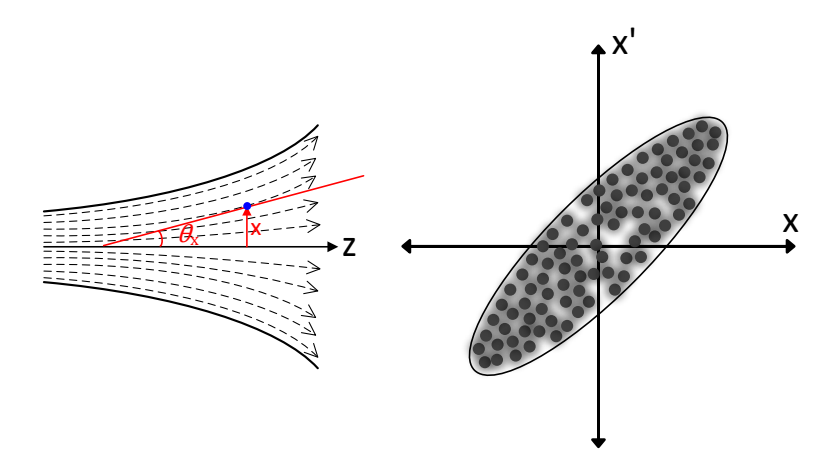


Figure 1.1 A diverging beam and its trace-space representation. When the particles in the diverging beam are plotted in the phase space of x-x', they form a positive correlation. A converging beam would form a negative correlation, rotating 90 degrees in x-x'.

defined as the longitudinal direction, denoted as z by convention, and x and y are referred to as transverse directions. In the x trace space, each particle is represented by (x, x') pair where x is the x-coordinate and  $x' = v_x/v_z$  is the angle of the x trajectory from the longitudinal axis. An example distribution for a diverging beam is shown in Fig.1.1. RMS x-emittance  $\tilde{\epsilon}_x$  is given by:

$$\tilde{\epsilon}_x = \sqrt{\langle \Delta x^2 \rangle \langle \Delta x'^2 \rangle - \langle \Delta x \Delta x' \rangle} \tag{1.1}$$

The calculation for *y*-emittance is identical to that for the *x*-emittance. Lower emittance results in better beam transport. Emittance also affects the size of the beam waist at a certain distance from a focusing device, with lower emittance allowing the beam to maintain its minimal waist size over longer distances [6]. Therefore, emittance determines the overall complexity of the optical element lattice. An illustration that captures these aforementioned points is presented in Fig.1.2. In many cases, what really matters is how much charge can be transported through many small apertures. This is captured by the parameter of brightness, taking charge and emittance, given by

$$B = \frac{2I}{\tilde{\epsilon}_x \, \tilde{\epsilon}_y} \tag{1.2}$$

A bright beam is an intense beam with a small radius, which can be collimated and focused well.

Emittance and brightness also have normalized versions given as

$$\epsilon_x^{\rm N} = \gamma \,\beta \,\tilde{\epsilon}_x \tag{1.3}$$

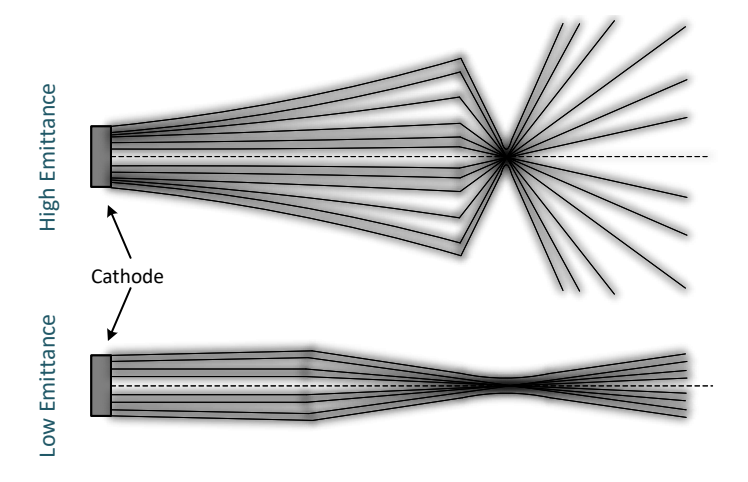


Figure 1.2 A comparison of the focusability between low and high emittance beams. To achieve a small spot size at the beam waist, the high emittance beam requires a strong lens with a shorter focal length. However, using a lens with a shorter focal length results in a wider beam divergence angle immediately after the focal point. In contrast, a low emittance beam can achieve the same spot size using a lens with a longer focal length, and maintain its small diameter of the waist order along longer distances after the focal point.

$$B_{\rm N} = \frac{2I}{\epsilon_{\rm x}^{\rm N} \, \epsilon_{\rm y}^{\rm N}} \tag{1.4}$$

where  $\gamma = \frac{1}{\sqrt{1-\beta^2}}$  is the Lorentz factor and  $\beta = \frac{v}{c} \approx \frac{v_z}{c}$ . The trace space can be manipulated with proper electron optics that utilize magnetic or electrostatic lenses to focus, deflect, etc. However, according to Liouville's theorem [7], normalized emittance and normalized brightness are conserved quantities as long as the beam is only subjected to conservative forces. For example, if the beam is focused with a strong lens, trace space contracts in x, but expands in x' such that the normalized area is always constant. Hence, it is critical to note that the beam must be of the highest quality, i.e. have the smallest area in the trace space, as the beam is emitted from the cathode surface. The beam emittance may worsen due to space charge [8], or the beam may lose charge along the beam pipe, but the qualities cannot be improved with any beam manipulation. So, whatever trace-space area is obtained on the cathode surface will be the measure of the best quality of the beam for the rest of its travel along the power device. This emphasizes the critical importance of cathode science.

## 1.3 High-Power Vacuum Electron Devices

To further emphasize the importance of beam emittance and brightness, some contemporary applications exploiting the free electron beam are reviewed.

It is known, for spherical waves, the radiation power drops with the square of the distance from the source. In addition, the absorption along the transmission medium causes additional power loss. Therefore, for sending high-frequency signals over long distances (such as in satellite communication, TV and radio transmitters, and radars), the output power of the transmitter needs to be as high as possible. Amplification of the signal can be achieved through either microwave tubes (a category of vacuum electron devices), which utilizes a free electron beam, or solid-state power amplifiers.

Although solid-state power devices are under extensive research, their frequency response is limited by the finite transit time of electrons. In a field-effect transistor (FET), if the gate signal is switched at a very high frequency, the carriers in the channel will not be able to drain fast enough due to the finite transit time, thereby attenuating the signal reaching the high-frequency bandwidth corner. To increase frequency response, the channel between the source and the drain must be as short as possible to allow for faster switching. However, smaller devices have lower power ratings, so there is a trade-off between power and frequency [9]. Increasing operating frequency and power at the same time is a great challenge for solid-state devices.

On the other hand, it is possible to obtain high frequency and high power at the same time with microwave tubes (MWTs). Although MWT devices vary in many nuances of their designs, the fundamental principle is common: MWT converts the kinetic energy of the free electron beam into radiation. The mechanism behind generating this radiation is "bunching". When a continuous stream of electrons interacts with an rf signal, depending on the phase of the signal, some of the electrons slow down and the others speed up, resulting in so-called velocity modulation. When the faster electrons catch up with the slower ones, it creates periodic bunches with the wavelength of the input signal. The bunched beam radiates coherently and constructively with the input signal, hence the input signal is amplified. It is also possible to recycle the bunched beam and re-interact

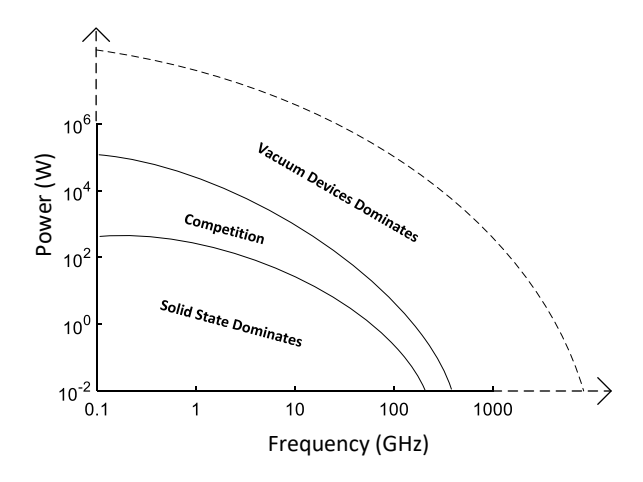


Figure 1.3 This power-frequency chart is comparing vacuum electron devices and solid-state devices [11]. At low frequencies and power, solid-state devices are preferred, whereas, at high frequencies and power, vacuum electron devices perform better.

it with the amplified signal and, therefore, produce even higher radiation power. In MWTs, unlike solid-state amplifiers, the output radiation is not created after collected electrons interact with an antenna load. Instead, microwave energy is radiated on-flight, i.e. as the beam travels along the device. So, the finite transit time, limiting the frequency response of the FET, does not hinder MWT performance [10]. MWTs are also more resilient to environmental effects like noise and heat. Heat especially can have a drastic effect on the operation point of solid-state devices [11]. Fig.1.3 shows a power-frequency chart comparing vacuum and solid-state electronic devices. At low frequencies and power, solid-state ones are the preferred choice due to their low power consumption and small size.

Although the transit time is not an issue in MWTs, transverse and longitudinal effects linked to emittance, brightness, and energy spread limit their performance. To demonstrate these factors and effects and give a comprehensive understanding of the required beam qualities, a few real vacuum electron devices are presented below.

### 1.3.1 Vacuum Triode

A vacuum triode cannot be classified as a microwave tube. However, as an ancestor of both MWTs and solid-state amplifiers, it formed a technological basis for the electronic revolution. It is the first practical amplifier to transmit and receive radio signals.

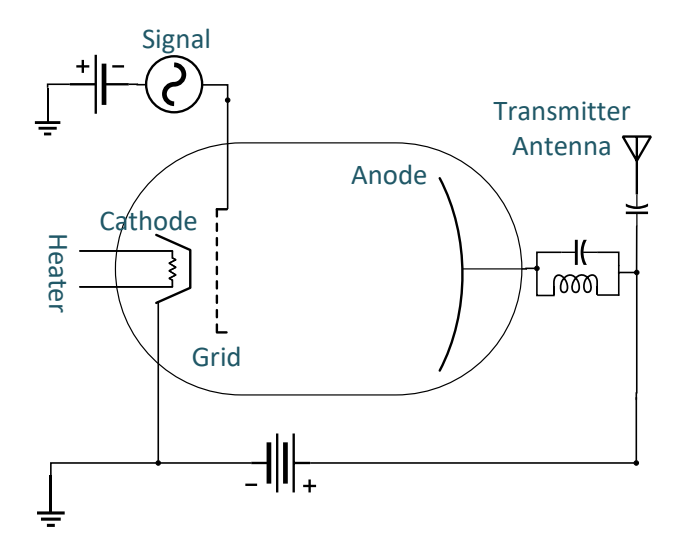


Figure 1.4 A vacuum triode. It consists of an electron emitter (cathode), a control grid, a collector (anode), and an antenna circuitry serving as the output load. The grid signal modulates the current flowing from the anode to the cathode, leading to amplification.

Like MWTs, the vacuum triode utilizes a stream of free electrons for amplification. Fig.1.4 shows a simple diagram of a vacuum triode. On the cathode side, either a Tungsten (W) or Carbon (C) filament is heated. The electrons on the surface of the heated cathode gain enough energy to overcome the potential barrier and become free electrons in vacuum. When the anode is biased positively, the electrons move from the cathode to the anode under the electric field, creating a steady DC current. The control grid in Fig.1.4 is placed close to the cathode. When a small rf signal is applied to it, the grid modulates the current flowing between the anode and the cathode, amplifying the signal. The anode collects the modulated current. Its energy is radiated through the antenna. A vacuum triode is similar to a JFET in that JFET modulates the current through its channel by changing the channel resistance with the gate signal. Unlike MWT, a vacuum triode produces usable radiation only after the beam is collected.

Since electrons in vacuum move much faster than the saturated drift velocity in the semiconductor, the vacuum triode enables faster switching of a higher power signal as compared to the field-effect transistor (FET). Still, triodes suffer from the transit time limitation, meaning that if the grid signal changes phase very quickly, the modulated current is not able to reach the anode before the next phase change [10]. Instead, it drains through the grid. As a result, the triode behaves as an

attenuator at very high frequencies. Increasing the potential of the anode could potentially alleviate this issue, but triodes are typically set to operate at a space-charge limited current for stability, so increasing the potential does not significantly increase the current due to field screening [12]. Built-in electrode capacitance and inductance also limit the frequency response of the triode, and radiation losses and heat dissipation problems further reduce its efficiency [10].

### 1.3.2 Klystron

Another technological breakthrough happened with the invention of the klystron. It was the first significantly powerful microwave tube for the amplification of radio signals. Fig.1.5 shows a schematic of a two-cavity klystron. Both cavities have a hole in the center to allow the electron beam to pass through. Once a voltage is applied to the anode of the gun, the heated cathode emits a DC stream of electrons. A small input signal to be amplified is fed into the buncher cavity. The signal forms a standing wave in the cavity so that the peak electric field occurs at the center, parallel to the beam path. The electron stream interacts with the wave while passing through the buncher cavity. For half of the signal period, the electric field opposes the beam, so it slows down. For the remaining half, the field is along the beam, so it speeds up. This again leads to velocity modulation. Velocity modulation causes a periodic variation in electron density. The modulated beam enters the drift space between cavities. In the drift space, faster electrons catch up with the slower ones, creating a periodically bunched beam. The period of the bunches is the same as the input signal. The catcher cavity is positioned where the bunch charge modulation contrast reaches its maximum. As the bunches pass through the catcher cavity, they induce an electromagnetic field with the frequency of the input signal. The induced signal creates another standing wave in the catcher cavity such that the field is always at an opposing phase as the bunches pass through, thus decelerating the bunches. The decelerated bunches radiate their energy, promoting further standing waves [13]. The beam with reduced energy is captured by the collector. The stored energy in the catcher cavity is coupled out through a coaxial cable. It is also possible to put a third idle cavity between the buncher and the catcher to reinforce bunching and increase power output. Klystrons are narrowband devices because the cavities, being RLC resonators, have a certain shape and can

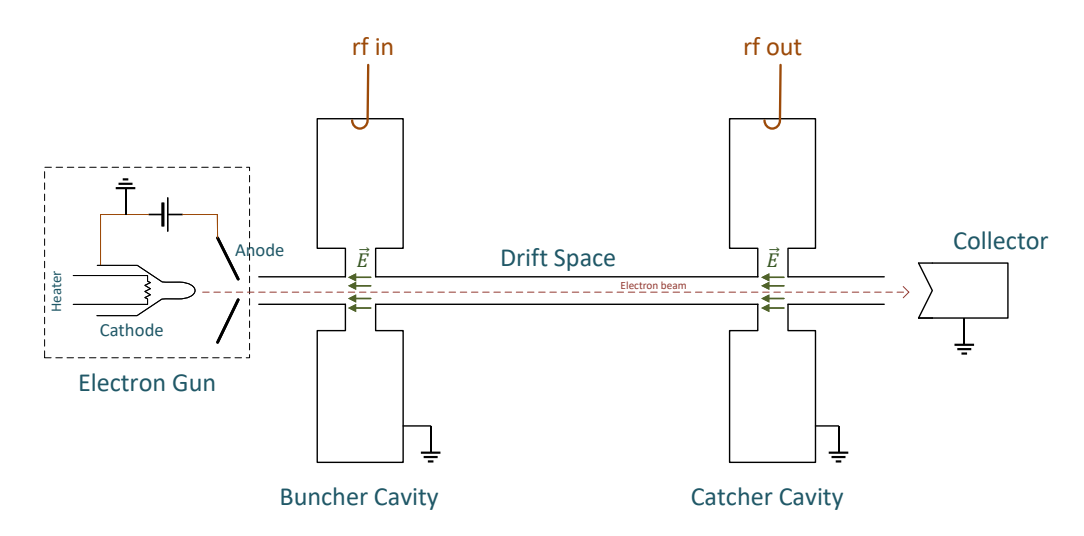


Figure 1.5 A schematic of a two-cavity klystron. The gun generates an electron beam, which, after acceleration, undergoes velocity modulation in the buncher cavity when an input rf signal is applied to the buncher. The bunches are formed in drift space. The bunched beam radiates its energy coherently in the catcher cavity. The beam loses its energy to radiation and is simply dumped into the collector.

only resonate with a reasonable loss for a limited frequency range.

For proper operation, the electron beam must meet several conditions: (1) The beam must have a small diameter and travel on the central axis with minimal transverse spread along the beam pipe, implying low emittance. A small beam diameter enables beam-peak field interaction through the cavity holes. It also reduces the higher harmonics, thus reducing noise. The minimal spread enables beam transport without losing charge between the cavities. (2) The beam must carry a high charge/high current, implying high brightness. A higher charge per bunch increases power output. (3) The beam must have a low energy spread. A lower energy spread of the beam leads to the best bunching and, hence, enables the highest radiation intensity and best signal-to-noise ratio.

The requirements for emittance and brightness are more stringent to amplify higher-frequency signals. This is because the cavities must be smaller (as a rule of thumb, the cavity size scales as  $1/f_c$ , where  $f_c$  is its resonance frequency). Therefore, in modern systems operating in X-band and above, the beam diameter must be in millimeters, with the transverse spread along the beam pipe being in the range of 10s–100s of microns.

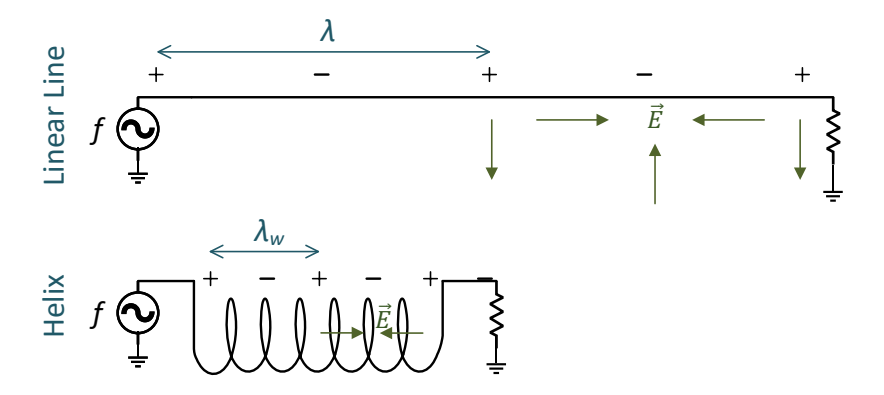


Figure 1.6 Linear vs helix transmission line. When an rf signal is applied to the linear line, it forms periodic high and low potential regions with the wavelength  $\lambda$  alternating with time. The field around the wire has both longitudinal and transverse components. On the other hand, when a helical shape is formed from the linear line, the wavelength reduces to  $\lambda_w$ , while the helical shape leads to a stronger longitudinal field at the center, as compared to the linear design.

## **1.3.3** Traveling Wave Tube (TWT)

Traveling wave tube amplifiers (TWTAs) are the most common power devices used in satellite communication. The core of any TWT consists of a helical wire through which the electron beam travels. To understand the function of the helical wire, refer to Fig.1.6. When an rf input is applied to the line, it creates periodic high and low potential regions that alternate with time. Since the rf wave travels at the speed of light inside a conductor, the distance between two same phases is simply  $\lambda = cT$ , where T is the period of the input signal. When a helix is formed from the same wire in Fig.1.6, two things happen [11]: (1) The helix's center axis is referred to as longitudinal direction. In the longitudinal direction, the distance between two same phases is  $\lambda_w = v_p T$ , where  $v_p$  is the phase velocity. As shown in the figure,  $\lambda > \lambda_w$ , so  $v_p < c$ , which means that in the helix, the phase travels a shorter distance in the longitudinal direction at the same signal period, so the phase velocity is lower. This structure is referred to as the slow-wave structure. (2) Forming the helix also changes the field direction. If one linear wavelength is divided by an integer number of helix turns, it creates a strong longitudinal electric field inside the helix (Fig.1.6).

In Fig.1.7, an input signal to be amplified is applied to the helix wire, creating a longitudinal electric field at the central axis of the helix. In the electron gun, a cathode emits free electrons, which are accelerated to an energy level so that the velocity of the beam matches the phase velocity

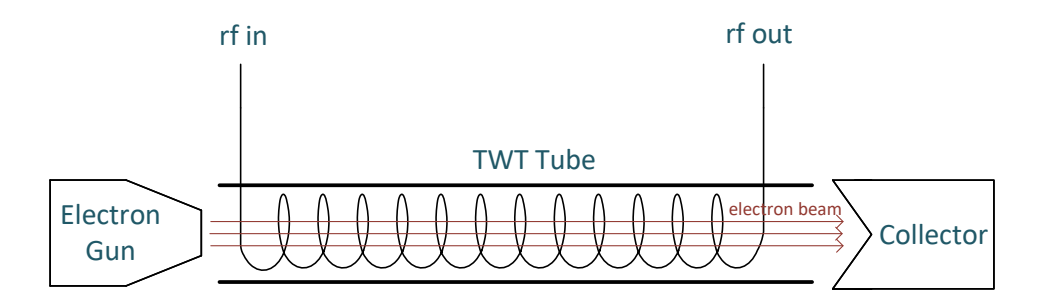


Figure 1.7 A simple traveling wave tube structure. The gun generates an electron beam and accelerates it to a certain energy. The beam then enters the helix. An input signal to be amplified is coupled into the helix wire, which results in bunching and deceleration of the beam, thereby causing the beam to radiate. The radiation amplifies the signal progressively. The beam with degraded energy is collected by the collector.

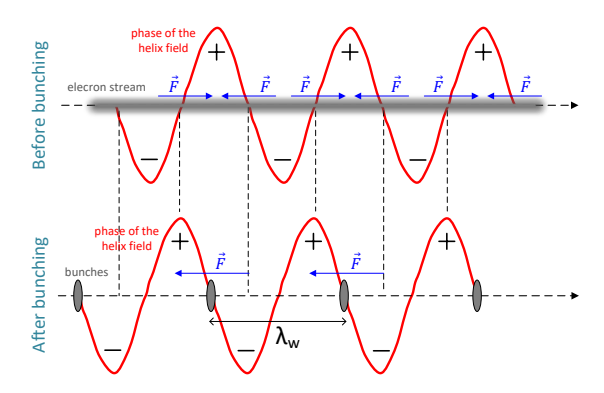


Figure 1.8 The red curve shows the phase of the helix wave along the central axis at a given time. The gray is the beam. The blue arrows indicate the direction of the forces. Initially, the beam is longitudinally uniform (dc). It is compressed by the wave into bunches. The bunches interact with the electrons inside the helix wire such that they settle at the decelerating phase of the signal. Because the wave and bunches travel at the same speed, the bunches are decelerated progressively. The beam converts its energy into radiation, which couples to the helix, and progressively amplifies the output signal.

of the wave on the helix's axis. The gun voltage can be fine-tuned for this purpose. The beam exiting the gun drifts toward the helix and enters the helix with a constant velocity. Initially, the beam is longitudinally uniform, as shown in Fig.1.8. Because the wave and beam have similar velocities, they travel alongside each other so that the forces in Fig.1.8 compress the beam into bunches continuously. As the bunches form, they also repel the electrons inside the helix wire, causing the phase of the wave to shift by  $\pi/2$  radians [11]. Eventually, the bunches set onto the decelerating phase of the wave as shown in Fig.1.8. Progressively, bunches decelerate through radiating, which couples constructively with the input signal, thereby, amplifying the signal at the output. The bunches with reduced energy are dumped in the collector (Fig. 1.7). If the wave traveled faster than the bunches, some bunches would accelerate while others decelerate, resulting in no net radiation. Unlike in the klystron, in TWT, the beam-wave interaction occurs along the entire length of the tube and does not require an extra drift space. Thus, TWT can be built at a much smaller footprint as compared to klystron. TWTs are also very wide band devices as they do not have fixed cavities like klystron, being a traveling wave device with a smaller quality factor. Although the power gain of a TWT is very high, maximum power is limited by the total current that can be passed through the helix.

For proper operation, (1) The beam divergence angle must be minimal so that the electrons do not escape along the helix (low emittance!); (2) The beam diameter must be small to enable efficient beam-wave interaction, as the strongest field is at the central axis; (3) The beam must carry a high charge/current. The higher the charge, the higher the current, and the higher the output power; (4) The energy spread must be small to improve bunch quality and reduce noise from higher harmonic waves. These requirements become more and more stringent as the helix diameter reduces to support higher frequency operation. For higher operating frequencies (shorter wavelengths), the helix is shorter and smaller in diameter requiring ever-growing brightness through ever-lowering emittance.

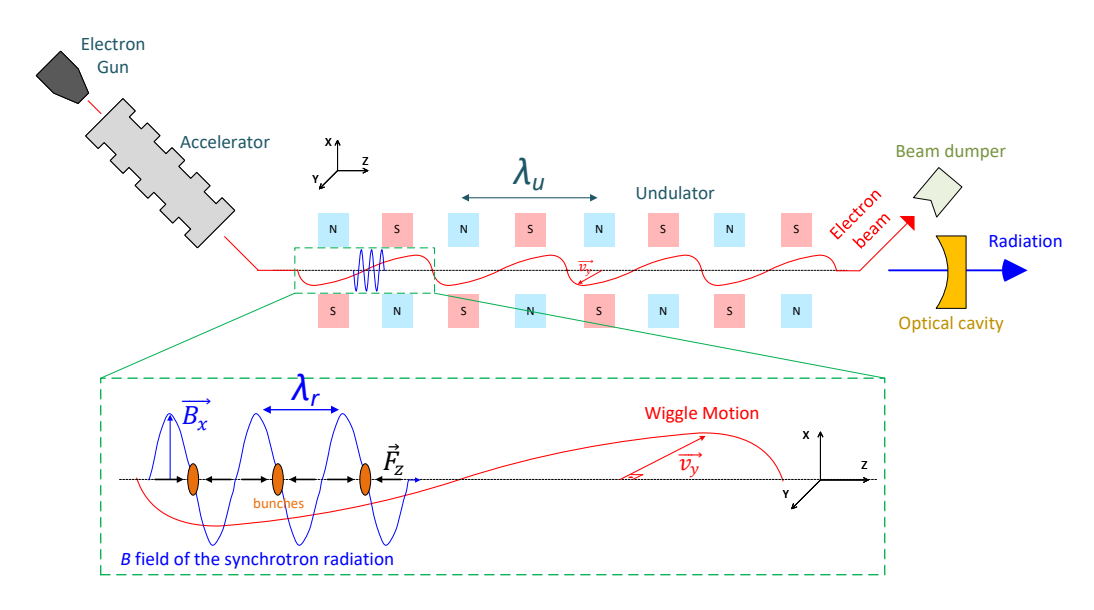


Figure 1.9 This schematic shows the operation of a free-electron laser. The inset image shows a zoomed view of a wiggle period. The electron beam generated by the gun reaches almost the speed of light in the accelerator, and then it is deflected to an undulator. Under the static undulator magnetic field, the beam makes a wiggle motion with the wavelength  $\lambda_u$  (the red trajectory). The wiggling electrons emit synchrotron radiation with a wavelength  $\lambda_r$  and a magnetic field  $\vec{B}_x$  in the  $\pm x$  direction (the blue wave). The magnetic field of the radiation and the wiggling motion creates longitudinal Lorentz forces ( $\vec{F}_z = \mathbf{q}_e \vec{v}_y \times \vec{B}_x$ ), compressing the beam into bunches (the forces are shown by black arrows). The decelerating bunches radiate coherently. The radiation is transmitted to the output and partially reflected back by an optical cavity to reinforce the bunching. The beam with reduced energy is deflected to a beam dumper.

### 1.3.4 Free-Electron Laser (FEL)

As the name suggests, a free-electron laser is a collimated monochromatic light source like other lasers. But, it utilizes a free electron beam as a gain medium instead of stimulated atomic excitation. It can provide extremely brilliant pulsed radiation at very high frequencies and powers which are not possible with conventional lasers otherwise. In this section, only oscillator FEL is presented, not the amplifying one [14]. The purpose of an oscillator is to generate the signal itself, not to amplify a given input signal.

The core of an FEL consists of an undulator and a free electron beam passing through it. An undulator is a periodic arrangement of dipole magnets. In Fig.1.9, the longitudinal central axis of the undulator is the z axis. The distance between two magnets with the same orientations is  $\lambda_{\rm u}$ , so the undulator creates a static magnetic field at  $\pm x$  direction with the wavelength  $\lambda_{\rm u}$ . In

Fig. 1.9, the free electron beam generated by the electron gun enters an accelerator, where it reaches almost the speed of light. Then, it is deflected to the central axis of the undulator. Before entering the undulator, the beam propagates with a constant velocity  $\vec{v}_z$ . Once it enters the undulator,  $\vec{v}_z$ and the static magnetic field create a Lorentz force pointing in the  $\pm y$  direction. This results in a wiggling motion in the yz-plane with the wavelength  $\lambda_u$  and a transverse velocity  $\vec{v}_y$ . So far, there is no net energy transfer because, in the transverse direction, the electrons are accelerated as much as decelerated. But, the wiggling electrons emit self-induced synchrotron radiation with a wavelength  $\lambda_r$ , most of which propagates along z with a magnetic field component  $\vec{B}_x$  oriented in  $\pm x$ , as shown in the inset of Fig.1.9. This radiation is not coherent as it interferes constructively as well as destructively. The  $\vec{B}_x$  is perpendicular to the  $\vec{v}_y$ , so they create the longitudinal Lorentz forces  $\vec{F}_z = q_e \vec{v}_y \times \vec{B}_x$  in Fig.1.9 [15]. The energetic beam is fast enough to accompany the wave, letting the longitudinal forces form micro bunches and decelerate them progressively. The decelerated bunches radiate coherently with the wavelength  $\lambda_r$ , forming the laser. The laser power is transmitted to the output, while partially reflected back into the optical cavities to reinforce microbunching. One detail to note is that, in Fig.1.9, after the bunches travel half an undulator wavelength,  $\vec{v}_y$  changes to the opposite direction, but the longitudinal forces do not (otherwise, the bunches would be destroyed). The reason is that the light is slightly faster than the beam, traveling exactly  $\lambda_u/2 + \lambda_r/2$ , while bunches travel only  $\lambda_u/2$  [15]. Therefore, when  $\nu_y$  changes direction, the bunches see the opposite phase of the wave, and thus, the forces are the same relative to the bunches.

 $\lambda_r \ll \lambda_u$  because the relativistic electrons see much shorter lengths between dipole magnets due to the length contraction. The relation between the output frequency and undulator wavelength is,

$$\lambda_{\rm r} \propto \frac{\lambda_{\rm u}}{2\,\gamma^2}$$
 (1.5)

where  $\gamma$  is the Lorentz factor of the beam. From Eq.1.5, the output frequency can be increased by simply increasing the energy of the electron beam. This gives significant tunability to FEL. An FEL can provide a wider spectrum than any other conventional laser. Its spectrum ranges from

microwave, terahertz, infrared to visible, ultraviolet (UV) to X-ray. The frequency can also be tuned with undulator period  $\lambda_u$  and static magnetic field strength [15].

On the other hand, the required beam qualities for an FEL are much tighter than those of klystron and TWT. One main requirement comes from the diffraction limit of the emitted radiation, which requires that [16, 17]

$$\frac{\epsilon_{\rm N}}{\beta \gamma} < \frac{\lambda_{\rm r}}{4\pi} \tag{1.6}$$

where  $\epsilon_N$  is the normalized emittance, and  $\beta$  is v/c. From the equation, to increase frequency, either the energy must be increased or the emittance must be lowered. Increasing the energy means building costly and sizeable (kilometer scale) accelerators [3]. So, to make FELs more practical and ubiquitous in medical and military applications and in basic sciences, the only choice is to find ways to lower the emittance. Last but not least, since the radiation intensity is proportional to  $N^2$ , where N is the bunch charge, extremely high charge beams are sought. This sets the stage for finding extremely high charge and extremely low emittance, i.e. exceptionally high brightness, beams.

# 1.3.5 Other Applications

The use of free electron beams is not limited to electromagnetic wave amplifiers and generators; the beam itself can also be utilized in applications such as electron-beam lithography (EBL), scanning and transmission electron microscopy (SEM, TEM), and their state-of-the-art time-resolved versions, and in linear accelerators and colliders.

SEM is based on secondary electron emission. When the energetic (typically 10-30 keV) primary electron hits the surface of a material under study, it induces the emission of secondary particles from the surface, which can be detected. By scanning a small beam spot over a sample and measuring the resulting secondary emission intensity, the surface image can be obtained at a very high lateral resolution. Beam spot size and energy spread are important factors in determining spatial resolution. A beam with a lower emittance produces a smaller spot size when it is focused, thereby improving the resolution. Additionally, because a low emittance beam diverges less after a focal point, the working distance between the objective lens and the sample can be increased to

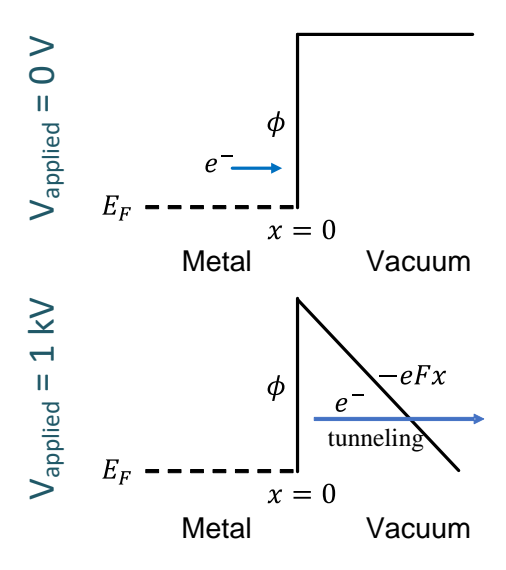


Figure 1.10 Electrons inside the material are bound in the potential well and cannot be emitted into a vacuum. In field emission, a high potential is applied to the cathode so that the electrons can tunnel through the modified potential barrier. By ignoring the image-charge effect, the applied potential result in a triangular barrier with a profile given by  $q_eFx$  where  $q_e$  is the negative electron charge, F is the electric field normal to the surface, and x is the normal distance from the surface. A stronger field results in a thinner barrier, which leads to more emission. By solving the Schrodinger equation with the given profile, the current density of the emission can be calculated.

enlarge the field of view while keeping the resolution nearly intact.

EBL is used to pattern very small features on an electron-sensitive resist. Unlike conventional photolithography, it utilizes an electron beam instead of light. It scans a focused beam of electrons over the surface, on which the regions of the resist that interact with the beam change solubility. By decreasing the energy spread of the beam and increasing its brightness, the resolution can be improved, allowing smaller features to be fabricated.

#### 1.4 Field Emission and Carbon Nanotube Fibers

### 1.4.1 Field Emission

A free electron beam can be generated from virtually any material but at different costs. An electron must overcome a potential barrier at the material-vacuum interface to be transmitted to free space (Fig.1.10). Conventionally, a minimal energy penalty to leave the material bulk is given by the work function,  $\phi$ . The electron can be emitted using three fundamental mechanisms: thermionic emission, photoemission (photoelectric effect), and field emission. In thermionic emission, the

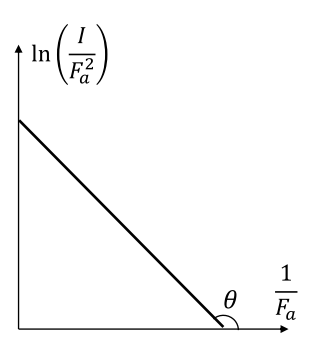


Figure 1.11 By plotting experimental data that includes the applied field  $F_a$  and the measured emission current I in Fowler-Nordheim coordinates as shown in the plot, the filed enhancement factor  $\beta$  can be found from the slope  $\theta$ .

excess energy is given by heating the cathode. In photoemission, the excess energy is given by radiating energetic photons on the material surface.

In field emission, instead of energizing the bulk electrons, the profile of the potential barrier is modified by applying a strong electric field as shown in Fig.1.10. The formed triangular barrier enhances the probability of tunneling exponentially. From Fig.1.10, a stronger field results in a thinner barrier, increasing the tunneling probability, and hence, emission current. By solving the Schrodinger equation for the potential profile, the resulting current is given by the Fowler-Nordheim equation

$$j = A \frac{1}{\phi} F_l^2 e^{-\frac{B\phi^{3/2}}{F_l}}$$
 (1.7)

$$I = S_{\text{eff}} j \tag{1.8}$$

where j is the current density, I is current,  $F_l$  is the local field normal to the surface,  $\phi$  is the work function,  $S_{\text{eff}}$  is the effective emission area, and A and B are constants. For a typical range of  $F_l$  (10<sup>7</sup> V/cm–10<sup>8</sup> V/cm), the current grows exponentially with the field.

In a field emission experiment, absolute determination of  $F_l$  and  $S_{\text{eff}}$  are very difficult. The absolutely measurable values are I and applied field  $F_a$ .  $F_a$  is determined by the geometry of the apparatus, often using the simple relation  $F_a = V_a/d$ , where  $V_a$  is the applied voltage and d is the interelectrode gap.  $F_l$  and  $F_a$  can differ significantly due to micro surface irregularities (protrusions and asperities) that can enhance the applied field 10's or even 100's of times. The relation between

 $F_a$  and  $F_l$  is given by

$$F_l = \beta F_a \tag{1.9}$$

where  $\beta$  is the field enhancement factor. Experimental data can be used to find  $\beta$  by plotting it in Fowler-Nordheim coordinates, as shown in Fig.1.11, where the slope  $\tan \theta$  is given by

$$an \theta = -\frac{B \phi^{3/2}}{\beta} \tag{1.10}$$

Due to surface irregularities, the actual value of  $\beta$  can vary locally over the surface. As a result, the values of  $F_l$  and j can vary as well. Eq.1.9 models only a cumulative averaged effect. To increase  $\beta$  and decrease the operation voltage, most emitters are designed as very sharp tips.  $S_{\text{eff}}$  cannot be taken as the whole cathode surface area in most cases due to the local variation of the current density, making it a parameter of uncertainty. Therefore, a better practice is to estimate  $S_{\text{eff}}$  by projecting the beam onto a scintillator screen and measuring the area of the emitting locations.

# 1.4.2 Properties of An Ideal Emitter

In Sec.1.3 many examples are given to emphasize the importance of an electron beam with low emittance, high brightness, and low energy spread. As mentioned in Sec.1.2, normalized emittance and brightness are conserved quantities, and the energy spread is a function of the intrinsic particle distribution inside the material itself (so they cannot be improved or corrected by external beam optics.) Therefore, the beam must be engineered to be of high quality upon emission from the cathode. All in all, the emitter design and the material it is made of are quite literally the tip of the spear.

To achieve low emittance, the cathode must emit an initial beam with a small diameter and divergence angle. To achieve a small beam diameter, the cathode itself must have a small surface area (while emitting uniformly across it.) To achieve a small divergence angle, the mean transverse energy of electrons inside the material must be small, and the geometry of the cathode and surface irregularities must not create strong radial fields where electrons are emitted. For a bright beam, the cathode must also provide a high current and charge. However, obtaining high current from a small

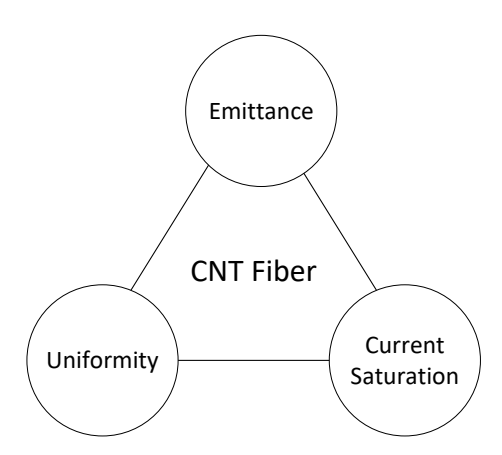


Figure 1.12 In this thesis, three main criteria were studied and used self-consistently to propose and engineer the most advanced CNT fiber cathodes to maximize their brightness.

surface is challenging due to intrinsic carrier density, space-charge effect, and current-induced heating, which limit the maximum current density that can be drawn.

As mentioned in Sec.1.3.2, Sec.1.3.3 and Sec.1.3.4, beam-driven radiation sources require better beam qualities for higher frequency operation. In an FEL (Sec.1.3.4), emittance imposes a theoretical limit on the maximum frequency. Microwave tubes, as discussed in Sec.1.3.2 and Sec.1.3.3, must be physically smaller for higher frequency operation. Consequently, the cathode must have an even lower emittance and smaller area while still producing a high current in the ampere range in order to allow the intense beam to pass through smaller apertures and tubes with minimal loss. In addition, the cathode assembly must also be smaller to fit inside the smaller tubes.

Because field emitters do not require additional laser or heater systems, they allow for most miniaturized and simplified designs. On the other hand, obtaining the required beam charge and emittance, emission stability, lifetime, and reliability still remain challenging for field emitter R&D.

## 1.4.3 Carbon Nanotube (CNT) Fibers as Field Electron Emitters

Traditionally, field emitters are made of high melting point refractory metals such as tungsten (W) and molybdenum (Mo), and ceramics such as LaB<sub>6</sub>, or carbon nanotubes produced in different forms. CNT fiber, in particular, is a collection of long chains of aligned carbon nanotube fibrils. In this work, only fibers produced by wet-spinning technique [18] are used. In this technique, premade CNTs are dissolved in acid to form a liquid dope which is extruded through a spinneret into a

coagulant bath to remove the acid and then dried in an oven, forming the fibers. This technique ensures dense CNT packaging and good alignment. The resulting fibers are very conductive, flexible, and durable.

As a field emitter, CNT fiber has drawn a lot of attention due to its very low turn-on voltage and high current output. It is a natural field enhancer, implying it does not need a sharp tip. It shows anisotropic emission [19], meaning most of the emission is along the fiber, not from side walls, which offers control over emittance. However, these properties, while necessary, are not sufficient.

The ultimate parameter which determines the fiber's applicability for high-power and frequency rf systems is the cathode brightness. In this thesis, to test and maximize the brightness, the fibers were studied and engineered based on three criteria: emittance, emission uniformity, and current saturation as shown in Fig.1.12.

Uniformity can be described as the distribution of emission current load over the surface. As mentioned in Sec.1.4.1 and Sec.1.4.2, surface irregularities may restrict emission to a certain number of active spots. The high emission current load on these spots leads to local overheating, causing micro breakdowns and instabilities, thus, limiting the maximum current that can be drawn and the brightness, as well as long-term operation stability and reliability.

Current saturation is the decrease in the rate of emission current increase as the applied voltage increases. It limits the maximum current cathode can emit at practical voltages and, thus, its brightness. Although all types of cathodes show current saturation, the mechanism behind them can be quite different. CNT fibers also exhibit saturation behavior. In the literature, it is generally attributed to space-charge effect [20, 21]. It is the fundamental saturation mechanism for metals. However, as the CNT fiber is not a metal, a metal-like treatment appears deficient. Understanding this issue of saturation and proposing a solution are essential to maximize the emission current and hence brightness.

Many studies on CNT fibers are primarily based on measuring *I-V* data to analyze their emission current performance. However, in this thesis, not only was the current measured, but also the beam was synchronously spatially monitored *in situ* to measure the other essential parameters in Fig.1.12.

All measurements were enabled by a custom-made field emission microscopy setup [1]. The core of the setup was a scintillator screen onto which the beam was projected. The screen was used as the anode electrode, and to enable biasing, it was coated with a thin layer of a conductive material. The projected beam forms a pattern on the screen, which is recorded by a camera, forming an emission micrograph. The micrographs give information on the amount of beam spread and uniformity, the beam divergence angle, and current density. By analyzing the micrographs and the *I-V* data together, emittance, brightness, emission uniformity, and saturation current density were calculated, analyzed, and understood.

#### **CHAPTER 2**

#### EVALUATING AND INTERPRETING SPATIAL EMISSION OF CNT FIBERS

This chapter is based on the author's published paper: **T. Y. Posos**, S. B. Fairchild, J. Park, and S. V. Baryshev, "Field emission microscopy of carbon nanotube fibers: Evaluating and interpreting spatial emission," *Journal of Vacuum Science & Technology B* **38**.2, 024006 (2020), https://doi.org/10.1116/1.5140602.

In this chapter, we quantify field emission properties of cathodes made from carbon nanotube (CNT) fibers. The cathodes were arranged in different configurations to determine the effect of cathode geometry on the emission properties. Various geometries were investigated including (1) flat cut fiber tip, (2) folded fiber, (3) looped fiber, and (4) fibers wound around a cylinder. The author employs a custom field emission microscope to quantify I-V characteristics in combination with laterally resolved field-dependent electron emission area. Additionally, we look at the very early emission stages, first when a CNT fiber is turned on for the first time, which is then followed by multiple ramp-up/down runs. Upon the first turn on, all fibers demonstrated limited and discrete emission area. During ramping runs, all CNT fibers underwent multiple (minor and/or major) breakdowns, which improved emission properties in that turn-on field decreased and field enhancement factor and emission area both increased. It is proposed that breakdowns are responsible for removing initially undesirable emission sites caused by stray fibers higher than average. This initial breakdown process gives way to a larger emission area that is created when the CNT fiber subcomponents unfold and align with the electric field. Our results form the basis for careful evaluation of CNT fiber cathodes for dc or low frequency pulsed power systems in which large uniform area emission is required or for narrow beam high frequency applications in which high brightness is a must.

## 2.1 Introduction

Novel cathodes are being investigated for use as electron beam sources for next generation vacuum electronic devices (VEDs). Applications such as electron microscopy, x-ray sources, and traveling wave tube amplifiers require high current, high brightness electron beams with a narrow

energy distribution. Cathodes need to be robust and durable to protect against damage from ion back-bombardment and heating (external or self-induced) during operation. Cathode lifetimes of a few thousands of hours are required [22].

As VEDs progress toward higher frequency and higher power operation, the benefits of using field emission cathodes rather than thermionic cathodes becomes apparent. This primarily stems from the fact that cathode size scales as 1/f, where f is the fundamental operating frequency of the device. Higher frequency devices [23–25], therefore, require smaller cathodes, and the excessive heat generated by thermionic emission can result in severe thermal stress placed on cathode assemblies, which leads to beam instability. Field emission cathodes also offer the potential of fast ON/OFF switching, as compared to externally heated thermionic sources that require a temperature thermal ramp-up to reach maximum emission current. This fast ON/OFF switching capability offers potential for more efficient gating techniques.

Fibers made from carbon nanotubes (CNTs) have demonstrated significant potential for use as field emission cathodes [22, 26]. CNT fibers have excellent electrical and thermal conductivity and produce high output emission currents with good current stability for ultralow turn-on voltage. To date, most data on the emission properties of CNT fibers have been obtained by measuring emission current in a simple diode configuration with the voltage applied to a metallic anode positioned above a vertically mounted fiber. However, there are numerous examples demonstrating that field emission is often not laterally uniform [27, 28]. Thus, there is a need to evaluate emission area to realistically estimate current density and cathode brightness.

To spatially resolve the emission properties of CNT fibers, we utilize a projection type field emission microscopy apparatus that can both measure and image the emission current. Four different CNT fiber cathode designs were fabricated for this measurement. We observe that CNT fibers undergo a conditioning process that immensely improves formal emission characteristics (turn-on field and field enhancement  $\beta$ -factor) but not necessarily spatial uniformity/coherence of emission. We find that the field emission area is responsible for unconventional emitter behavior, namely, emitter saturation and self-heating. Results and conclusions are consistent across all the

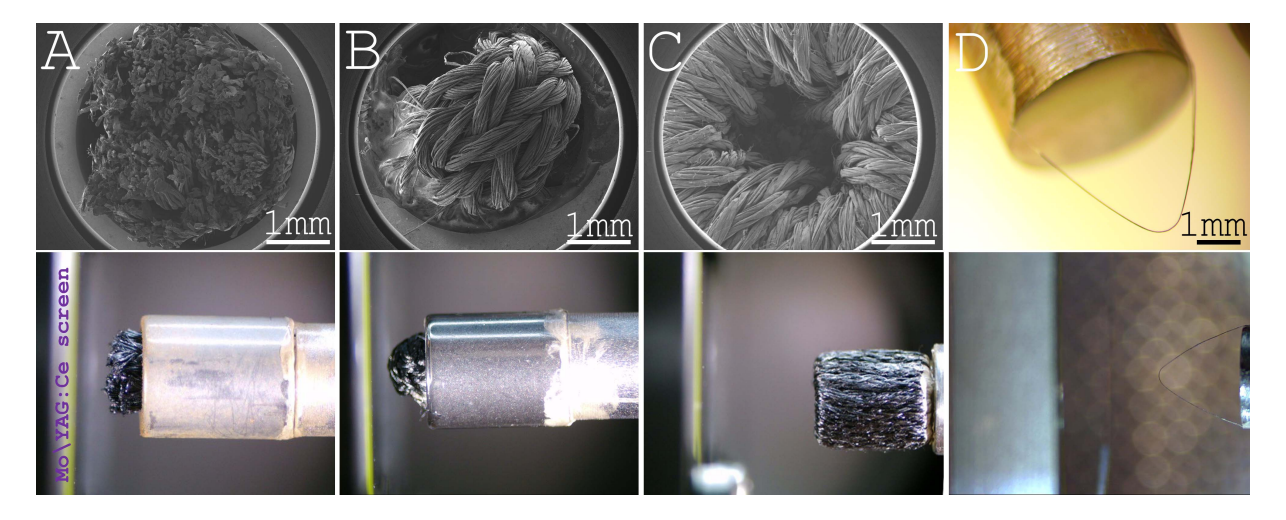


Figure 2.1 SEM images of sample A (flat cut sample), sample B (folded sample), sample C (wound geometry sample), and optical microscope image of sample D (looped sample). Bottom row: side camera views of samples A, B, C and top camera view of sample D when the samples are placed against the imaging YAG:Ce screen. All these images are taken before starting the experiments. There were no visible signs of unfolded stray fibrils on the samples.

tested geometries. The most promising CNT fiber cathode design is emphasized.

# 2.2 Samples and Experimental

The CNT fibers used in these experiments were purchased from DexMat, Inc., Houston, TX. The fibers were fabricated using a wet spinning technique described by Behabtu *et.al.* [18]. This fabrication process ensures that the CNTs comprising the fibers are closely packed and highly aligned which ensures high electrical and thermal conductivity [29], as well as optimal performance when used as either wire conductors or field emission cathodes [18, 30–32]. Carbon nanotube yarns are made by twisting or braiding together multiple CNT fibers. Both individual fibers and twisted yarns were used in these experiments.

The CNT fibers were arranged in four different configurations, which utilized either a single  $\sim 90 \, \mu m$  diameter fiber or multiple fibers braided together into a larger diameter yarn. These different configurations allowed us to investigate the effects of surface geometry on electron brightness, beam size, emission area, and current density.

Sample A consisted of four yarns inserted together into a 3 mm diameter metal tube. Each yarn consisted of  $\sim 850$  fibers braided together to make the total yarn diameter  $\sim 900 \, \mu m$ . The yarns

are protruding from the end of the tube where then mechanically cut in an attempt to get a surface with uniform emitter heights. This was difficult to achieve due to the toughness of the CNT yarns, which makes them difficult to cut. The final results are shown in Fig.2.1A, which shows an SEM image of the cut fibers as well as an optical image that shows a side view of the cathode.

Sample B was made of CNT yarns that were  $\sim 200\,\mu m$  in diameter. They consisted of 180 CNT fibers braided together. Several yarns were folded together and then shoved through the metal tube to make a somewhat rounded tip that protruded through the end of the tube. Fig.2.1B shows an SEM image of the bunched yarns at the top of the tube as well as an optical image which shows a side view of the cathode.

Sample C was made by winding a CNT yarn around the wall of a 3 mm diameter metal tube. The purpose of this sample was to see if we could make a uniform emission edge around the edge of the tube. Fig.2.1C shows an SEM image of the top of the tube showing the yarns pulled over the edge. Also shown is an optical image of the side of the cathode. Samples A, B, and C were all attached to the steel cylinder with silver paint to ensure an electrical contact to ground.

Sample D was a single looped CNT fiber of  $\sim 90~\mu m$  in diameter, which was arched and attached from both ends to the stainless steel base. The fiber was contacted to the steel base with silver paint. Optical images of the cathode are shown in Fig.2.1D.

The experiments were performed using a field electron microscope given in Ref.[1]. The measurement setup is shown in Fig.2.2. In place of a standard metal anode, we used a custom scintillator anode screen. The scintillator is optical quality single crystal cerium-doped yttrium aluminum garnet (YAG:Ce) of 1" in diameter and 100 µm in thickness. To establish an electric field between the sample and the isolating YAG:Ce anode and to collect the current, a metal film needs to be deposited. Molybdenum (Mo) was chosen because it is dense and allows for continuous ultra-thin films. The 7–8 nm Mo coatings were applied in house by dc magnetron sputtering. The coating is thin enough to allow 10% of all the electrons from the cathode penetrate and strike the YAG:Ce to produce green light, while it is thick enough (by absorbing 90% of electrons) to prevent YAG:Ce screen from charging up [1]. Another advantage of Mo is in that it has high melting

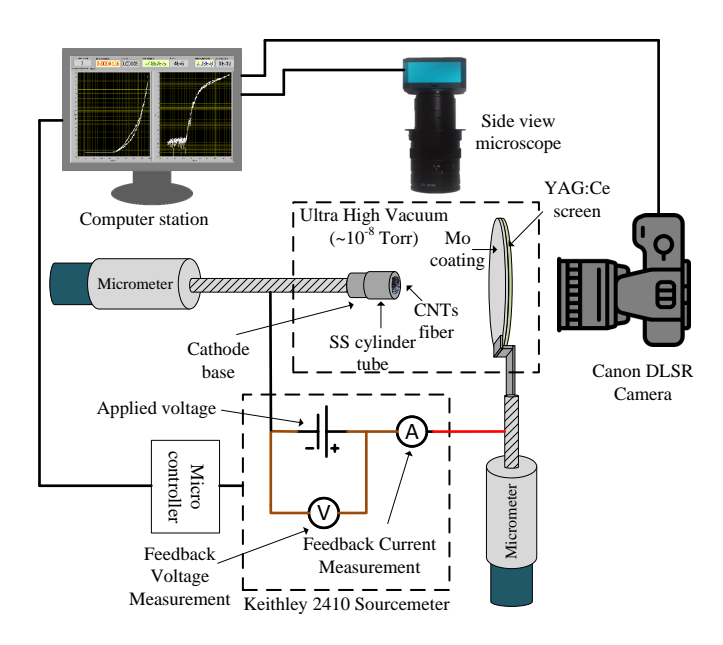


Figure 2.2 Experimental setup cartoon

point (2896 K), so it can sustain exceptionally high electrical power surface densities. No visible electron bombardment induced damage (burn-through pinholes) was observed on the screen upon completing measurements. Cathode mounts were made out of 316 stainless steel in a form of a cylinder of 4.4 mm in diameter. The cathode assembly was then attached to a in-vacuum micrometer to adjust the interelectrode gap. Parallelism of the screen and the sample surface is checked by top- and side-view cameras when installing the cathode (see Fig.2.1, bottom row). Samples and the vacuum chamber are grounded. The screens are positioned using another translation arm that is attached to the system using a custom quartz nipple and, therefore, electrically isolated from the chamber. It is positively biased in the experiment. Emitted electrons from the sample under the effect of the bias voltage are accelerated toward the screen and strike the screen with an energy equal to the applied voltage. In such a way, electrons arriving from different points of the emitting cathode surface create cathodoluminescence patterns (at 550 nm luminescence line) on the YAG:Ce screen. The patterns, captured by a Canon DLSR camera with CMOS full frame sensor installed at viewpoint behind the screen, represent laterally resolved field electron emission. Applied voltage, feedback current and feedback voltage readings are enabled by Keithley 2410 electrometer. The electrometer was programmed to sweep voltage up/down with 1 V step with 100 µA set as an upper limit for the emission current. Dwell time for each voltage step is 5 s to sample and record current, set and feedback voltage and vacuum pressure, and calculate statistical error bars. The system was programmed to take field emission images every  $10\,\mathrm{V}$  such that taking images was synchronized with the electrometer. All measurements were done in vacuum  $2-5\times10^{-8}\,\mathrm{Torr}$ .

## 2.3 Results and Discussion

# 2.3.1 Conditioning Microbreakdowns

All samples were tested multiple times; each test included the voltage sweep up and then down. Fig.2.3 summarizes electric *I-E* characteristics comparing the first and the last run; *E*-field is the actual field that is calculated using the measured feedback voltage  $V_f$  and the measured gap. One particular feature can be seen—it is the improved efficiency of the cathodes in that the turn-on field decreased and field enhancement  $\beta$ -factor increased. The main vehicle mechanism of the improvement is the "conditioning" process that happens through a series of igniting/quenching emitters that, in most extreme cases, is accompanied by breakdowns of different strength. The ignition/quench process appears as extensive noise of the I-E curves of the initial run for all samples, labeled as Ab, Bb, Cb, Db, where "b" stands for "before". Aa, Ba, Ca, Da, where "a" stands for "after" show I-E curves upon completing 4 runs. The extensive conditioning noise is visible because every point on the *I-E* curve is collected for 5 s to gain enough statistics in order to calculate average current, voltage, pressure, and their error bars [1]: such a long dwell time captures ups and downs in the output current of the fibers turned on for the first time. The error bars, shown with light red and blue in Fig.2.3, are derived from the standard deviation of the mean as the microscope does multiple samplings (5 s) for every (current-voltage-vacuum pressure) point. The current noise of a relatively large amplitude (3–5 times) could be associated with breakdowns (if any) that have negligible strength, i.e., cannot be detected in our system. Following our previous work [33], the sizable microbreakdown/discharge taking place can be visualized by plotting the difference between the set voltage  $V_s$  and the feedback voltage  $V_f$  versus the feedback voltage or the actual E-field. Such a plot traces the voltage loss in the system due to arcing: since the electrometer is power limited, the arc will cause  $V_f$  to drop with respect to  $V_s$ . Note, since the

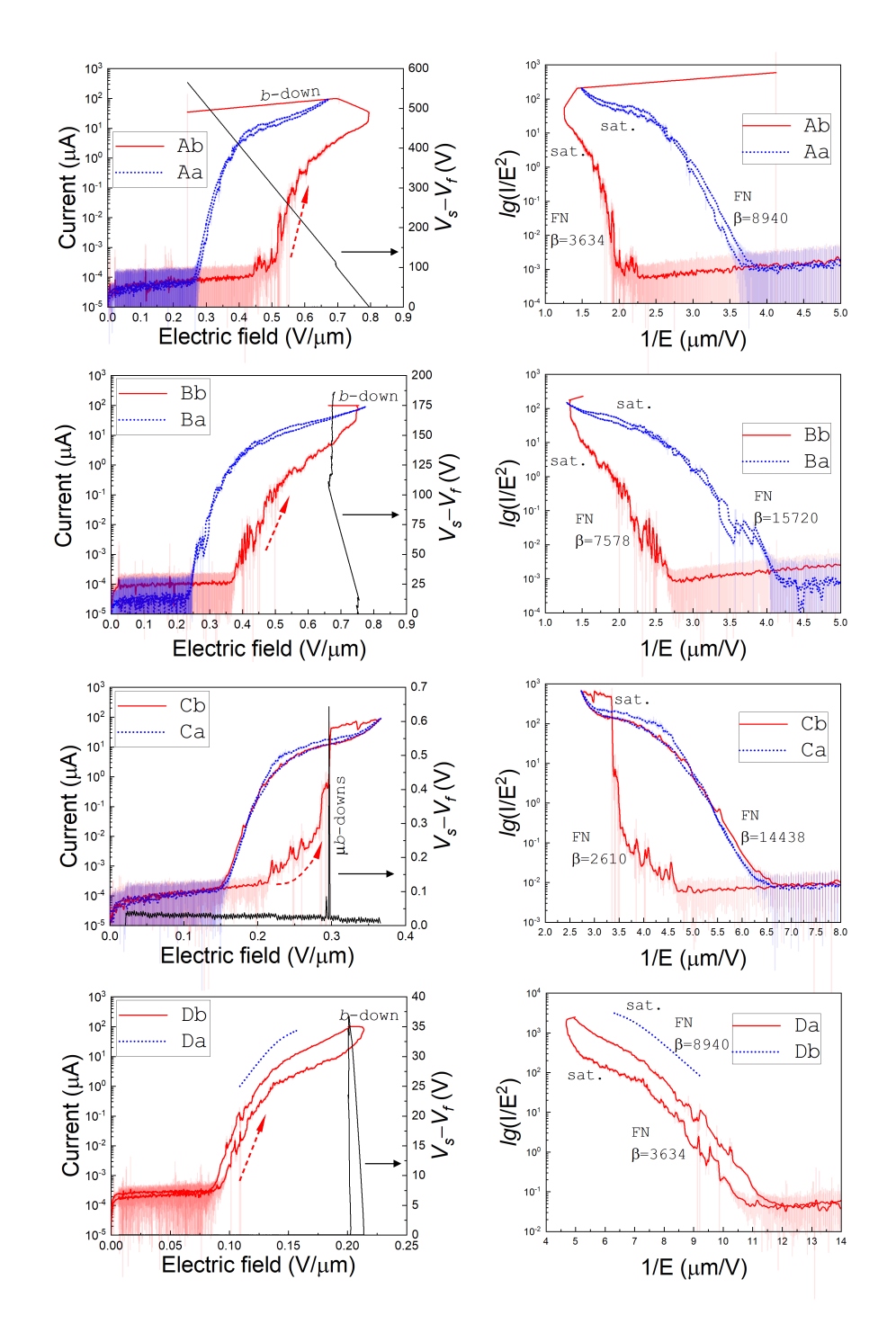


Figure 2.3 Semilog I-E curves and FN plots for the studied fibers. The solid black curves show the difference between the set voltage of the electrometer ( $V_s$ ) and the actually measured feedback voltage ( $V_f$ ) applied to the sample. Horizontal black arrow indicates axis for the  $V_s$  –  $V_f$  curve. Capital letter A is the flat cut sample, B is the folded sample, C is the wound geometry sample, and D is the looped sample. Small letter "b" corresponds to emission "before" initial conditioning, "a" corresponds to emission "after" the very last test run. Error bar regions for the dotted blue and solid red curves are shown in light blue and light red, respectively.

dwell or integration time per point is 5 s, shorter surges will result in smaller delta between  $V_f$  and  $V_s$  even if the breakdown/arc/discharge strength was of the same magnitude. In that sense, we are looking for nonzero difference between  $V_f$  and  $V_s$  to mark off the breakdown rather than evaluate its actual strength. In Fig.2.3, the *I-E* curves are superimposed with  $V_s - V_f$  traces. As can be seen, all four samples underwent through breakdowns of different strengths or lengths (or both). Upon the first turn-on, samples A and B do not have ramp down curves as the strength/lasting of the breakdowns was extensive and the power supply was automatically shut down via a safety interlock. Even though the breakdown is often seen a damaging process, in the present case, there were significant emission property improvements. For example, sample A before (Ab) and after (Aa) experienced twofold decrease of the turn-on field, from about 0.5 to 0.25 V/ $\mu$ m, and threefold increase of the  $\beta$ -factor, from about 3000 to 9000.

## 2.3.2 Field Emission Microscopy and Conditioning

To better understand the effects of conditioning and fully characterize the fiber design, the presented *I-E* curves are compared to the laterally resolved field emission micrographs that are compiled in Fig.2.4. They compare the emission patters between the first and the last tests. A few main features can be noted as follows:

- (1) Samples A and B improved their emission by means of increasing the total number of strong emitters seen as bright spots on the micrographs Ab/Aa and Bb/Ba. The larger the number of strong emitters (higher  $\beta$ -factor) the lower the turn-on field: the electrometer senses currents above the detection threshold and, therefore, larger number of high  $\beta$ -factor emitters will deliver an output current of a magnitude above the threshold at a lower E-field.
- (2) Sample C behaved differently. As seen from Fig.2.3, the run Cb demonstrated very slow response to the field in that the output current remained  $\sim 0.1$ –1 nA even though the applied field significantly changed (corresponding to the applied voltage of 100 V, out of entire sweep ranging 0–375 V). Then, a series of microbreakdowns took place (at least two were detected) and the output current instantaneously inflated by over 3 orders of magnitude. Concurrently with the breakdown at  $0.3 \text{ V/}\mu\text{m}$ , one strong emitter (see Cb in Fig.2.4) appeared as a red spot. Our imaging screens

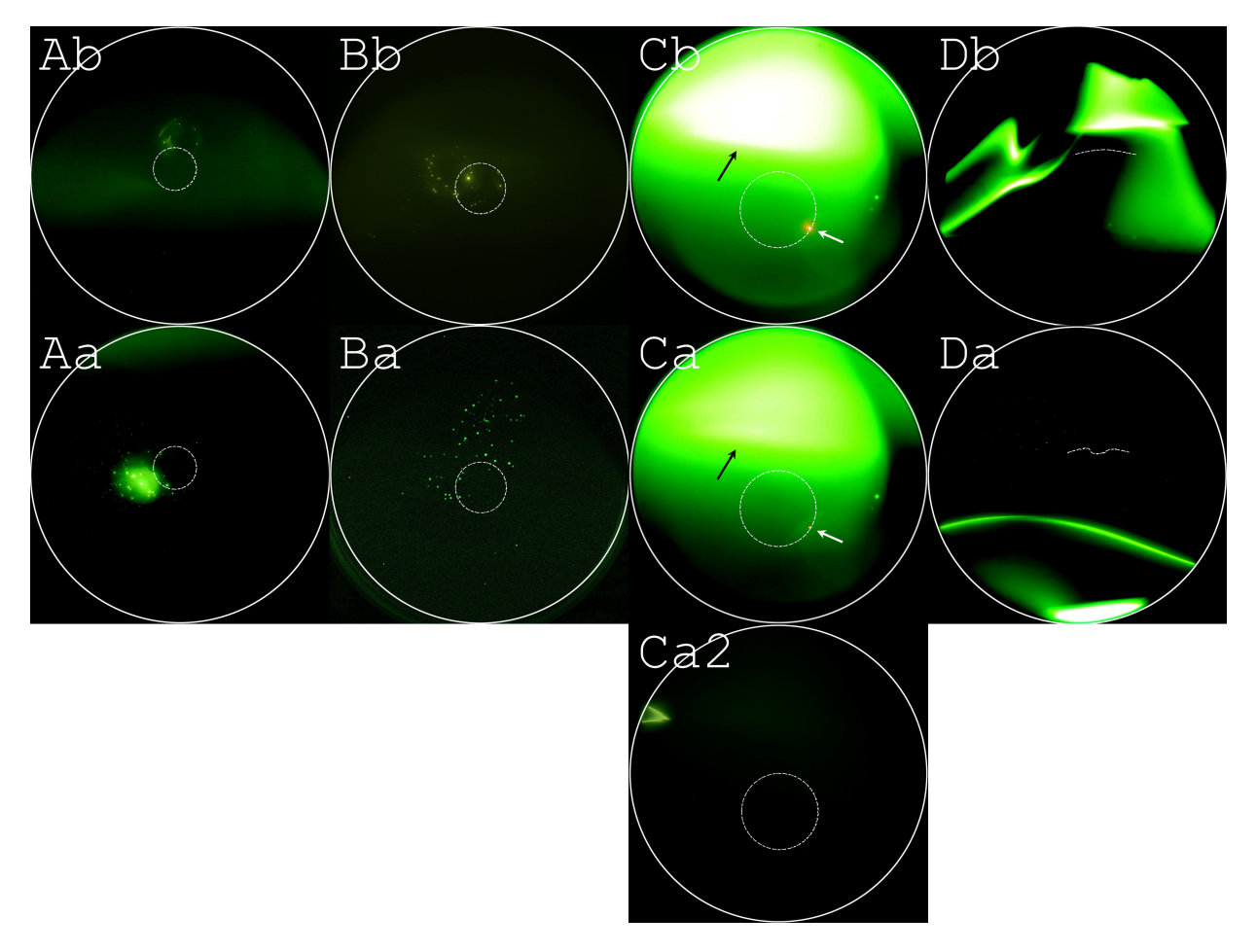


Figure 2.4 Laterally resolved field emission pattern on YAG screen taken at the same electric field before and after conditioning for sample A  $(0.67\,V/\mu m)$ , B  $(0.72\,V/\mu m)$ , C  $(0.36\,V/\mu m)$ , and D  $(0.16\,V/\mu m)$ . The white dashed circles and line show actual position and orientation of the samples with respect to the YAG screen. The white arrows show the location of the red spot. The black arrows point at the halo. The outstanding image at the bottom (Ca2) illustrates the source of the halo background: it is a stray emitter pair projected to be nearly parallel to the screen plane thus generating electron rays that have long path across the screen resulting in intense halo.

are semitransparent to the red, and in this case red light emission from the emitting locations was bright to the extent that the green light emission from the YAG anode screen was not seen. The intense red light emission suggested that this specific emitter was delivering major portion of the detected output current  $100 \,\mu\text{A}$ . The small emitter size (single nanotube or a cluster of single CNTs) resulted in extensive current density and, therefore, led to exceptional thermal heating of this emitter. Unlike samples A and B, sample C retained a very similar emission area (i.e., one red emitter in the right bottom corner) in the following runs. One can see that the ramp down *I-E* curve of the initial run (Cb) and *I-E* curves of the subsequent run (Ca) are identical.

There was no quantification metric for emission area of sample D and its emission imaging results will be discussed in more detail in Subsection 2.3.5 that follows. Since the sample was free standing, i.e., lacking strong mechanical support, after the first breakdown happened, we tested sample D by setting the voltage manually instead of using our automatic setup in order to observe emission pattern and its stability at a constant applied field and to have more control over measurement. The voltage was increased in 25 V steps. At each step, the voltage was kept constant for a few minutes, YAG:Ce screen image was taken, and current data were recorded (both manually). We recorded data when the fiber started to emit 1 μA current until it reaches 100 μA. That is why after conditioning run of sample D (Db) has limited range in Fig.2.3.

Overall, the emission improved after fibers underwent conditioning breakdowns: this is seen as improved efficiency (lower turn-on field and enhanced  $\beta$ -factor), which happened alongside with the improved spatial emissivity of the fibers in that the emission area was increased. A rough stepwise process can be described as (1) the breakdown increases the number of emitters (i.e., through mechanical unfolding) and (2) the larger number of emitters deliver larger output current seen as lowered turn-on field and larger  $\beta$ -factor of the Fowler-Nordheim (FN) like part of the *I-E* curves. This model is further supported by the analysis of the saturation sections of the *I-E* curves; saturation follows the FN-like part when going to higher current range. The FN-like and saturation regions are labeled with "FN" and "sat.", respectively, on the FN plots given in Fig.2.3.

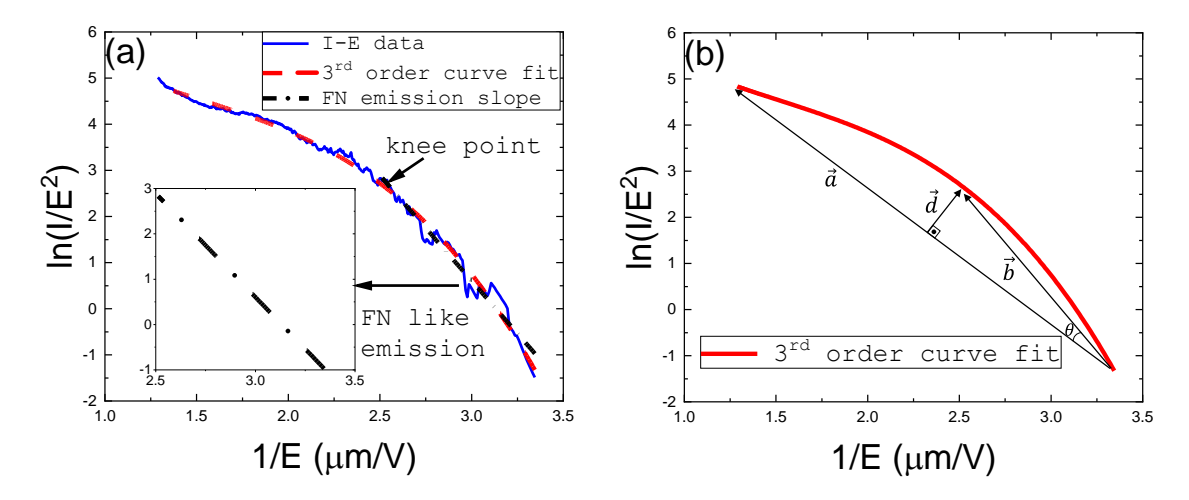


Figure 2.5 (a) Emission curve after noise reduction processing (solid blue), third order polynomial fitting (dashed red), deduced FN-like section of the I-E curve used for calculation of the  $\beta$ -factor (dot-dashed black), zoom in view of the deduced FN-like section is shown in the inset plot. (b) The vector family used in the knee point calculation.

## 2.3.3 Emission area: FN versus Image Processing

According to the FN law, the emission current as a function of applied electric field is given by

$$I = 1.54 \times 10^{-6} \left( \frac{\delta S}{\phi} \right) (\beta \cdot E)^2 \cdot \exp\left( \frac{-6.83 \times 10^9 \cdot \phi^{3/2}}{\beta \cdot E} \right)$$
 (2.1)

where  $\delta S$  is effective emission area,  $\beta$  is unitless effective or apparent field enhancement factor, and  $\phi$  is the work function which is assumed as 4.8 eV for all the CNT fiber geometries. When  $\ln(I/E^2)$  is plotted against 1/E, the slope gives  $[-6.83 \times 10^9 \cdot \phi^{3/2}/\beta]$ .

Although for metallic surfaces, the experimental data show linear slope [34], for the nonmetallic and semimetallic surfaces, there is deviation of the slope from linear trend [35]. For all geometries of the fiber samples tested, after filtering out conditioning noise portion of the FN plots, there were two distinct slope regions: one for low applied field and the other for high applied field (see FN plots in Fig.2.3). The curves have "knee" point separating one slope region from another. The low applied field linear region of a larger slope corresponds to FN-like emission. The high applied field linear region of a smaller slope corresponds to saturation region.

The apparent  $\beta$ -factors were calculated from the slope of FN-like portion of the *I-E* curve using the following procedure: (1) noise data filtration, shown by blue solid line in Fig.2.5(a); (2) third order polynomial fit, shown by dashed red line in Fig.2.5(a); (3) knee point calculation [36],

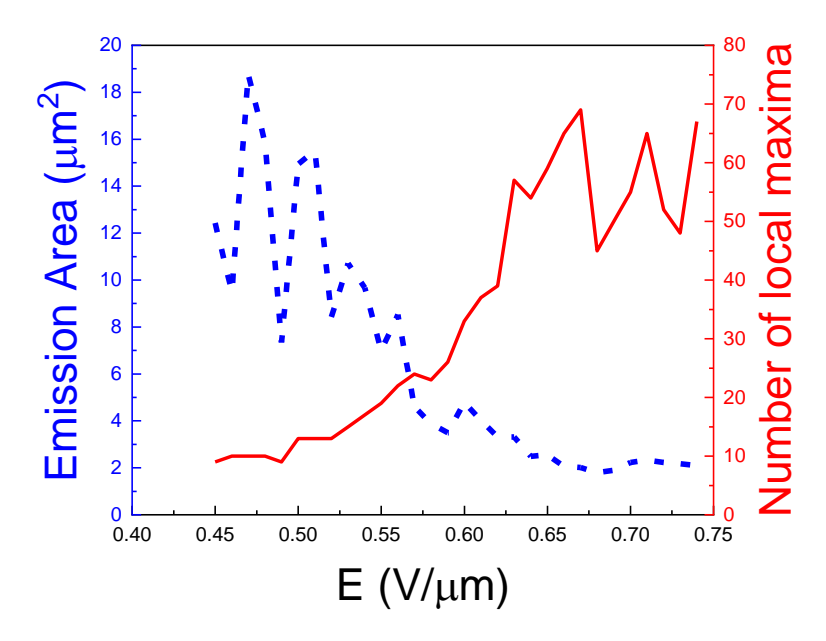


Figure 2.6 Comparison of the emission area on the applied electric field for the folded sample B before conditioning, as extracted from *I-E* curves using the FN equation versus from the field emission micrograph dataset using an image processing algorithm (Ref.[35]) developed elsewhere.

using a set of vectors as shown in Fig.2.5(b); (4) filtering out all the points above the knee point; and (5) fitting fist order polynomial of the remaining low field curve and calculating its constant slope to extract effective field enhancement factor. The final slope is shown by black dashed line in Fig.2.5(a). More specifically, step (3), when the knee point is calculated, is done by finding a unique point on the third order polynomial fit to find the maximum magnitude of vector  $\vec{d}$  [shown in Fig.2.5(b)] defined as

$$\vec{d} = \vec{b} - b \cdot \cos\theta \cdot \hat{a} = \vec{b} - (\vec{b} \cdot \hat{a}) \cdot \hat{a} \tag{2.2}$$

where  $\vec{a}=a\cdot\hat{a}$  is a constant vector between two edges of the curve,  $\vec{b}=b\cdot\hat{b}$  is a variable vector from one edge of the curve to each data point,  $\hat{a}$  is unit vector in the direction of  $\vec{a}$ , and  $\theta$  is angle between  $\vec{a}$  and  $\vec{b}$ . Final  $\beta$ -factor values extracted for all samples are labeled in Fig.2.3.

Effective emission area is then calculated using the measured I-E data and calculated  $\beta$ 's through Eq.2.1. The calculated dependence  $\delta S(E)$  for sample B is shown in Fig.2.6 as the decaying dashed blue line. However, the results obtained using a custom image processing algorithm developed by our group before [35] show opposite trend:  $\delta S$  is predicted to increase as the applied field increases (red solid line in Fig.2.6). Field emission micrographs taken concurrently with I-E curves and

processed in batches point out that local emitting maxima multiply with the field. To keep the discussion to the general level and compare the trends, we do not present detailed analysis of the emission area and only calculate local maxima (brightest emitter locations). Assuming that the source behind every local maximum is a single CNT,  $\delta S$  must grow with the field. The same issue was first pointed out in an original Air Force Research Laboratory (AFRL) study of a CNT fiber [22]. Using a Particle in Cell (PIC) simulation, it was shown that the emission area has to be a growing function of the *E*-field to account for the observed emission characteristics. The presented results are an experimental evidence that support the earlier PIC findings. This result is also supported by our earlier studies of nanodiamond emitters in which  $\delta S$  grows nonlinearly with the electric field [35]. Together, this result adds to concerns raised in the recent literature [37, 38] about the validity of FN equation application for extracting the emission area. This problem is under intense investigations in our lab.

#### 2.3.4 Current Saturation

One of the quantitative ways [39] to describe saturation current plateau of a nonmetallic field emitter, or the total current limit that cannot be exceeded, is

$$I_s^{\text{max}} = \frac{|\mathbf{q}_e| \cdot n^{2/3} \cdot \nu_\infty}{l} \cdot \delta S \tag{2.3}$$

where  $q_e$  is the electron charge, n is the bulk charge carrier concentration,  $v_\infty$  is the saturated drift velocity, l is the depletion length, and  $\delta S$  is the emission area. Since each sample fibers' constituent CNT material is the same in the before and after experiments, it can be speculated that their properties are the same. The only parameter that is changing then in formula (2.3) is the emission area. From comparing the l-E curves and field emission micrographs (given for before and after runs at the same electric field) for samples A and B, it is seen that the output current saturation plateau value increased by five to seven times and so did the emission area as suggested by image processing illustrated in Sec.2.3.3. Unlike A and B, sample C showed no change of the output current in the saturation regime (ramp down of the Cb and Ca in Fig.2.3). From comparing to Fig.2.4 Cb and Ca, it can be noted that the single emitter generated during breakdown remained

and, therefore, no change in the output current was observed; this is consistent with formula (2.3).

Using typical numbers for CNTs,  $n \sim 10^{18}\,\mathrm{cm}^{-3}$  (calculated from  $\sigma = \mathrm{q_e} \cdot n \cdot \mu$ , where  $\sigma = 1\,\mathrm{kS/cm}$  [40] and  $\mu = 10^4\,\mathrm{cm}^2/\mathrm{V}\,\mathrm{s}$  [41]),  $\upsilon_s \sim 10^7,\mathrm{cm/s}$  [42],  $l \sim 890\,\mathrm{nm}$  (calculated using Ref.[43]), it yields the diameter of the emitter of 0.7  $\mu$ m. This result is much smaller than the lateral resolution of our microscope, typically 5–10  $\mu$ m. Contrastingly, for all samples single emitters appear as  $\sim 0.1\,\mathrm{mm}$  spots on the YAG screen. The reason for that is a fairly large magnification of the system when the fibers are placed far away from the screen (1 mm in this case). Magnification of a point like electron source can be estimated as

$$mag = 2 \cdot d \cdot \tan \alpha \tag{2.4}$$

where d is the distance between the emitting surface and the screen (d was 1 mm for samples A, B, and C) and the angle  $\alpha$  is calculated as

$$\alpha = \frac{p_x}{p_z} = \sqrt{\frac{2 \cdot \text{MTE}}{\text{m}_0 \cdot \text{c}^2}} \cdot \frac{1}{\beta \cdot \gamma}$$
 (2.5)

where  $p_x$  and  $p_z$  are transverse and longitudinal momenta, MTE is the mean transverse energy,  $m_0c^2$  is the rest energy (0.511 MeV),  $\beta$  is the ratio between electron velocity and the speed of light, and  $\gamma$  is the Lorentz factor. By using  $\beta = 0.063$  and  $\gamma = 1.1$  at 1 kV and MTE = 4.5 meV (corresponding to its Fermi energy), we find that a point like emitter would appear as a 0.25 mm spot on the screen due to spreading electron rays that have nonzero transverse momentum.

In Ref.[22], the CNT fiber was found to saturate at about 250  $\mu$ A. This result could not be explained by the vacuum space-charge (Child-Langmuir) effect. Extending the application of Eq.(2.3), we find that the emission area in saturation had to be  $\sim 0.02\%$  of the total cross section area of the fiber. PIC results suggested  $\sim 0.3\%$ . The order of magnitude discrepancy could be explained within the series ballast resistor model [39, 44], by adding extra terms (in addition to the basic resistivities associated with the transport through the depletion region and tunneling barrier transparency) in the following form:

$$R_i \propto \sum_i \frac{m^*}{q_e^2 \cdot n} \cdot \frac{1}{\tau_i}$$
 (2.6)

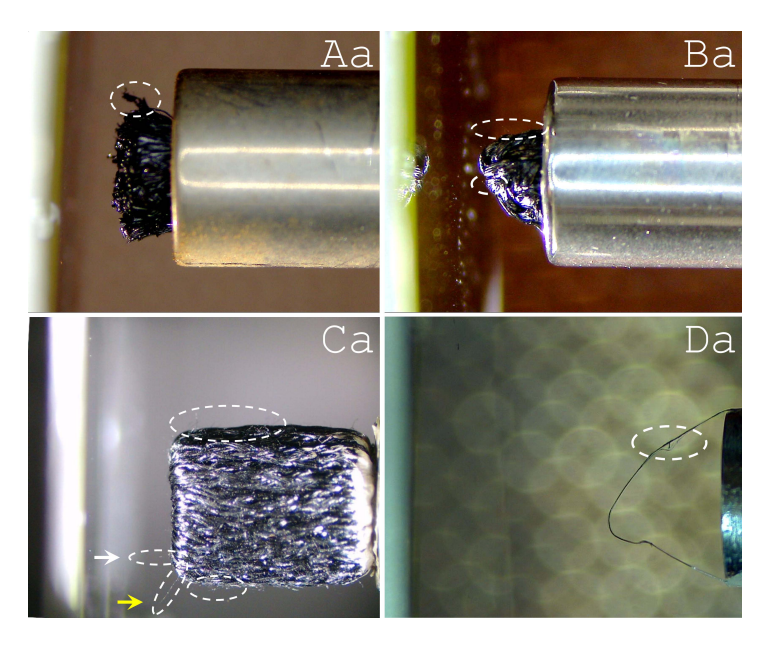


Figure 2.7 Demonstration of various types of unfolded and differently aligned stray CNT fibrils that are formed after conditioning breakdowns—all taken by the top-view camera, except for sample C, which was inspected by the side-view camera to reveal the origin of the red spot.

where  $\tau_i$  is a characteristic scattering time that should be associated with microscopic bundle/alignment structure. An effect of this sort, earlier observed in Ref.[32], can change the onset of saturation by many folds and adds an uncertainty to emission area calculation and was not included before into basic/simplified models.

# 2.3.5 Emission Uniformity and Directionality

Additional analysis of Fig.2.1 shows that four fiber designs demonstrated very different emission patterns that can be further discussed and interpreted as follows:

(1) There is the glowing background that exists on every image set in Fig.2.1. They come from tangent electron rays that penetrate the anode screen at shallow angles. Sometimes, they can be visualized by moving the screen such that the sample is at the edge of the screen or by increasing the distance between the screen and the cathode. Then, the background halo source can be seen at the opposite edge of the screen as a streaked magnified nanotube oriented more in parallel, rather than perpendicular to the screen plane. This is exemplified in the outstanding image in Fig.2.4 (Ca2) for sample C that had the strongest halo. Typically, the halo becomes stronger after the conditioning process, additionally confirming mechanical untangling of CNTs comprising the fibers. These

CNT bunches are seen (highlighted by the dashed circles in Fig.2.7) by the top (samples A, B, and D) or side (sample C) view camera measuring the interelectrode gap. The bottom CNT bunch of sample C, perpendicular to screen and marked with the white arrow in Fig.2.7, can be identified as the major emitter on the laterally resolved images in Fig.2.1—when image is taken by the side camera in dark, this location is glowing bright red corresponding to a blackbody temperature of 1500–2000 K. The bottom long fiber bunch, marked with the yellow arrow in Fig.2.7, with 45° alignment with respect to screen, could also be a possible source of the red spot because free standing fibrils are known to realign along the field lines when the electric field is applied. Looking at Fig.2.1, there is correlation: if the fiber is enclosed into a hollow cylinder like samples A and B, the background is suppressed, suggesting mechanical support somewhat mitigates the untangling.

- (2) The physical dimensions are not directly related to emission properties, i.e., emission area is not necessarily large for a large size sample, such as exampled by sample C. All samples demonstrated a counted number of strong emitters during the "before" runs with emission area being orders of magnitude lower that the physical area available for emission.
- (3) Sample B, even improving the emission area upon conditioning, shows a very large distribution of emission angles. When placed 1 mm away from the screen, the emission envelope is three times larger than the actual cathode size (dashed circle in Fig.2.7 Ba). This suggests proper performance for megahertz applications if the fiber is placed in a solenoid field for focusing. If X-band or beyond applications are sought, the brightness of such a design will deteriorate the performance of a VED.
- (4) Upon conditioning, sample D shows no stray emitters (Fig.2.1) and the emission pattern is an arch showing a coherent emission from a section of the looped fiber. At this point, there is no good procedure of evaluating exact field emission area for this type of geometry without knowing the emitting section. One main complication is the parallel shift with respect to the actual fiber loop position that could be caused by a fairly large emission angle. Compared to Fig.2.1 Db, showing spatially incoherent emission centered near the actual emitter location, the emission pattern Fig.2.1 Da was located away from the emitter. It was later found to be caused by a mechanical bend-down of

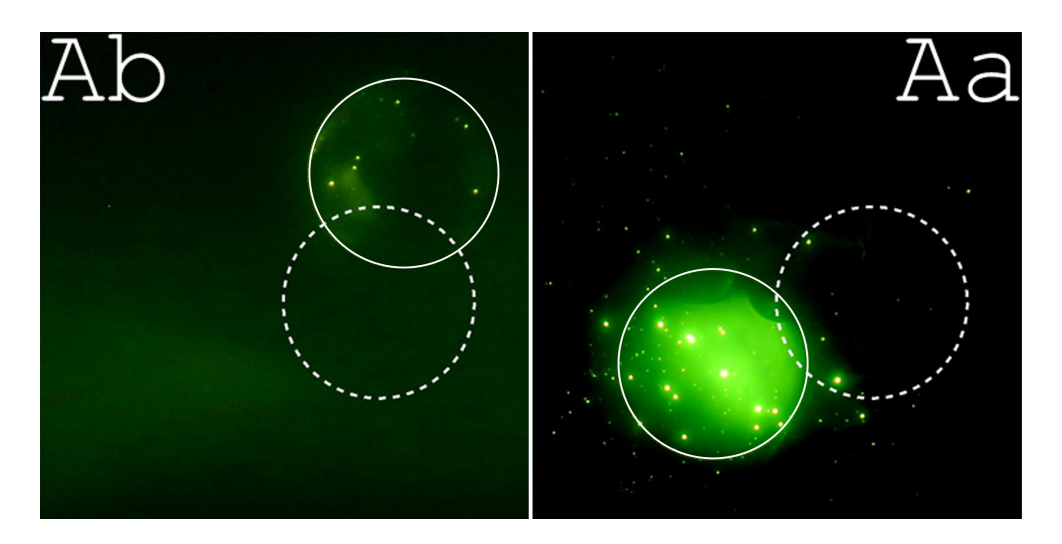


Figure 2.8 Close-ups of emission patterns of sample A before and after the conditioning runs. The dashed line circles depict the actual fiber location with respect to the YAG screen. Solid line circles of the same diameter are to illustrate that major emission pattern fits within the size of the fiber even though there is a parallel shift caused by slight misalignment.

the front half section of the loop that occurred during the initial conditioning run. Even establishing coherent emission, this free-standing design shows weak resilience to conditioning breakdowns that always take place.

(5) The most remarkable and promising performance was demonstrated by sample A. During the conditioning run, the emission is limited to ~ 10 bright strongest pointlike emitters combined with more distributed lobes. Most importantly, all the emission locations are confined within a circle of the size of the emitter A, see Fig.2.8. The parallel shift is due to cut and installation angle imperfections. Electrons start at a small angle but soon after travel along uniform field lines yielding the projection shift with respect to the actual emitter location. In Fig.2.8, the dashed white circle corresponds to the actual fiber position and the solid white circle of the same diameter is to emphasize that the diameter of the emission core matches the fiber diameter. After the breakdown, the parallel shift has changed due to the change in the relative position between the fiber and the screen. More bright pointlike emitters appeared outside the emitter physical size boundary due to untangled stray emitters, but the core retained its shape and became brighter and more uniformly distributed carrying more emission current. Altogether, sample A demonstrated the best spatial emission coherence. Therefore, this design may be further optimized to achieve high brightness to

be used as a driving injector for miniature/small size VEDs operated between X- and W- bands.

#### 2.4 Conclusion and Outlook

Field emission microscopy of four different CNT fiber designs is presented. Details of cathode conditioning upon the initial turn on are outlined. It is emphasized that the electrical breakdown plays a critical role in establishing emission performance and operating point of the emitter, typically improving performance in terms of integral *I-E* characteristic in that the turn-on field drops, field enhancement and emission area increase, and the saturation level increases allowing for larger output current. The flat cut fiber geometry enclosed in a supporting tubing was found as a best design. Folded and wound designs either demonstrated lower spatial coherence or greatly suppressed area of emission due to unfolded stray CNT emitters after undergoing conditioning breakdowns; either would deteriorate performance when driving a high frequency VED. The free standing looped design showed weak mechanical stability against breakdown: while still promising additional design considerations must be made to strengthen its stability. Altogether, the new results support earlier findings and provide new insights into performance of the CNT fibers as the material-of-choice for future VED architectures/platforms.

#### **CHAPTER 3**

# CONFIRMATION OF TRANSIT TIME-LIMITED FIELD EMISSION IN ADVANCED CARBON MATERIALS

This chapter is based on the author's published paper: **T. Y. Posos**, Oksana Chubenko, and S. V. Baryshev "Confirmation of Transit Time-Limited Field Emission in Advanced Carbon Materials with a Fast Pattern Recognition Algorithm," *ACS Applied Electronic Materials* **3**.11, 4990 (2021), https://doi.org/10.1021/acsaelm.1c00789.

An accurate estimation of the experimental field emission area remains a great challenge in vacuum electronics. The lack of convenient means, which can be used to measure this parameter, creates a critical knowledge gap, making it impossible to compare theory to experiment. In this chapter, a fast pattern recognition algorithm was developed to complement field emission microscopy, together creating a methodology to obtain and analyze electron emission micrographs in order to quantitatively estimate the field emission area. The algorithm is easy to use and made available to the community as freeware and therefore is described in detail. Three examples of DC emission are given to demonstrate the applicability of this algorithm to determine spatial distribution of emitters, calculate emission areas, and finally obtain experimental current density as a function of the electric field for two technologically important field emitter materials, namely, an ultrananocrystalline diamond and a carbon nanotube fiber. Unambiguous results, demonstrating the current density saturation and once again proving that conventional Fowler-Nordheim theory, its Murphy-Good extension, and the vacuum space charge effect fail to describe such behavior, are presented and discussed. We also show that the transit time-limited charge resupply captures the current density saturation behavior observed in experiments and provides good quantitative agreement with experimental data for all cases studied in this work.

## 3.1 Introduction

Many studies [35, 45–49] have convincingly demonstrated that the electron emission from a large-surface area field emission cathode placed in a macroscopic electric field E is not uniform. The emission area is only a small portion of the total surface area of a cathode, since most of the

emission is confined to a small number of emission spots randomly distributed over the cathode surface. Therefore, a proper and thorough estimation of the apparent emission area and the number of emission locations is essential to quantify field emitters in terms of the current density j and its variation with the applied electric field E. The importance of developing such methodologies is twofold. The first one is practical: an actual emission area needs to be known to compare cathode materials produced by various or varied syntheses. The second one is fundamental: only a properly established j-E (and not I-V) relationship can be used to define the validity range of a classical Fowler-Nordheim (FN) emission and clarify the role of other mechanisms that could cause deviation from the FN emission, that is, cause non-conventional behavior that is being observed across a large body of experimental work [35, 45–53].

A simple and convenient way to measure distribution of electron emission sites is using a luminescence (or phosphor) screen, also known as a scintillator. These screens emit light when they interact with electrons. When such a screen is used as an anode in a field emission experiment, it magnifies and projects an emission pattern formed on the cathode surface under the external field force. When captured using a camera, it creates a micrograph. An experimental system can be designed such that I-V curves can be taken synchronously with micrographs. Then, the micrographs can be used to extract the apparent emission area and obtain the j-E relation. This work is motivated by the lack of a guided micrograph processing for emission area calculations. Here, we present a fast image processing algorithm and demonstrate its application for a thorough analysis of field emission data. Results are presented for micrographs obtained from ultra-nanocrystalline diamond (UNCD) and carbon nanotubes (CNTs) under the applied DC field. These materials exhibit extreme robustness and stability against high electric field loads and produce high electron currents. The method developed in this work to characterize field emission areas from largearea cathodes is necessary for revealing the fundamental material properties of UNCD and CNT cathodes and effective optimization of these cathodes. In the field emission experiments, we use anode screens made of Ce-doped yttrium aluminum garnet (YAG:Ce), which produces a bright green luminescence line at 550 nm. The proposed image processing algorithm is also applicable to

any other phosphor screen that is able to produce spatially separated features that are bright enough.

The algorithm is realized on the MATLAB platform and takes advantage of its strength in processing arrayed data. When compared to an earlier version implemented in Mathematica [35], where a server was required to process extensive sets of micrographs, our present implementation performs 10 times faster on a personal laptop. Additionally, the proposed algorithm is capable of processing micrographs with a strong background gradient glow. The correct subtraction of such kinds of background was extremely challenging or impossible with earlier methods. It means that it could find widespread applications in the field emitter research and development domain. More specifically, the proposed method enables better quantification of the experimental current density, thus narrowing the existing gap between theory and experiment, and allows for consensual evaluation of performance of various field emitters. The image processing code is open-source software: the first and future releases with examples and the user manual can be found in our GitHub page (see ref [54]).

This paper is organized as follows. A brief description of experimental methods is given in Section 3.2. A thorough description of the mathematical background and implementation details of the image processing algorithm are given in Section 3.3. In Section 3.4, we emphasize the importance of the established image processing framework to capture non-conventional field emission behavior of semiconducting nanodiamond and carbon nanotube materials. Semiconductors and semimetals have long been known to violate the classical field emission law [20, 35, 55–59]. Our approach makes it possible to establish quantitative relation between the applied electric field and experimental field emission current density and therefore allows us to verify theory against experiment directly. Results and findings of this chapter are summarized in Section 3.5.

# 3.2 Experimental Methods

In this work, we study field emission characteristics of two scientifically and technologically important materials: the nitrogen-incorporated UNCD and the CNT fiber.

A thin polycrystalline diamond film for the UNCD cathode was grown on a stainless-steel (SS) substrate, 4.4 mm in diameter, as described in ref [35], using a chemical vapor deposition method

that took the feedstock gas mix of  $CH_4/Ar/N_2$ . The chemical bonding was confirmed with Raman spectroscopy. The film had cauliflower-like morphology as expected from an  $sp_2$ -rich diamond film.

The fibers forming the CNT cathode were obtained from DexMat, Inc. They were fabricated using a wet-spinning technique described in detail in ref [18]. The resulting fibers were 90  $\mu$ m in diameter. Hundreds of such fibers were braided and twisted together to form a yarn 200  $\mu$ m in diameter. Two yarns were folded together and inserted in a hollow metal tube, 3 mm in diameter, and electrically connected to the tube walls and the base plate with silver paste, forming the cathode.

The cathode assemblies were placed across a custom-developed imaging screen in a home-developed field emission microscope [1]. The imaging screen was electrically isolated from the grounded chamber body with a brazed conflat flange quartz tube break adapter, where the screen was then positively biased. A Keithley source/meter instrument was used to measure *I-V* curves. A Canon DLSR camera was placed behind a view port to collect emission images. The measurement and data acquisition process involving the camera and the source/meter instrument were fully automated using a NI DAQ microcontroller in a way that allowed us to acquire *I-V* curves and emission images concurrently and synchronously. Therefore, the detected emission current for a given voltage could be assigned to a very specific emission pattern on the screen for further image processing and interpretation. The interelectrode gap for the CNT cathode was 1 mm, and it was 100 µm for the UNCD cathode.

# 3.3 Image Processing Algorithm

## 3.3.1 Feature Extraction

As shown in the examples given in Figures 3.1A, 3.4A, and 3.6A, field emission patterns can vary a lot, with an additional challenge being a bright halo background, which complicates image analysis. However, after a closer look at these images, one notices that the patterns consist of bright spots separated spatially enough to distinguish them visually. Therefore, the strategy is to detect the brightest pixel within each emission spot, which is further referred to as a local maximum (LM). Then, the number of electron emission sites is equal to the LM count, and the emission area can be

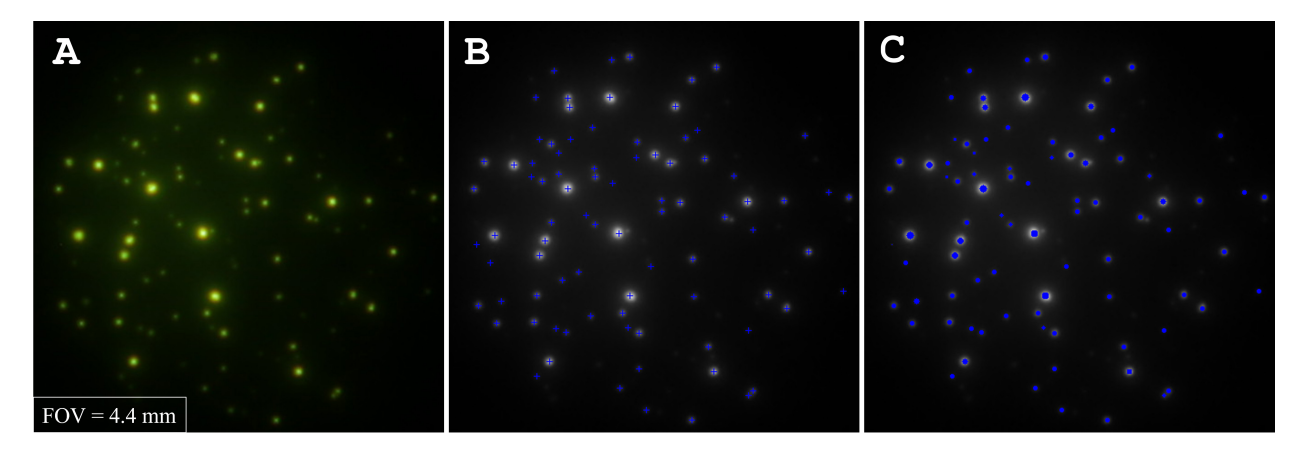


Figure 3.1 (A) Typical micrograph obtained from an UNCD film under the applied DC field [35]. A  $450 \times 450 \,\mathrm{px^2}$  image represents a projection of spatial distribution of electron emission sites onto a YAG anode placed  $106 \,\mu\mathrm{m}$  from a  $4.4 \,\mathrm{mm}$ -diameter cathode. The FOV seen in the micrograph is  $4.4 \times 4.4 \,\mathrm{mm^2}$ . (B) Detected LMs (shown with blue plus signs) overlaid with emission spots shown on the micrograph. (C) Emission pixels (shown in blue), which represent the projected emission area, overlaid with emission spots shown on the micrograph.

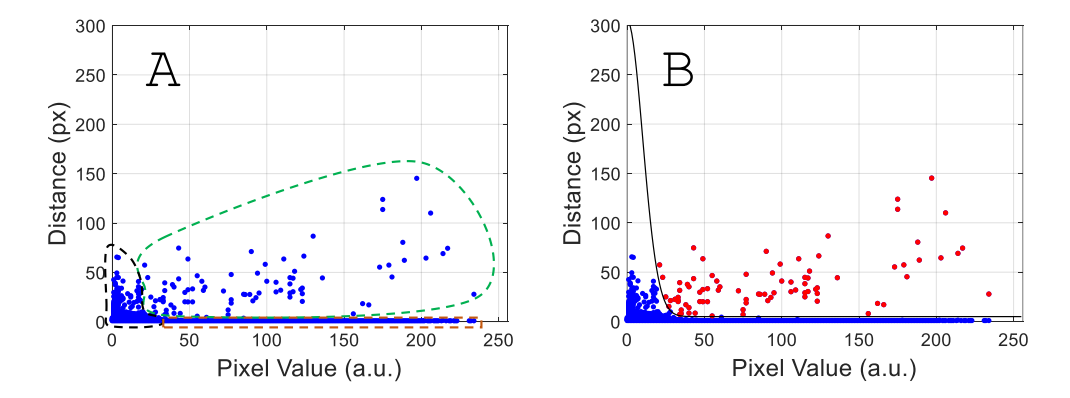


Figure 3.2 (A) Decision plot of extracted features for the micrograph obtained from an UNCD cathode operated under the DC field. The unit of the distance is pixel (px), and the unit of the pixel value is arbitrary (a.u.). Green, black, and brown dashed regions show locations of LMs, background pixels, and emission pixels in the decision plot, respectively. There is no overlapping between an LM cluster and a uniform background. (B) The black curve shows the Gaussian decision boundary. The pixels shown in red are classified as LMs.

estimated by assembling certain neighbor pixels around LMs.

Prior to numerical analysis, an RGB micrograph is converted into a gray-scale format and represented with a 2D matrix of pixels. The intensity of each pixel is given by an integer between 0 and 255. When a typical micrograph (Figure 3.1A) is represented as a 3D plot (Figure 3.3), it can be seen that emission spots appear as Gaussian peaks atop a certain background. LMs are the

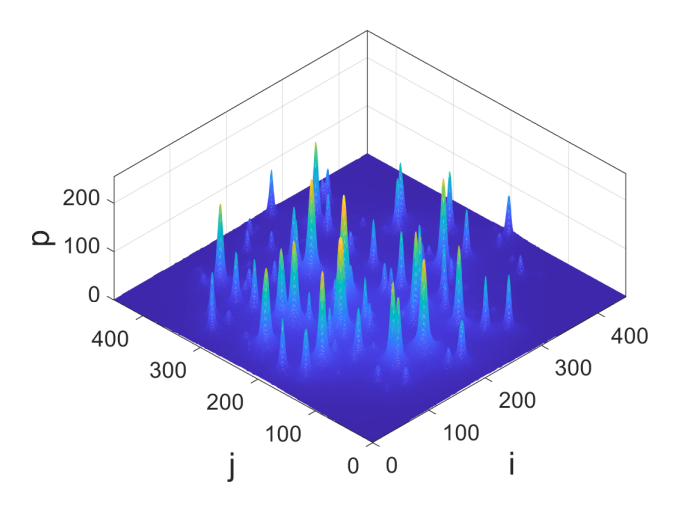


Figure 3.3 3D plot of the micrograph shown in Figure 3.1A. i and j axes are pixel coordinates, and the p axis is for the pixel value.

brightest pixels of each Gaussian peak, and they are also well separated in space. Therefore, two features must be known for each pixel in order to define LMs: pixel value and the distance to the nearest brighter pixel. Because pixels are represented by integers, occurrence of more than one LM for each peak is possible. In order to prevent this, a small random noise between 0 and 0.1, excluding 0 and 0.1, is added to the image, so that there are no identical pixels in the data array. This procedure does not perturb the image because the original image can be retrieved any time by rounding the matrix.

A pixel a with spatial coordinates  $(i_a, j_a)$ , where  $i_a$  is the row number and  $j_a$  is the column number in a 2D array of the digitized image, will be represented by  $(p_a, d_a)$  in a feature space, where  $p_a$  is the intensity feature and  $d_a$  is the distance feature.  $p_a$  is just a pixel value (an integer, typically between 0 and 255), which can be simply extracted from a data array (before adding the noise).

A fast method of extracting the distance feature is searching for a brighter neighbor in a certain neighborhood of each pixel, which is called the search region [60, 61]. The search region must be large enough to enclose an entire Gaussian-like peak but small enough to enclose not more than one entire Gaussian peak. All images presented in this work were  $450 \times 450 \,\mathrm{px^2}$ . Although the size of emission spots varied, two standard deviations of each Gauss peak corresponded to 10 pixels or less. At the same time, the distance between peaks was 20 pixels or more. Therefore,

a circular search region was chosen: centered around each pixel, the search region radius was set to 10 pixels. It should be noted that for different images or image sizes, this value may have to be adjusted accordingly. The Euclidean distance between any two pixels a' at  $(i_{a'}, j_{a'})$  and a at  $(i_a, j_a)$  is defined as

$$d_{a'a} = \sqrt{(i_{a'} - i_a)^2 + (j_{a'} - j_a)^2}$$
(3.1)

If  $s_a$  is the search region for a pixel a carrying a value of  $p_a$  and a pixel b carrying a value of  $p_b$  contained inside the  $s_a$  is the next closest pixel to the pixel a such that  $p_b > p_a$ , the distance  $d_a$  assigned to the pixel a is

$$d_a = \sqrt{(i_a - i_b)^2 + (j_a - j_b)^2}$$
(3.2)

If no other brighter pixel was found in a search region, the brightest pixel is called as the maximum in the search region (MISR). There is a distance property that can be defined for a MISR as the distance to another closest MISR that is brighter than the former. For example, pixel A with a value of  $p_A$  is the MISR in its own search region  $s_A$ , and pixel B with a value of  $p_B$  is the MISR in its own search region  $s_B$ , and  $s_B > s_B$ , if  $s_B = s_B$  is the MISR closest to pixel  $s_B = s_B$ , the distance  $s_B = s_B$  is the MISR closest to pixel  $s_B = s_B$ .

$$d_A = \sqrt{(i_A - i_B)^2 + (j_A - j_B)^2}$$
(3.3)

The brightest pixel across the entire image is the global maximum (GM). There is a distance value that is assigned to the GM. It is the distance to the closest MISR (regardless of its value). Considering that pixel GM with a value of  $p_{GM}$  is the GM and pixel A with a value of  $p_A$  is a MISR, closest to GM, the distance assigned to the GM is

$$d_{\text{GM}} = \sqrt{(i_{\text{GM}} - i_A)^2 + (j_{\text{GM}} - j_A)^2}$$
(3.4)

After all these distances are extracted and recorded, the random noise added earlier gets removed. The code stores both  $(p_a, d_a)$  and  $(i_a, j_a)$  pairs for every pixel. Scatter plots of intensity-distance arrays, which correspond to emission micrographs from UNCD (Figure 3.1A) and CNTs (Figure 3.4A), are presented in Figures 3.2A and 3.5A, respectively. Such plots are called as decision plots, also known as plots of features in the machine learning literature.

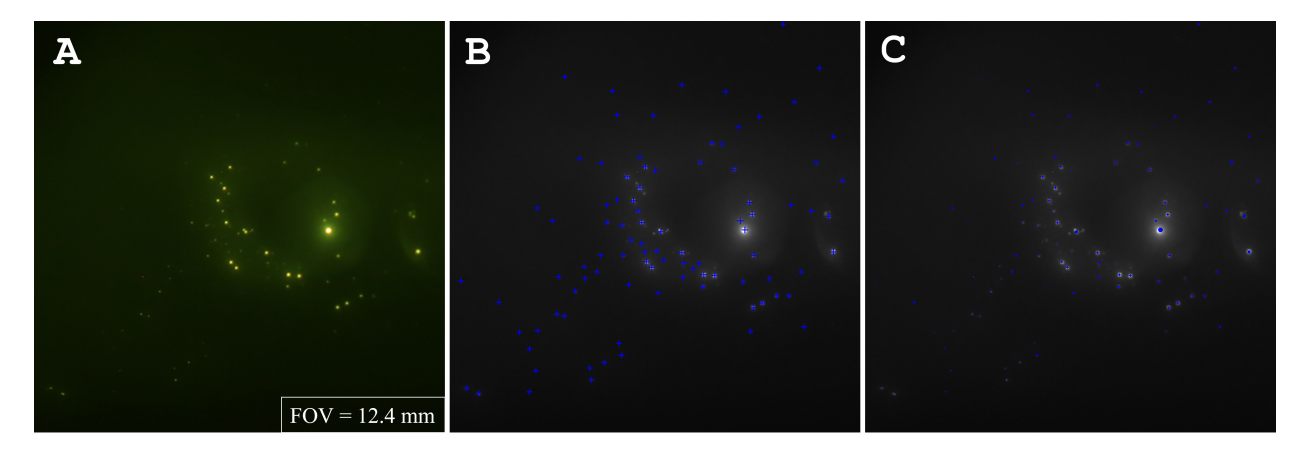


Figure 3.4 (A) Typical micrograph obtained from a CNT fiber under the DC field. The FOV seen in the micrograph is  $12.4 \times 12.4 \,\mathrm{mm^2}$ . (B) Detected LMs (shown with blue plus signs) overlaid with emission spots shown on the micrograph. (C) Emission pixels (shown in blue), representing the projected emission area, overlaid with emission spots shown on the micrograph.

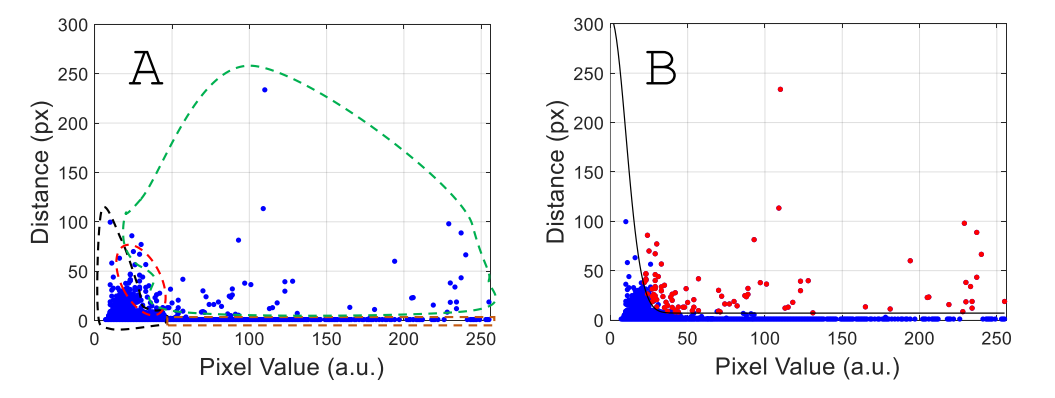


Figure 3.5 (A) Decision plot of extracted features for the micrograph obtained from a CNT fiber under the DC field. Green, black, and brown dashed regions show locations of LMs, background pixels, and emission pixels, respectively. The red dashed region shows overlapping between LMs and a background cluster. (B) The black curve is the applied Gaussian decision boundary. Red points are detected LMs. Notice that not all points above the boundary are red; this is because some false LMs were filtered out.

## 3.3.2 Decision Boundary

Both the density of emission spots and their intensity increase with the applied electric field. Moreover, the background (often non-uniform) arises due to a large number of bright glowing spots. As a result, an analysis of decision plots becomes more complicated. For example, two peaks can be located very close to each other, so the distance feature of a fainter peak becomes very close to or lower than the set distance boundary. Otherwise, let us say that there are fairly faint but distinct emission spots atop a bright background. In this case, there is no clear boundary between the intensity of emission spots and the intensity of background pixels. Moreover, some background protrusions can be mistaken as LMs. Therefore, an effective method for estimating an appropriate decision boundary is required to identify LMs on the decision plot.

A supervised machine learning using labeled data cannot be used for this class of problems because labeling hundreds of images with hundreds of emission spots is not feasible. In addition, micrographs vary a lot for different materials and geometries or evolve with a high dynamic range throughout a single experiment. An unsupervised machine learning scheme might be used. However, as seen from Figures 3.2A and 3.5A, no distinct clusters form on the decision plots. Therefore, a simple and robust approach using a tunable decision boundary of a certain form is attempted here.

For pixels that come from a continuous low background (intense and high-gradient background case will be discussed later), the algorithm finds a brighter pixel less than a few pixels away. Thus, these background pixels are characterized by a small distance  $d_a$  and a small intensity  $p_a$ . As a rule, the background pixels outnumber the emission spot pixels. Therefore, most of the background pixels lie near the origin and appear as crowded clusters encircled by black dashed loops in Figures 3.2A and 3.5A. Some pixels that belong to emission spots are also characterized by small distances (less than the radius of the search region), but most of them are brighter than the background, and their pixel values are large, up to 255. Therefore, these pixels form stretched clusters at the bottom of decision plots, as shown by brown dashed regions in Figures 3.2A and 3.5A.

LMs are bright pixels separated from brighter pixels by large distances (usually larger than

the search radius). They are shown by dashed green regions in decision plots. If the background is low and uniform (as in the case shown in Figure 3.1A), LMs can be easily separated from background pixels (see the green dashed region in a corresponding decision plot in Figure 3.2A). However, when a stronger background appears with a distinct gradient across the image plane as shown in Figure 3.4A, there are relatively faint emission pixels that are barely noticeable on a bright background. In Figure 3.5A, these pixels are shown inside the red dashed region and are intermixed with background pixels. To separate LMs from the background, we use a Gaussian decision boundary given by

$$f(p_a) = A \cdot e^{-\frac{(p_a - \mu)^2}{2\sigma^2}} + k$$
 (3.5)

where A is the amplitude,  $\mu$  is the mean,  $\sigma$  is the standard deviation, and k is the offset. Functions, which define decision boundaries for micrographs in Figures 3.1A and 3.4A, are shown in Figures 3.2B and 3.5B, respectively. The decision rule is as follows. Consider a pixel a carrying the pair of values  $(p_a, d_a)$ . If  $d_a > f(p_a)$ , the pixel a is a LM. The parameters A,  $\mu$ ,  $\sigma$ , and k can be adjusted for each dataset. If the background and LM pixels are mixed as shown by the red dashed region in Figure 3.5A, many background pixels are detected as LMs. One way to fix it is to increase  $\sigma$  to exclude background pixels from the LM list. In a case when the density of emission spots is high (emission spots and thus LMs are spatially very close to each other), decreasing k helps to identify some missing LMs. The distance feature  $d_a$  was never greater than 300 for  $450 \times 450 \,\mathrm{px}^2$  images. Thus, the parameter A was kept at the value of 300 for all datasets presented. Mean  $\mu$  was set to zero for all datasets. Any false LM can be further filtered out by applying the surface-fitting method given in Section 3.3.3. Therefore, a crude adjustment of the decision boundary parameters is enough.

Decision boundaries shown with black curves in Figures 3.2B and 3.5B were applied to Figures 3.2A and 3.5A, respectively. Then, false LMs were filtered out by the surface-fitting method. A final list of detected LMs is labeled with red data points on the decisions plots in Figure 3.2B and Figure 3.5B, and with blue crosses in Figures 3.1B and 3.4B. These examples illustrate nearly perfect LM detection.

#### 3.3.3 Emission Area

As it was already mentioned, each emission spot on a micrograph (e.g., Figure 3.1A) appears on a 3D plot (Figure 3.3) as a quasisymmetric Gaussian with its center at a LM. Once a LM is detected, a 2D Gaussian function can be used to fit an intensity peak [62, 63]. The fitting function, which returns the estimated pixel value  $p_{ij}^e$  for a pixel at the position (i, j), is given by

$$p_{ij}^{e} = A_s \cdot e^{-\frac{(i-i_{LM})^2 + (j-j_{LM})^2}{2\sigma_s^2}} + C$$
(3.6)

where  $A_s$  is the amplitude,  $\sigma_s$  is the standard deviation, C is the offset to manage the background level, and  $(i_{LM}, j_{LM})$  is the position of a given LM. Fitting parameters  $A_s$ ,  $\sigma_s$ , and C have to be determined for each LM. A  $15 \times 15 \,\mathrm{px^2}$  region was chosen to fit each peak centered at the position  $(i_{LM}, j_{LM})$ , so  $i_{LM} - 7 \le i \le i_{LM} + 7$  and  $j_{LM} - 7 \le j \le j_{LM} + 7$ . Such a fitting region is optimal for our images because it ensures that only one emission spot is included. The fitting parameters for each LM can be calculated via minimizing the following sum by the least-squares regression method

$$\sum_{i} \sum_{j} (p_{ij} - p_{ij}^{e})^{2} \tag{3.7}$$

where  $p_{ij}$  is the original pixel value and i and j are the indices running over the fit region of each LM.

Obviously, most of the bright pixels will fall within one standard deviation of the mean. To classify a pixel a, which is located at  $(i_a, j_a)$  within a fit region centered at a LM at  $(i_{LM}, j_{LM})$ , as the emission pixel that contributes toward the emission area calculation, the following condition must be satisfied

$$(i_a - i_{LM})^2 + (j_a - j_{LM})^2 < \sigma_s^2$$
(3.8)

Alone, this condition is not enough to classify a pixel as the emission pixel. For example, consider the case when a background pixel is incorrectly detected and listed as a LM (called a false LM in Section 3.3.2). The Gaussian fit of the region around such a false LM will yield a large standard deviation  $\sigma_s$  but small amplitude  $A_s$ . This allows for filtering out fake LMs by applying

threshold values for  $A_s$  and  $\sigma_s$ . LMs, which satisfy the condition

$$(\sigma_s > \sigma_{\text{th}}) \lor (A_s < A_{\text{th}}) \tag{3.9}$$

are not real LMs, and they are discarded from the master LM list. Thus, they do not contribute to the local maximum count and the emission area calculation.

For the micrographs presented in this work,  $\sigma_{th} = 7$  and  $A_{th} = 10$  are chosen. For cases when spots are faint,  $A_{th}$  should be decreased for the spots to be detected. If the background noise is high,  $\sigma_{th}$  should be decreased to produce reliable results. In Figures 3.1C and 3.4C, the blue pixels identified as the emission pixels are overlaid with the emission spots shown in Figures 3.1A and 3.4A, respectively. If the physical area of the image is known, the apparent emission area is given by

Emission area (mm<sup>2</sup>) = Image area (mm<sup>2</sup>) 
$$\times \frac{\text{Number of emission pixels}}{\text{Total number of pixels}}$$
 (3.10)

Both Figures 3.1A and 3.4A have  $450 \times 450 = 202$ , 500 pixels. There are 1929 emission pixels in Figure 3.1C and 349 emission pixels in Figure 3.4C. The displayed portion of a YAG:Ce screen in Figures 3.1A and 3.4A has the area of  $4.4 \times 4.4$  and  $12.4 \times 12.4$  mm<sup>2</sup>, respectively. Then, applying eq 3.9, the apparent emission area is 0.814 mm<sup>2</sup> for UNCD (Figure 3.1) and 0.264 mm<sup>2</sup> for CNTs (Figure 3.4), while the total cathode surface area available for emission is 15.2 mm<sup>2</sup> for UNCD and 4.71 mm<sup>2</sup> for CNTs.

## 3.3.4 Micrographs with Intense Backgrounds

Micrographs with intense and non-uniform backgrounds are extremely challenging to process and analyze. One such example is shown in Figure 3.6A. In this micrograph, the global background changes from dark at the top to very bright at the bottom, where the detection of emission spots becomes less effective. A corresponding decision plot is shown in Figure 3.7A. Unlike previous cases (Figures 3.2 and 3.5), the background pixels do not cluster near the origin, but instead, they are distributed over a wide range of pixel values (shown by a black dashed region in Figure 3.7A). There are well-separated bright pixels, corresponding to LMs, shown by a green dashed region. Because some of the glowing background pixels have values comparable or higher than those of

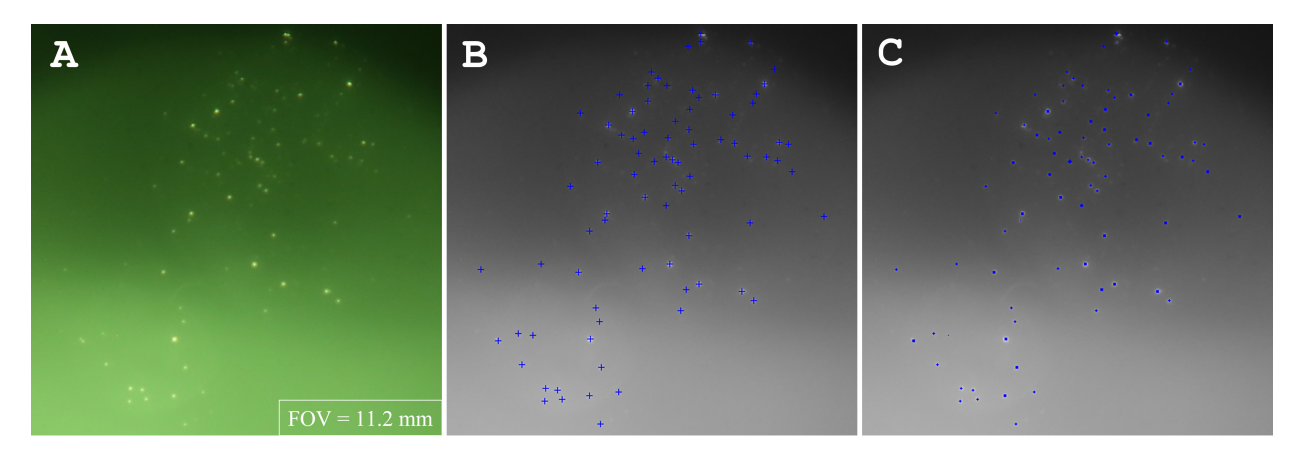


Figure 3.6 Typical micrograph obtained from a CNT fiber under the DC field with a glowing high-gradient background. The emission domains appear as bright peaks on the glow. The exact source of the glow is unknown. The FOV seen in the micrograph is  $11.2 \times 11.2 \,\mathrm{mm^2}$ . (B) Detected LMs (shown with blue plus signs) overlaid with emission spots shown on the micrograph. (C) Emission pixels (shown in blue), representing the projected emission area, overlaid with emission spots shown on the micrograph.

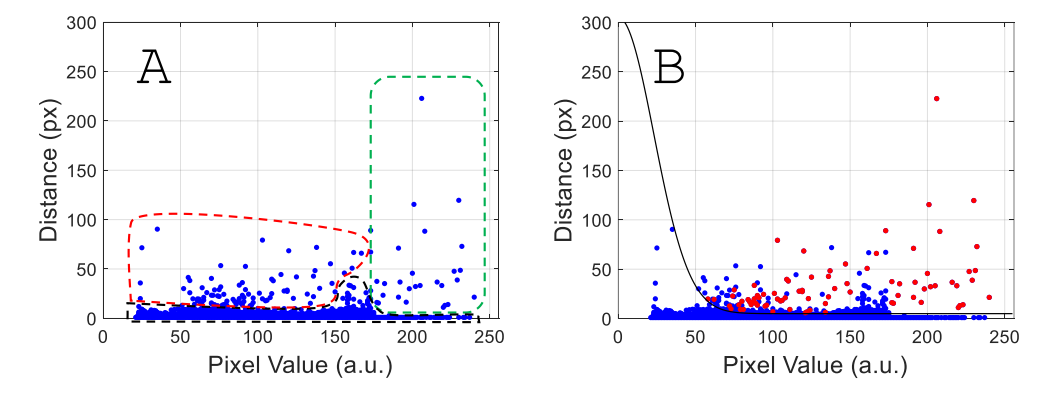


Figure 3.7 (A) Decision plot of extracted features for the micrograph obtained from a CNT fiber under the DC field with a glowing high-gradient background. Unlike the previous cases, the background does not form a cluster. Instead, it is distributed over a wide pixel range shown in a black dashed region. The green dashed region consists of well-separated LMs. The red region includes both background pixels and LMs, so the boundary should be drawn so that the region includes all candidate LMs. Any false LMs are to be filtered out by Gaussian surface fitting. (B) A black curve shows the applied decision boundary. All points above the curve are candidate LMs. Red points label the finalized LM list after false LMs are filtered out by the surface fitting.

some of the emission pixels, there is also a large region, shown by a red dashed line, where LMs and background pixels are intermixed.

It is important to note that any LM, excluded during the decision-making procedure, cannot be recovered at later stages of the image analysis. However, any background pixel, identified and

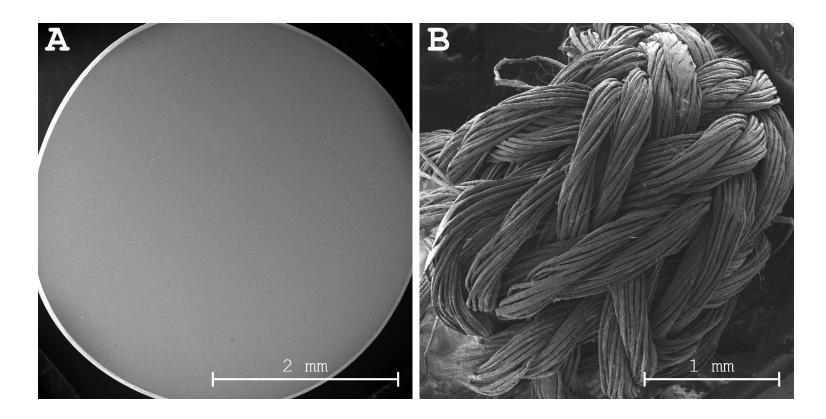


Figure 3.8 (A) SEM image of the UNCD film grown on a Ni/Mo/SS substrate. (B) SEM image of the CNT fiber. The twisted and folded yarn structure is clear from the image.

included as a LM, can be filtered out by the surface-fitting procedure. Therefore, the decision boundary should be soft, that is, it should include all possible LM candidates (as opposed to a rigid boundary that would exclude as many background pixels as possible). According to this approach, the decision boundary should be drawn on the decision plot (Figure 3.5) in such a way that the pixels from a red region are considered as LM candidates. Any false LM will be likely filtered out. One major drawback of applying the soft boundary is the increased computation time due to an increased number of Gaussian fitting steps required for an increased number of LMs. With the decision boundary applied in Figure 3.7B, all pixels above the black curve are LM candidates. Figure 3.7B highlights in red a finalized array of LMs (after most or all false LMs were removed). The same points are overlaid on the original image as blue crosses in Figure 3.6B. Nearly perfect agreement can be seen upon visual inspection. Finally, Figure 3.6C shows in blue the calculated apparent emission area. One can see how effectively the entire pattern recognition workflow performs even for images highly distorted by the background. The calculated number of emission pixels is 533 out of 202, 500 pixels. The field of view (FOV) in Figure 3.6A is 11.2 × 11.2 mm², yielding an emission area of 0.33 mm², while the total cathode area is 15.2 mm².

#### 3.4 Results and Discussion

In this section, we used the described algorithm to extract the electron emission area projected on the YAG screen, which is the apparent emission area, and estimated the experimental current density as a function of the electric field. We analyzed three sets of field emission micrographs.

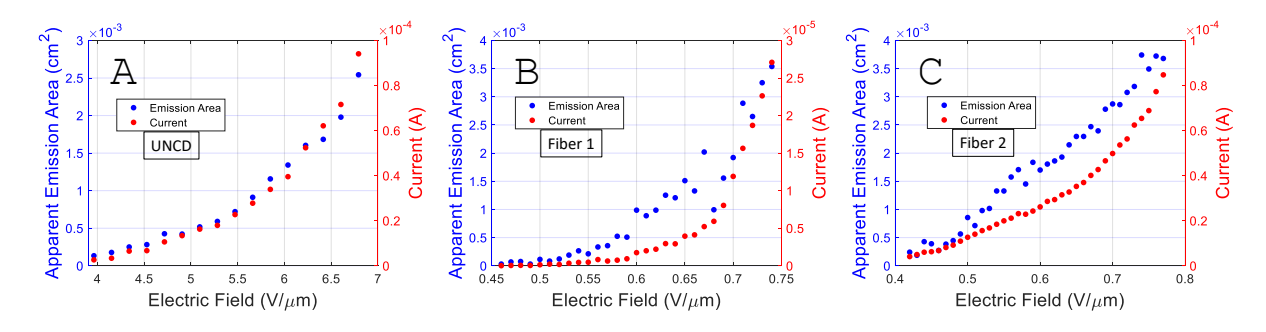


Figure 3.9 Apparent emission area estimated using the algorithm (blue dots) and the measured current (red dots) as a function of the applied electric field (A) for the UNCD film, (B) for the CNT fiber before conditioning, and (C) for the CNT fiber after conditioning.

Each set contains tens of micrographs taken with regular intervals as the applied voltage (and the electric field) was swept up and down. The current was measured concurrently. The first set is obtained from the n-type UNCD film grown on a planar SS substrate with a Ni/Mo buffer layer [35]. The second and third sets are from the CNT-folded rope taken before and after conditioning, respectively. The sample was formed by braiding and twisting 90 µm fibers, then folding the resulting yarn multiple times, and inserting it in a metal tube [45]. Scanning electron microscopy (SEM) images of the samples are given in Figure 3.8.

Electric field dependencies of the apparent emission area  $S_{apparent}$  computed for the considered datasets are presented with blue dots in Figure 3.9. In the same figure, red dots trace the corresponding field dependencies of the measured current  $I_{measured}$ . The apparent emission area is not the actual emission area. The apparent emission area estimated using the algorithm is the projected or magnified emission area. The magnification occurs as a result of the non-zero finite transverse momentum of emitted electrons and the transverse component of the fringe electric field on the surface of the high-aspect ratio features. Therefore, the relation between the apparent emission area and the real emission area can be obtained by introducing the magnification factor. Although finding the factor is not a straightforward process (because it depends on both internal material parameters and complicated surface geometry), the lower and upper limits of the experimental current density can be easily estimated.

The lower limit of the current density can be found by dividing the measured current  $I_{\text{measured}}$ 

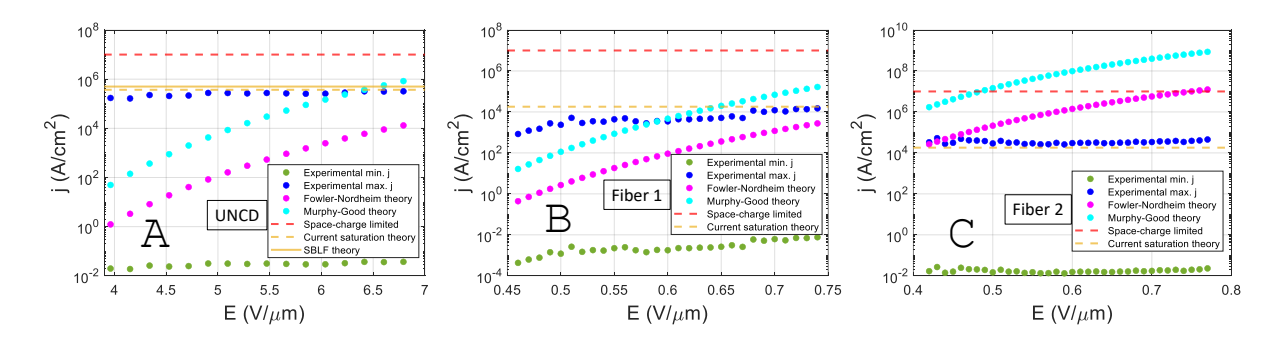


Figure 3.10 Experimental current densities (the lower limit is shown with green dots; the upper limit is shown with blue dots) compared with the theoretical estimations (the elementary FN equation is shown with magenta dots; the MG extension is shown with cyan dots) and the space charge limited emission (dashed red line) and the transit time-limited emission (dashed orange line) as a function of the applied electric field (A) for the UNCD film, (B) for the CNT fiber before conditioning, and (C) for the CNT fiber after conditioning.

by the total apparent emission area  $S_{\text{apparent}}$  estimated using the algorithm for a given electric field E

$$j_{\text{exp.min}} = \frac{I_{\text{measured}}}{S_{\text{apparent}}}$$
 (3.11)

The lower current density limits  $j_{\text{exp.min}}$  for all three datasets are shown with green dots in Figure 3.10. It can be seen that the current density  $j_{\text{exp.min}}$  does not change significantly with the applied electric field. This happens because the variation in the apparent emission area with the applied electric field is almost identical to that of the measured current (Figure 3.9). Such behavior is observed for all datasets and contradictory to the FN law [64], which predicts the exponential increase in the current density with the applied electric field.

Furthermore, the upper limit of the current density can be calculated using an estimated angle of the beam ray trajectory. If the angle is  $\alpha$ , a point-like single emission site with area  $S_{\text{single}}$  appears on the YAG:Ce screen as  $S_{\text{single apparent}}$ , given by

$$S_{\text{single apparent}} = \pi (d \tan \alpha)^2$$
 (3.12)

where d is the interelectrode gap. Geometrically, the angle  $\alpha$  can be obtained using the mean transverse energy (MTE) as [45]

$$\tan \alpha = \frac{p_x}{p_z} = \sqrt{\frac{2 \cdot \text{MTE}}{\text{m}_0 \text{c}^2}} \frac{1}{v/\text{c}} \frac{1}{\gamma}$$
(3.13)

where  $p_x$  and  $p_z$  are transverse and longitudinal momentum,  $m_0c^2 = 0.511$  MeV is the electron rest energy, v/c is the ratio of the electron speed to the speed of light, and  $\gamma$  is the Lorentz factor. At 1 keV energy, v/c and  $\gamma$  are taken as 0.063 and 1, respectively. MTE values are 100–200 meV [65, 66] for the UNCD. For CNTs, its Fermi energy of 50–100 meV [67] can be used as MTE. Then, the estimated values of the angle are 0.9° for the UNCD sample [68] and 0.4° for the fiber sample [45]. Then, the inverse magnification factor is given by the ratio  $S_{\text{single}}/S_{\text{single apparent}}$ , and the current density can be calculated as

$$j_{\text{exp.max}} = \frac{I_{\text{measured}}}{\frac{S_{\text{single}}}{S_{\text{single apparent}}} \cdot S_{\text{apparent}}}$$
(3.14)

To obtain the upper current density limit, the minimum possible size for  $S_{\text{single}}$  should be chosen in Eq 3.14. Therefore, we assume  $S_{\text{single}}$  to be equal to the size of grain boundaries (1 nm by 1 nm square [68]) for UNCD and the size of a single CNT (10 nm-diameter circular region) for the fiber. The resulting upper limits for the three datasets are shown with blue dots in Figure 3.10. A few important conclusions can be made. First, experimental current densities are practically constant in the studied range of electric fields. Therefore, an increase in current with the electric field can be explained by an increase in the emission area (see Figure 3.9). Second, according to Dyke et al. [69], above the  $10^7 \,\text{A/cm}^2$  current density level, the emission is limited by the space charge, which causes a decrease in the effective field over the cathode. The current density limit due to the space charge is shown by a red dashed line for reference in Figure 3.10. However, we find that the upper limit of experimental current density is much lower than this value. Therefore, the saturation behavior cannot be explained by the space charge effect.

We also compared our results with predictions given by field emission theory in both FN and MG formulations. In the FN formulation, the image charge effect is ignored, and the potential barrier at the material-vacuum interface can be approximated using a simple triangular potential. In this case, the FN current density  $j_{FN}$  (A/m<sup>2</sup>) is given by [64, 70]

$$j_{\text{FN}} = A \frac{1}{\phi} (\beta E)^2 e^{-\frac{B\phi^{3/2}}{\beta E}}$$
 (3.15)

where A =  $1.54 \times 10^{-6}$  A eV/V<sup>2</sup>, B =  $6.83 \times 10^{9}$  V/eV<sup>3/2</sup> m,  $\beta$  is the unitless field enhancement

factor,  $\phi$  (eV) is the material work function, which can be taken as 4.8 eV for both UNCD and fiber samples, and E (V/m) is the electric field.  $\beta$  can be obtained from experimental data by plotting it in FN coordinates, where the x-axis is 1/E and the y-axis is  $\ln(j/E^2)$ . The plot forms a distinct knee point for non-metal and semimetal emitters [35, 45], that highlights the saturation behavior in its high-field region. After fitting its low-field region with a line as in Ref [45], the slope m is given by

$$m = -\frac{\mathrm{B}\,\phi^{3/2}}{\beta}\tag{3.16}$$

from where  $\beta$  can be extracted. The resulting current density curves are shown with magenta dots in Figure 3.10.

A better theoretical approach is taking the image charge effect into account. In this case, the surface potential barrier is given by a rounded triangular barrier, and the current density is given by the Murphy-Good (MG) current density  $j_{MG}$  (A/m<sup>2</sup>) [34, 70–74]

$$j_{\text{MG}} = A \frac{1}{t_{\text{F}}^2 \cdot \phi} (\beta E)^2 e^{-\nu_{\text{F}} \frac{B \phi^{3/2}}{\beta E}}$$
 (3.17)

where A and B are the same constants as before and  $t_F$  and  $v_F$  are special field emission elliptic functions of the unitless Nordheim parameter y, given by [72, 74]

$$y = k \cdot \frac{1}{\phi} \sqrt{\beta E} \tag{3.18}$$

where  $k = 3.79 \times 10^{-5}$  eV m<sup>1/2</sup>/V<sup>1/2</sup> and E and  $\phi$  are in terms of V/m and eV, respectively. Once it is plotted in FN coordinates, it produces the slope m given by

$$m = -s_{\rm F} \frac{\mathrm{B} \,\phi^{3/2}}{\beta} \tag{3.19}$$

where  $s_F$  is the slope correction factor. Although  $v_F$ ,  $t_F$ , and  $s_F$  are not trivial to calculate, they had been tabulated well [75], and simple good approximations are given by [76]

$$v_{\rm F} = 1 - y^2 + \frac{1}{3}y^2 \ln y \tag{3.20}$$

$$t_{\rm F} = 1 + \frac{1}{9}(y^2 - y^2 \ln y) \tag{3.21}$$

$$s_{\rm F} = 1 - \frac{1}{6}y^2 \tag{3.22}$$

For a typical range of applied fields and the work function of  $4.8 \,\mathrm{eV}$ ,  $s_{\mathrm{F}}$  and  $t_{\mathrm{F}}$  can be adequately taken as 0.95 and 1, respectively [75, 77]. Then,  $\beta$  can be extracted from Eq 3.19 after plotting experimental data in FN coordinates and applying the previous procedure. By substituting the extracted  $\beta$  to Eq 3.18 and using approximation of the Nordheim function given by Eq 3.20,  $j_{\mathrm{MG}}$  in Eq 3.17 can be calculated. The corresponding theoretical current density curves are shown using cyan dots in Figure 3.10. It is obvious that both the elementary FN equation (Eq 3.15) and MG equation (Eq 3.17) fail to explain the saturation trend observed experimentally.

The discrepancy between theory and experiment is due to the fact that FN-type equations are derived for metals where the number of carriers is approaching infinity, surface is equipotential, and resistance on the current path can be ignored. However, this assumption is obviously not valid for non-metal and semimetal emitters: compare the carrier concentration  $\sim 10^{23}\,\mathrm{cm^{-3}}$  in copper to the carrier concentration  $\sim 10^{18}$ – $10^{19}$  cm<sup>-3</sup> in the CNT and UNCD. The development of improved theoretical models that would take semiconductor effects into account is critical. Nevertheless, most studies relate this saturation effect to impurities at the emitter apex [56], space charge effect [20, 21], series contact resistance between the substrate and the emitter [44, 78], and so on. As we stated before, the space charge is not a dominant effect at the current density levels of our interest. Surface adsorbates do not cause saturation for metal emitters, so we believe that it is not an important effect for our samples. Measurements [58] show that the voltage drop due to series contact resistance is small for a typical range of applied potential, so it can also be ruled out. On the other hand, it is proven both experimentally [58] and analytically [79] that a small voltage drop along the emitter body can cause a large drop in the enhancement factor at the emitter apex. The voltage loss along the body can also be modeled by penetration of the field into the sample through defining a certain depletion length W from the emitter surface [39] into the bulk. Such a W is a result of poor screening due to a limited number of charge carriers in non-metallic field emitters. Therefore, the effects of the decrease in the field enhancement factor as a result of voltage loss along the emitter [58, 79] or limited charge supply [39] appear to be better hypotheses. The saturation

current density, that is, the maximum current density that can be extracted from a sample assuming that carriers reach saturation velocity, is given by [39]

$$j_{\text{sat}} = \frac{q_{\text{e}} n^{2/3} v_{\text{sat}}}{W} = \frac{q_{\text{e}} n^{2/3}}{\tau},$$
 (3.23)

where  $j_{\rm sat}\,({\rm A/cm^2})$  is the saturation current density,  ${\rm q_e}=1.6\times10^{-19}\,{\rm C}$  is the electron charge,  $n \, (\mathrm{cm^{-3}})$  is the electron carrier density,  $v_{\mathrm{sat} \, (\mathrm{cm/s})}$  is the saturation velocity,  $W \, (\mathrm{cm})$  is the length of the subsurface depletion region, and  $\tau$  is the transit time, that is, the time it takes for charges to cross over the depletion region and reach the cathode surface to get emitted into vacuum. Typical parameters for the CNT fiber [45] are  $n \sim 10^{18} \, \mathrm{cm}^{-3}$ ,  $v_{\mathrm{sat}} \sim 10^7 \, \mathrm{cm/s}$ , and  $W \sim 8.9 \times 10^{18} \, \mathrm{cm}^{-3}$  $10^{-5}$  cm (890 nm). Then, Eq 3.23 gives  $1.8 \times 10^4$  A/cm<sup>2</sup>, which is shown with an orange dashed line in Figure 3.10B and 3.10C for reference. Another dashed orange line  $3.7 \times 10^5 \, \text{A/cm}^2$  is also drawn for UNCD in Figure 3.10A, where n is taken as  $10^{19} \,\mathrm{cm}^{-3}$ , and W is replaced with the film thickness of 200 nm atop a metal substrate that would terminate electric field lines. An orange solid line is also presented in the same plot. This additional line is based on extended Stratton-Baskin-Lvov-Fursey (SBLF) theory formulated in our previous work (see Ref [68]). In SBLF theory, Poisson's and Stratton's equations are solved self-consistently at the material-vacuum interface. The extended SBLF takes into account the detailed density of states of a material and, importantly, accounts for the effect of field-induced reduction of electron mobility (referred to in this work as the transit time limitation) that plays a central role. The comparison between solid and dashed orange lines suggests that Eq 3.23 can be safely used in the place of detailed and time-consuming SBLF calculations, if fast benchmarking of experimental data is needed.

Figure 3.10 demonstrates that the behavior of real field emitters is significantly different from that dictated by classical field emission theory. First of all, we find that neither the FN nor MG formulation of the j-E relation captures the functional behavior of the studied field emitters, while demonstrating significant disagreement with experimental measurements. Thus, the classical field emission appears to have no relevance toward describing experimental behavior of this class of cathodes (be it a first-time turn-on or a consecutive conditioned operation). Additionally, the 1D vacuum space charge effect (it is obtained from a 1D Child-Langmuir law treatment [69] and thus

provides the lowest boundary for the space charge saturation limit as compared to a 2D case [80]) still overestimates the experimentally observed saturation by 1–3 orders of magnitude.

The transit time-limited field emission model appears to capture the experimentally observed emission characteristics unique to the advanced semiconducting field emission materials, UNCD and CNT. It also correctly explains two major facts important for cathode conditioning ("Fiber 1" and "Fiber 2" case studies in this work). First, despite the fact that the characteristic field emission parameters (e.g., field enhancement factor and turn-on field) may be drastically altered, the current density saturates due to intrinsic material properties and thus remains the same as long as the material itself does not alter during conditioning. Second, it correctly implies that once a semiconductor is depleted, the increase in the output current is only possible if the emission area increases (see the results in Figure 3.9). The emission area grows with the electric field and so does the output current, but the current density remains constant. This creates a sizable misconception when measured *I-V* or *I-E* curves and not *j-E* curves are analyzed using the elementary FN approach.

#### 3.5 Conclusions

In conclusion, we demonstrated that the experimental field emission current density of UNCD and CNT materials remained constant with the applied electric field, demonstrating saturation behavior. These results emphasized that classical FN and MG theories fail to describe fundamental field emission properties of these materials. Moreover, it was shown that the saturation level cannot be explained by external effects such as space charge, surface adsorbates, or contact resistance. Instead, it was found that the transit time-limited field emission, which accounts for the limited carrier concentration and the saturation drift velocity, provides the current density saturation levels very close to the upper limits of experimentally measured ones for all cases studied in this work.

The direct benchmarking between theory and experiment became possible solely thanks to the development of a new pattern recognition algorithm. Application of this algorithm was demonstrated and emphasized by counting the number of field emission sites and calculating the apparent field emission area from DC micrographs. The algorithm is fast. Run on a personal laptop with

Intel i5 2.5 GHz core, the full set of calculations took 23.8 s for Figure 3.1, 18.9 s for Figure 3.4, and 26.3 s for Figure 3.6. It took the longest processing time for Figure 3.6 because a soft decision boundary was used, and false LMs had to be sorted out.

Future work is being focused on unsupervised machine learning, especially one-class support vector machines, to replace the Gaussian decision boundary and thus completely automate the pattern recognition. The current/future releases are/will be available as freeware on GitHub [54]. Video tutorials were uploaded to the GitHub page for future users. The tutorials contain comprehensive details on how to use the code. Many exemplary images were also uploaded to the page to allow users to get familiar with practical code implementations before applying the code to their own micrographs.

#### **CHAPTER 4**

#### BRIGHT SPATIALLY COHERENT BEAM FROM ELECTROPLATED CNT FIBERS

This chapter is based on a paper of the author under review: **T. Y. Posos**, J. Cook, and S. V. Baryshev, "Bright Spatially Coherent Beam From Carbon Nanotube Fiber Field Emission Cathode", *arXiv* 2301.06529 (2023), https://doi.org/10.48550/arXiv.2301.06529

Large area carbon nanotube (CNT) cathodes made from yarns, films or fibers have long been promising as next generation electron sources for high power radio frequency (rf) and microwave vacuum electronic devices. However, experimental evidence have been pointing out spatial incoherence of the electron beam produced by such cathodes that, in turn, impeded the progress toward high brightness CNT electron sources and their practical applications. Indeed, typically large area CNT fibers, films or textiles emit stochastically across their physical surface at large emission angles and with large transverse spread, meaning large emittance and hence low brightness. In this work, using high resolution field emission microscopy, we demonstrate that conventional electroplating of hair-thick CNT fibers followed by a femtosecond laser cutting, producing emitter surface, solves the described incoherent emission issues extremely well. Strikingly, it was observed that the entire (within the error margin) cathode surface of a radius of approximately 75  $\mu$ m emitted uniformly (with no hot spots) in the direction of the applied electric field. The normalized emittance on the fiber surface was estimated of 52 nm with brightness of >10<sup>15</sup>  $\frac{A}{m^2 \text{ rad}^2}$  (or >10<sup>7</sup>  $\frac{A}{m^2 \text{ sr V}}$  estimated for pulsed mode operation.

## 4.1 Introduction

In early 1990's, carbon nanotechnology revolution introduced a plethora of new advanced materials among which the carbon nanotube was notoriously attractive for making nanoscale field effects devices, including vacuum devices. Many labs studied effects associated with field emission from a single CNT or arrays with counted number of isolated CNTs [58, 81–85]. Control over fabrication and emission of single CNT field emission devices was excellent and many field emission devices were demonstrated, e.g. field emission radio [86] or field emission transistor [87], amplifier [88], and many others [84, 85].

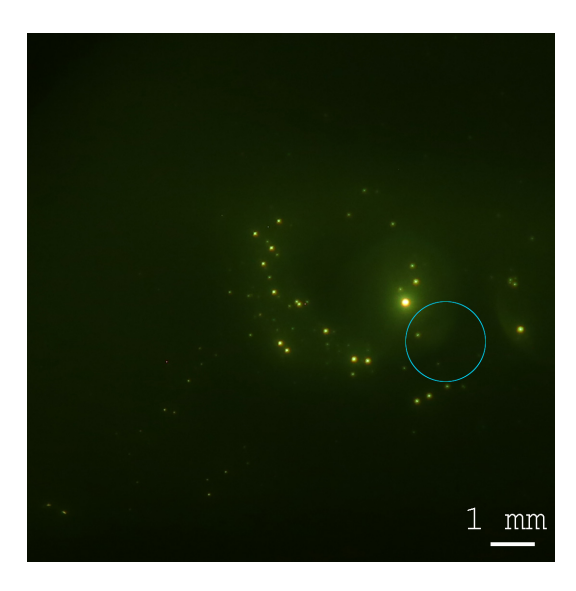


Figure 4.1 Typical micrograph showing large beam transverse spread and nonuniformity. The blue circle marks the cathode's position behind the imaging screen and its size.

In order to increase the output power, macrosocopic large area CNT fibers, films, yarns and fabrics started to be used to increase the operating currents from pico-/nano- to many amperes. Here, CNTs were thought to replace legacy velvets [22]. The multiple benefits of CNT fibers over legacy technology are low turn-on voltage and high emission current at relatively low operating electric field due to inherent high field enhancement factor, and high electrical and thermal conductivities [18]. It was conventionally assumed that emission would be uniform, i.e. uniformity would translate from previously studied arrays of counted CNTs to the large area CNT fibers. However, recent studies that employed field emission microscopy illustrated that emission is never uniform and moreover that the emission area is a function of the electric field (making it cumbersome for calculating current densities.) Fig.4.1, reproduced from our past work [45], highlights other important issue of the large transverse spread of the emitted beam where beam lands on the imaging screen millimeters away from the physical location of the cathode source (blue circle) after travelling only a millimeter between the cathode and the anode. This clearly points out a very large emittance and therefore very low brightness, making CNT fiber cathodes impractical for applications like rf or microwave traveling wave tubes (operating in GHz range), microscopy and bright X-ray sources for medicine or active scanning. Another issue arises from that—because all the current emerges from a few

active spots, it leads to local heating, microbreakdowns [45] and short-lived cathodes.

After experimenting with many fiber arrangements, we found that loose tiny singular fibrils (comprising braided fibers) resulted from thermal and field related stress [32, 45], which eventually focus the field due to their high aspect ratio and become point-like randomized intense electron emitters eventually exploding (seen as micro-breakdowns) and re-populating surrounding areas with more new-born fibrils. This process repeats itself until the cathodes stops operating while emission always look like a family of single electron rays going in many directions that are not aligned with the desired main longitudinal propagation direction, such as in Fig.4.1. To mitigate this issue, hypothesised to be the major problem, we study new cathode production technology where fibers are electroplated with Ni and laser cut; all to suppress the fibril occurrence and regeneration. Through experimental measurements and electrostatic and beam dynamics modeling, emission uniformity and beam brightness were analyzed.

## 4.2 Experimental

To prepare the field emission CNT fiber cathodes, a commercially available CNTs fiber from DexMat, Inc was used. The fiber is made by a wet-spinning technology [18]—pre-grown arrays of CNTs are dissolved in an acid to form a spinnable liquid dope that is extruded through a spinneret into coagulant bath to remove acid, and then dried in an oven. The resulting product is highly aligned and densely packaged CNTs in a form of a fiber. DexMat fibers have high electrical and thermal conductivity. Such fibers were shown to feature anisotropic field emission [19] that is emission takes place along the fiber (not from side walls) which is a great property allowing for control over emittance. Raman spectroscopy shows the G peak positions at 1583 cm<sup>-1</sup> suggesting rich crystalline graphitic content as expected from high quality fibers (Fig.4.2A).

To mitigate the described stray fibril problem, a few fibers of the described kind were placed side by side and electroplated with Ni in an electrochemical bath and flush cut from the top to the required length of about 5 mm with a femtosecond micromachining laser beam. Then, it was welded on  $1 \times 1$  inch Ni base. The final fabricated structure can be seen in Fig.4.2B.

We tested two samples referred to as Sample A and Sample B through the rest of the paper. In

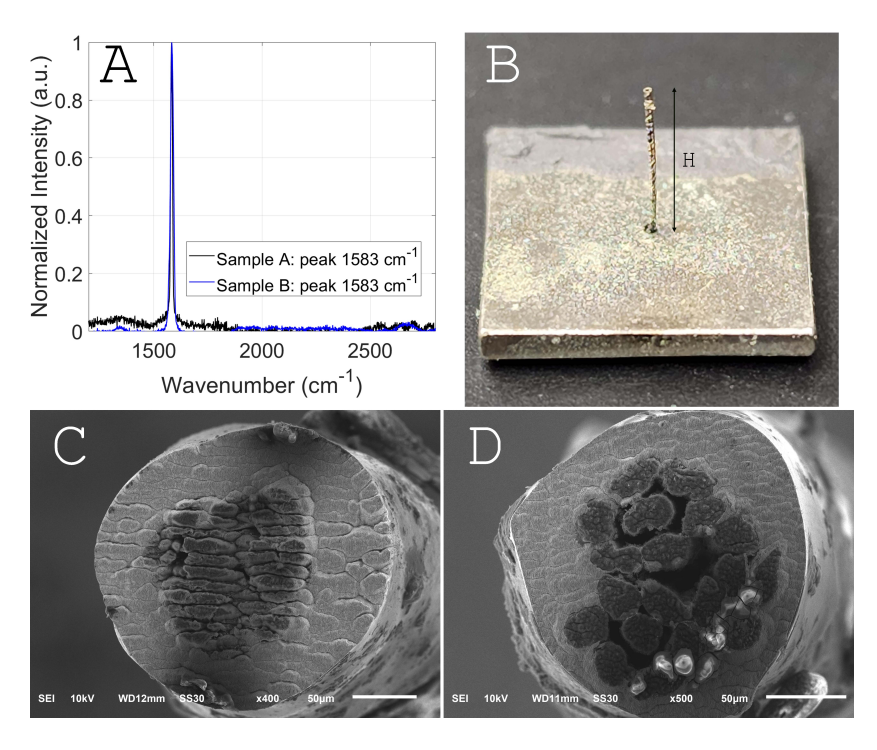


Figure 4.2 (A) Raman spectra of the cathode surface showing a crystalline graphitic peak. (B) Electroplated CNT fiber welded on a Ni base; H=4.8 mm for Sample A and H=4.6 mm for Sample B. (C) and (D) SEM images of Sample A and Sample B, where scale bars are 50  $\mu$ m.

Sample A fibers were twisted and in Sample B were not, i.e. simply place along each others. As scanning electron microscopy (SEM) demonstrates in Fig.4.2C, additional fiber twisting enabled a dense core in Sample A, while Sample B (Fig.4.2D) has visible voids between the individual fibers. Otherwise, both sample have fiber core diameter of  $\sim 150 \, \mu \text{m}$  and Ni shell thickness of  $\sim 50 \, \mu \text{m}$ . Sample A and Sample B have height of 4.8 mm and 4.6 mm respectively (see Fig.4.2B).

DC current tests and field emission microscopy were performed in our custom field emission microscope described in great detail in Ref.[1]. The illustration of the test setup is given in Fig.4.3. Images were processed by a custom image processing algorithm FEpic described elsewhere [89].

# 4.3 Field Emission Imaging and Conditioning

After the sample was installed and the gap was tuned using two orthogonal optical microscopes, the physical location of the fiber was determined and labeled. To do that, the test chamber was illuminated. Because the imaging anode YAG screen is semitransparent, the location of the fiber can be immediately seen and captured by photographing. The core of the fiber was marked with a

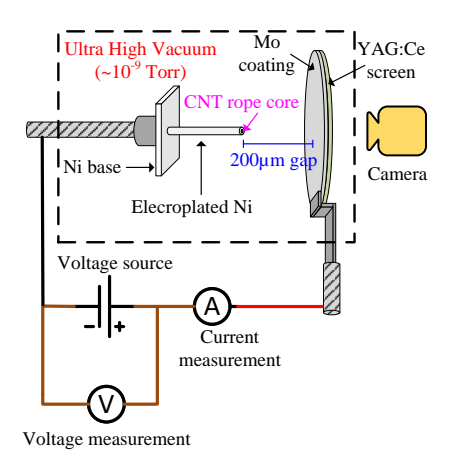


Figure 4.3 This is an illustration of the measurement setup. The coated fiber cathode was mounted across a scintillator anode screen made of yttrium aluminum garnet (YAG). The screen was biased positively, and the cathode and body of the vacuum chamber were grounded. The emitted electrons, under the applied field, struck the screen, which formed emission micrographs. The micrographs were captured by a camera behind the screen. The emission current and feedback voltage were recorded. All data acquisition was done synchronously and automatically by computer control.

red circle for reference in Figs.4.4A and 4.5A.

After that voltage was applied and field emission images were taken concurrently with I-V curves. Fig.4.4B shows an emission micrograph of Sample A. The improvement is immediately obvious when compared with Fig.4.1. First, the emission spot appears exactly at the optical projection of the cathode. This means the beam divergence angle is small, so emittance can be expected to be low. Second, there is only a single spot and its size is comparable to the size of the fiber core—this is an indication of uniformity and small angular spread of the electron beam. The same exact behavior was observed for Sample B, as given in Fig.4.5. No evidence suggesting the stray fibril issue was observed for either cathode. These results highlight that such a simple electroplating strategy is extremely effective at yielding emission uniformity and spatial coherence, thereby boosting the transverse beam brightness.

Fig.4.6 shows cathode conditioning I-V curves for Sample A and B at the interelectrode gap of 200  $\mu$ m. Conditioning [45, 47, 90] or cycling, where the applied voltage is ramped up and down to a progressively higher number in every consecutive cycle until the desired operating current is achieved, is a crucial procedure to maximize field emission cathode performance and ensure

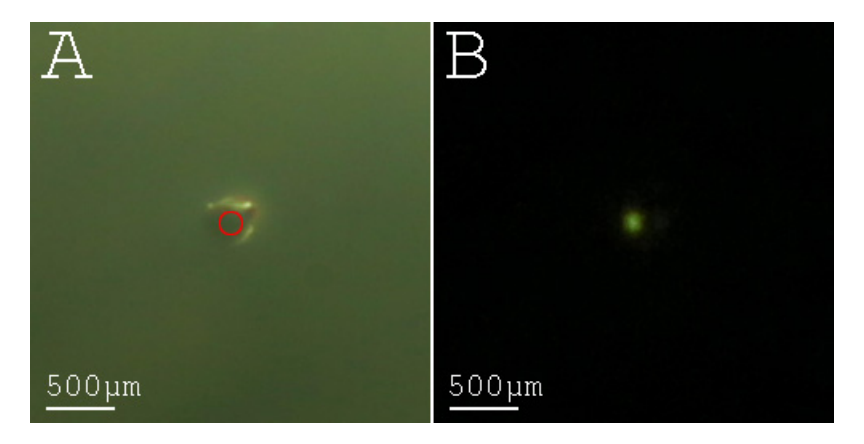


Figure 4.4 A) Sample A seen through the YAG screen when the lights are on in the chamber. Its fiber core is marked with a red circle (the shiny gray region is the metal shell, and the darker center is the core). B) FE micrograph of the same region at the gap of  $200 \,\mu\text{m}$ .

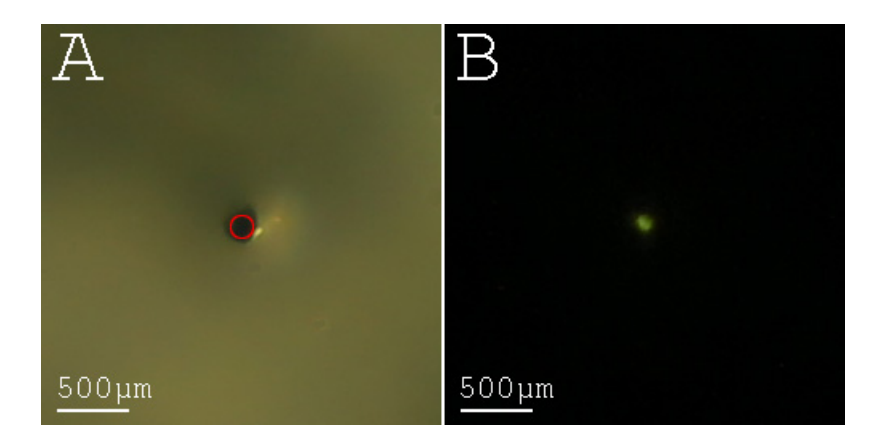


Figure 4.5 A) Sample B seen through the YAG screen when the lights are on in the chamber. Its fiber core is marked with a red circle. B) FE micrograph of the same region at the gap of  $200 \,\mu\text{m}$ .

stability at the operating point.

We found that the electroplated fibers should be conditioned with small incremental steps to avoid adverse effects such as sudden burn-down. Fig.4.6A demonstrates the case where the maximal field was doubled with respect to the previous conditioning cycle, such that the current went up from 3 to 22  $\mu$ A. Next, after completing the ramp down, Sample A stopped working completely, which was possibly due to applying electric power that exceed that in the previous run by more than an order of magnitude. Its operation could not be rejuvenated by applying higher electric fields. This is unlike a conditioning scheme that was used for Cathode B as shown in Fig.4.6B. The emission current was doubled at every conditioning cycle: up to 1  $\mu$ A and down to 0, then to 2  $\mu$ A, to 4  $\mu$ A,

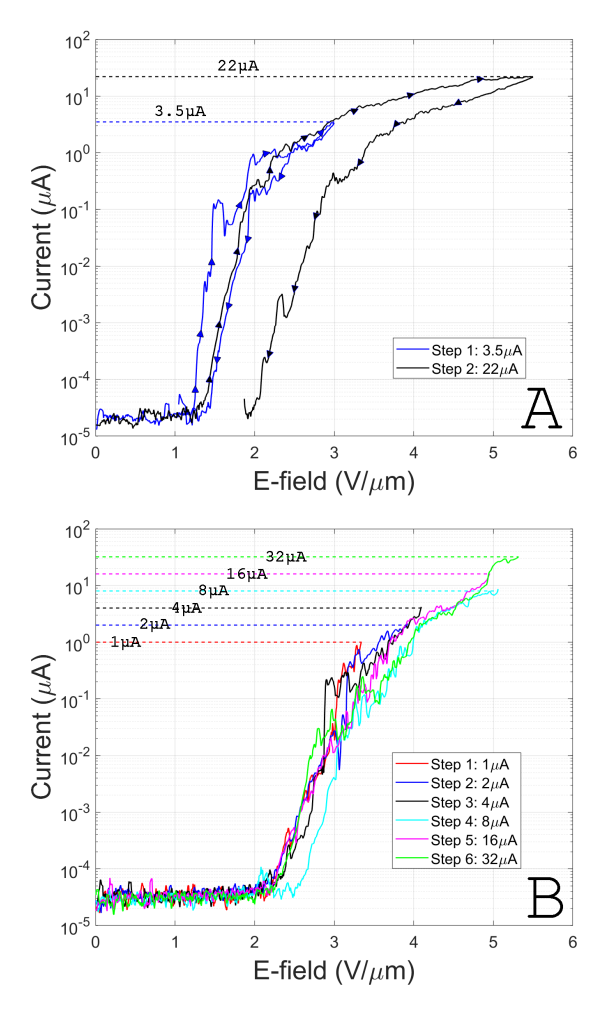


Figure 4.6 A) The conditioning scheme of Sample A. Both ramp up and down curves are shown. There is a clear decrease in performance. B) Conditioning scheme of Sample B. Only ramp-up curves are shown. There is no considerable change in performance.

to 8  $\mu$ A, to 16  $\mu$ A, and finally to 32  $\mu$ A. By doing so, Cathode B was conditioned *softly* (compared to Sample A) maintaining and enhancing its performance: i) the resulting operating field went up and doubled, reaching the same exact value where Cathode A burned down; ii) turn-on field and field enhancement factor remained nearly the same meaning that Cathode B was conditioned to stably sustain a higher local field.

When it is compared to our past cathode designs, detailed in Ref.[45], they emit less at any given field. This is an expected result because (with stray fibrils mitigated) the field enhancement is reduced. However, turn-on fields are still very low, between 1 and 2.5 V/ $\mu$ m. Because the beam was tight suggesting high current density we limited our measurements to between  $10-100 \,\mu\text{A}$  as the

power density deposition at the imaging screen could attain above  $1 \,\mathrm{kW/cm^2}$  at the voltage source limit of  $1100 \,\mathrm{V}$ , thereby literally drilling holes in it [91, 92]. At  $1100 \,\mathrm{V}$ , Sample A maxed out at  $20 \,\mu\mathrm{A}$  and Sample B  $30 \,\mu\mathrm{A}$ , respectively. Again both cathodes had similar metrics. Having these metrics and qualitative results in mind, a step was taken to carry out more quantitative analysis and calculate cathode emittance and brightness as detailed in the next section.

## 4.4 Emittance and Brightness

In the phase space, (x, x'), x is spatial position and  $x' = \frac{dx}{dz} = \frac{dx/dt}{dz/dt} = \frac{v_x}{v_z}$  is the slope of the trajectory from the longitudinal centrosymmetric axis of each particle. Then, rms emittance  $\tilde{\epsilon}_x$  is defined as

$$\tilde{\epsilon}_x = \sqrt{\langle \Delta x^2 \rangle \langle \Delta x'^2 \rangle - \langle \Delta x \Delta x' \rangle} \tag{4.1}$$

where  $\Delta x = x - \langle x \rangle$  and  $\Delta x' = x' - \langle x' \rangle$ . For a beam with cylindrical symmetry in (x, y) and (x', y') centered around zero,  $\langle x \rangle$  and  $\langle x' \rangle$  are zero. The cross-correlation term,  $\langle \Delta x \Delta x' \rangle$  can be removed with proper beam optics [4]. Then, Eq.4.1 reduces to

$$\tilde{\epsilon}_x = \sqrt{\langle x^2 \rangle \langle x'^2 \rangle} = \sigma_x \sqrt{\langle x'^2 \rangle} \tag{4.2}$$

Rms emittance is a function of the beam energy as x' is changing under acceleration, and is not useful while comparing beam or beams at different energies. On the other hand, from Liouville's theorem, normalized emittance is a conserved quantity under acceleration as long as the beam is only subjected to conservative forces. The relation between rms emittance and normalized emittance is given by

$$\epsilon_x^{\rm N} = \gamma \,\beta \,\tilde{\epsilon}_x \tag{4.3}$$

where  $\gamma = \frac{1}{\sqrt{1-\beta^2}}$  is the Lorentz factor and  $\beta = \frac{v}{c} \approx \frac{v_z}{c}$ . In our case,  $\gamma \approx 1$  because energy is <=1 keV. Mean-transverse energy, MTE, is  $\frac{1}{2} \text{m}_e \langle v^2 \rangle$ , where  $v^2 = v_x^2 + v_y^2$ . Because of the cylindrical symmetry in  $(v_x, v_y)$ , MTE  $\approx \frac{1}{2} \text{m}_e \langle 2v_x^2 \rangle = \text{m}_e \langle v_x^2 \rangle$ . Then, after substituting Eq.4.2, in terms of MTE, Eq.4.3 becomes

$$\epsilon_x^{\rm N} = \frac{v_z}{\rm c} \, \sigma_x \, \sqrt{\langle \frac{v_x^2}{v_z^2} \rangle} = \sigma_x \, \sqrt{\frac{\rm MTE}{\rm m_e c^2}}$$
 (4.4)

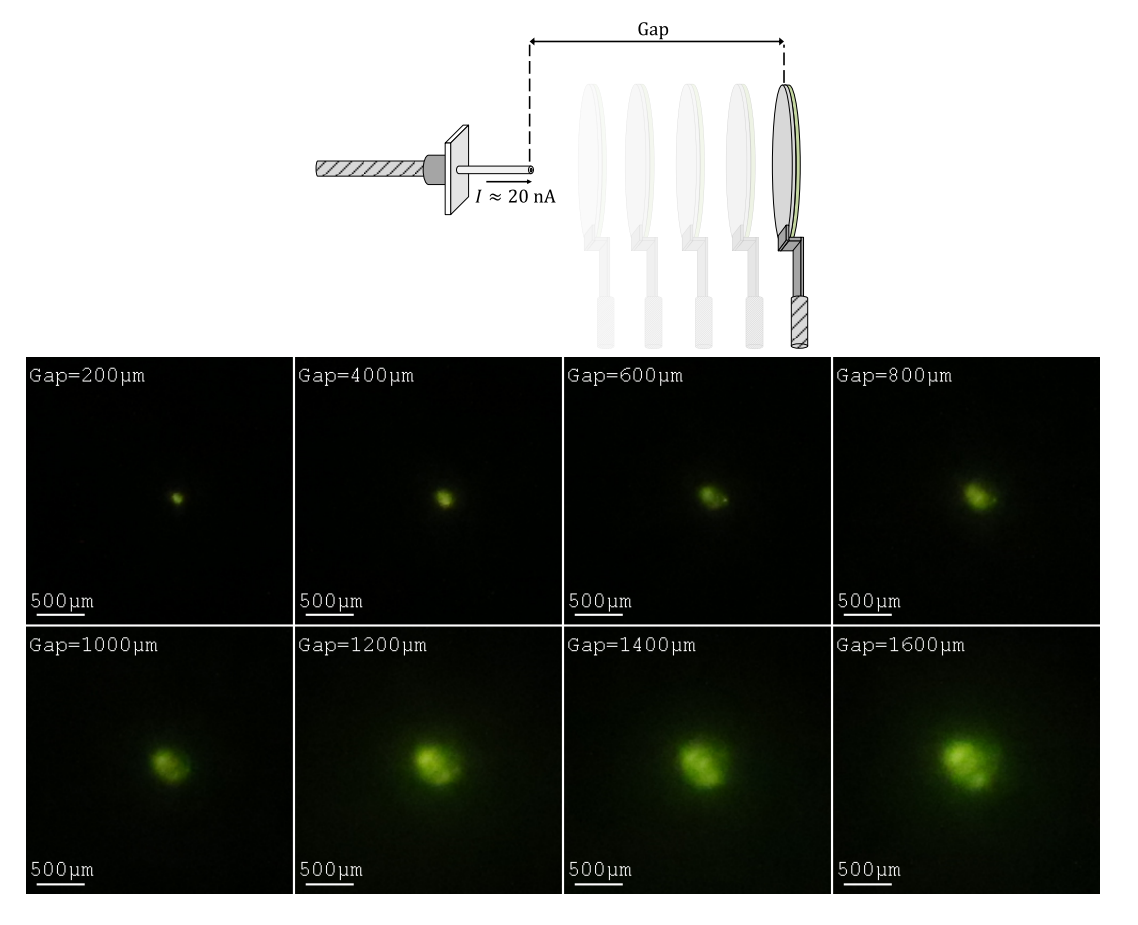


Figure 4.7 Series of field emission micrographs of Sample B with the screen moved away progressively from  $200 \,\mu\text{m}$  gap to  $1600 \,\mu\text{m}$  gap with  $200 \,\mu\text{m}$  steps. At each step, a micrograph is captured.

Practically, the normalized emittance at the cathode surface is calculated as follows. If the radius of the uniformly emitting surface of the cathode is  $r_i$ ,  $\sigma_x \approx r_i$  can be taken. Moreover, at the surface, MTE is due to the statistical distribution of electrons inside the cathode itself. So, it is intrinsic and is further redefined as MTE<sub>i</sub>. Then, Eq.4.4 becomes

$$\epsilon_x^{\rm N} = r_{\rm i} \sqrt{\frac{\rm MTE_i}{\rm m_e c^2}} \tag{4.5}$$

By using normalized emittance, normalized transverse brightness,  $B_{\rm N}$ , can be calculated as

$$B_{\rm N} = \frac{2I}{\epsilon_{\rm x}^{\rm N} \epsilon_{\rm y}^{\rm N}} \tag{4.6}$$

where *I* is the emitted current.  $\epsilon_x^N = \epsilon_y^N$  can be taken in cylindrical symmetry.

To determine  $r_i$  and MTE<sub>i</sub> in Eq.4.5, we conducted experimental measurements in combination with beam dynamics in GPT (General Particle Tracer) [93]. In the measurements, the imaging screen is moved away from the cathode progressively. The voltage is set accordingly to keep the current constant at 20 nA to enable a strong beam image signal but avoid additional beam expansion due to vacuum space charge effect. A micrograph at each step is recorded (see Fig.4.7). The increase in the spot size due to the larger time of flight is measured. As it is seen in Fig.4.7, the spots are Gaussian in nature with dense centers and faint tails. Each spot can be modeled mathematically with a cylindrically symmetric Gaussian as

$$p = A \exp\left(-\frac{(x - x_c)^2 + (y - y_c)^2}{2\sigma_{\text{spot}}^2}\right) + C$$
 (4.7)

to extract the projected transverse beam size. Here, A is the amplitude,  $\sigma_{\rm spot}$  is the standard deviation, C is the background offset, p is the intensity, (x, y) are the space dimensions,  $(x_c, y_c)$  are the coordinates of the peak [89]. The model parameters A,  $\sigma_{\rm spot}$ , and C for each spot are computed with least-square fitting method. After fitting, the emission spot diameter is taken as  $2\sigma_{\rm spot}$ . An exemplary 3D fitting done by FEpic for the beam imaged at 200  $\mu$ m gap is presented in Fig.4.8; with the black mesh surface being the fitting surface. The resulting dependence of the spot size, first measured (Fig.4.7) and processed by FEpic, versus distance is shown in Fig.4.9 with black solid circles. The data in the figure is only for Sample B. Because Sample A burned down, studies similar to those presented in Fig.4.7 could not be carried out.

To calculate the phase space volume for emittance and brightness estimations and obtain  $r_i$  and MTE<sub>i</sub>, we switched to beam dynamics in GPT by comparing it with the experiment in Fig.4.7. To do that, a field map for each interelectrode gap was computed in COMSOL by solving Poisson's equation with given boundary conditions. An exemplary field distribution for a 1 mm gap is shown in Fig.4.10. Then, the field maps were imported to GPT. In GPT, the initial particle distribution in the real space (x, y) (Fig.4.11A) and momentum space  $(\beta_x, \beta_y) = (v_x/c, v_y/c)$  (Fig.4.11B) has to be set to propagate the beam. Because the cathode itself is circular, we used a circular uniform distribution with the radius  $r_i$  in position-space and the radius  $r_\beta$  in  $\beta$ -space. MTE<sub>i</sub> of the fiber is

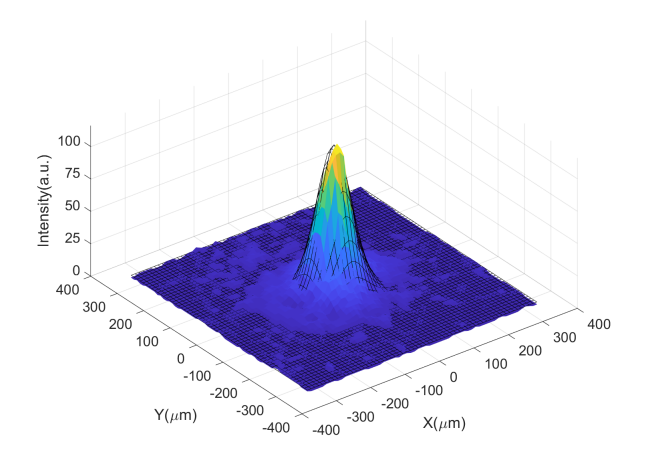


Figure 4.8 The color surface shows the beam spot for  $200 \,\mu\text{m}$  gap in 3D. The black mesh surface shows its mathematical fit in Eq.4.7.

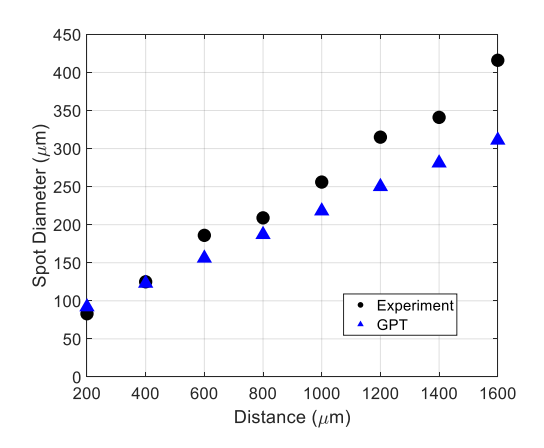


Figure 4.9 Comparison of experimental and computational final beam spot size as the screen is moving away from the cathode. MTE<sub>i</sub> of 250 meV and  $r_i$  of 75  $\mu$ m were used in GPT modeling.

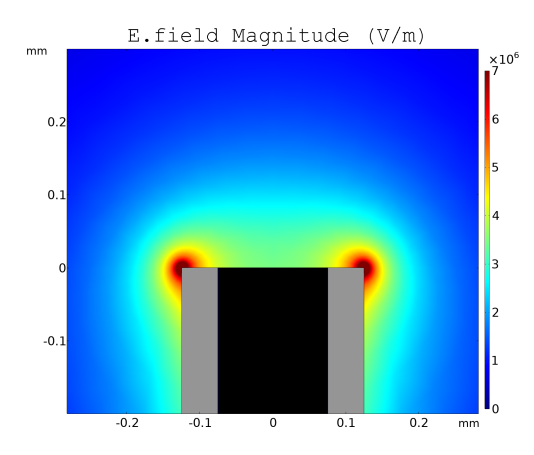


Figure 4.10 Illustration of electric field computed in COMSOL for a 1 mm gap. The color plot shows the field magnitude and contour. The dark region is the fiber core, and the gray region is the Ni shell.

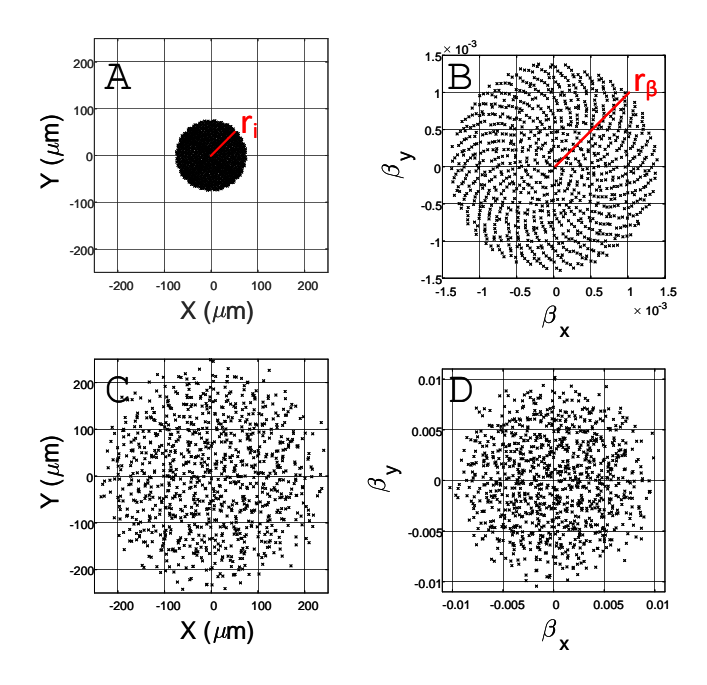


Figure 4.11 In GPT: (A) Initial uniform beam distribution at the cathode surface in real space, where  $r_i$  is the radius of the beam. (B) The initial distribution in momentum-space, where  $\beta_x = v_x/c$ ,  $\beta_y = v_y/c$ , and  $r_\beta$  is the radius. Final distribution in (C) real space and (D) momentum space when the screen is at 1 mm.

expected to be 250 meV [94]. To be used in GPT, MTE<sub>i</sub> is converted into  $r_{\beta}$  as

$$r_{\beta} = \sqrt{\frac{4 \,\mathrm{MTE_i}}{\mathrm{m_e c^2}}} \tag{4.8}$$

MTE<sub>i</sub> of 250 meV translates to  $r_{\beta}$  of  $1.4 \times 10^{-3}$ . At the same time,  $r_{i}$  remains a free model parameter to be found by finding the best agreement between GPT and the experiment.

The beam was launched at a charge corresponding to 20 nA and allowed to drift through the distance corresponding to a specified interelectrode gap. Here, the beam dynamics is computed self-consistently taking the COMSOL calculated field. The final distribution in (x, y) and  $(\beta_x, \beta_y)$  was captured at a distance corresponding to the imaging YAG screen of the microscope and are shown in Fig.4.11C and D. In the (x, y) space, the standard deviation  $\sigma_{\rm gpt}$  of such projections were calculated for every cathode-anode gap, and  $2\sigma_{\rm gpt}$  was taken as the computed beam diameter (analogous to FEpic image processing of the experimental images). It was established that in GPT, when  $r_i$  was set to the physical radius of the fiber core of 75  $\mu$ m, and  $r_\beta$  was set by MTE of 250 meV [94], then the final diameter (spot size  $2\sigma_{\rm gpt}$ ) of the resulting beam projection was

in a very good quantitative agreement with the experiments (see Fig.4.9). Note, the GPT results were fairly insensitive to MTE values set between 25 (typical Fermi level value for CNT) and 250 meV, and magnification was due to the radial field distribution. This points out that the divergence between the experiment and GPT (seen for the gap ranging between 1 and 1.6 mm) stems from the difference between the idealized computed and the actual field distribution in the gap. The summary of the results in Fig.4.9 confirms that the entire fiber surface is actively and uniformly emitting with a small MTE.

Finally, using Eq.4.5 and substituting  $r_i = 75 \,\mu\text{m}$  and MTE<sub>i</sub> = 250 eV, the upper limit of the normalized emittance on the fiber cathode surface can be estimated as

$$\epsilon_x^{\mathrm{N}} = 0.052 \,\mathrm{mm}\,\mathrm{mrad} = 52 \,\mathrm{nm} \tag{4.9}$$

From this, taking the measured current (limited to 10– $100\,\mu\text{A}$  due to extremely high power density), as shown in Fig.4.6, the normalized brightness for  $50\,\mu\text{A}$  dc current is  $B_{\rm N} = 3.7 \times 10^{10} \frac{\text{A}}{\text{m}^2\text{rad}^2}$ . The same very fibers can draw currents of 1–10 A when operated in pulsed mode with a pulse length of 100– $300\,\text{ns}$  [95]. Using the estimated emittance of  $52\,\text{nm}$  rad, the brightness in the pulsed mode, the preferable mode in most VED HPM applications, attains a notable value of  $B_{\rm N} = 4.4 \times 10^{15} \frac{\text{A}}{\text{m}^2\text{rad}^2}$ . This number is outstanding and is comparable with brightness metrics in the state-of-the-art microwave/rf accelerator injectors [96]. This (phase space) brightness can be converted into geometrical brightness, a definition of brightness commonly employed in the electron microscopy literature. The geometrical reduced brightness is defined as  $B_{\rm r}^{\rm G} = \frac{dI}{d\Omega} \frac{1}{U} \frac{1}{S_{\rm cathode}}$ , where  $\Omega$  is the solid angle, U is the voltage at which the current I is measured, and  $S_{\rm cathode}$  is the emission area of the cathode. Our calculations show that in pulsed mode it could attain  $B_{\rm r}^{\rm G} = 5.7 \times 10^7\,\text{A}\,\text{m}^{-2}\text{sr}^{-1}\text{V}^{-1}$ . This number is within the range obtained for single CNT emitters [97].

## 4.5 Conclusion

In conclusion, we presented a simple and efficient field emission cathode design where CNT fiber core was plated with a nickel shell. This design had two important functions. First, it compresses the core, and provides mechanical strength thereby preventing stray fibril formation during conditioning

and operation. Second, such a design (while slightly reducing field enhancement and increasing turn-on field) reduces the fringing field on the CNT fiber and therefore defocuses the radial field.

As field emission microscopy directly demonstrated, both tested cathodes featured excellent spatially coherent emission. Field emission microscopy aided by image processing and beam dynamics simulations confirmed that the entire fiber core of  $150\,\mu\mathrm{m}$  in diameter actively and uniformly emitted electrons, as well as enabled phase space analysis. All of these methods combined enabled quantification of the observed emission coherence through calculating emittance and brightness. The extremely low emittance resulting in record brightness highlights a simple and practical path forward for the CNT fiber technology that has long been expected to advance high-frequency vacuum power devices but had limited success due to low brightness.

Finally and most importantly, it was demonstrated that the nanoscopic single CNT cathode technology can be translated to the macroscopic fiber CNT level in terms of emission uniformity. In other words, spatial coherence and uniformity (intrinsic to a single CNT emitter) can be achieved in a CNT fiber comprised out of billions of single CNT's. The obtained brightness figures of merit further confirm this technology translation in that ultimate single CNT emitter brightness is feasible to attain for CNT fiber cathodes.

#### **CHAPTER 5**

#### CONCLUSION AND OUTLOOK

Throughout this thesis, CNT fiber emitters were evaluated and engineered using three major criteria, 1) emittance, 2) uniformity, and 3) current saturation (see Fig.5.1, which was reproduced from Sec.1.4.3), as means to maximize the cathode brightness.

The first step was to evaluate the emitted beam characteristics of standard cathode designs and identify bottlenecks limiting their performance. To achieve this, in Ch.2, four different designs made of a fiber rope were investigated in the field emission projection microscope. The microscopy setup allowed for real-time monitoring of the spatial beam characteristics and measuring current. The observations were as follows: 1) The emission was very non-uniform regardless of the sample design. Only a handful number of localized spots were active and emitting. 2) The beam spread was very large. The beams always landed on the screen millimeters away from the origin (physical emitter location). Therefore, emittance was very high. 3) At higher applied fields, there was a considerable drop in the increase in the rate of the output current with increasing voltage. This was referred to as a saturation behavior that caused two distinct slopes to emerge in the I-V curves plotted in Fowler-Nordheim coordinates. 4) The emission patterns in the micrographs were dynamic. Spots

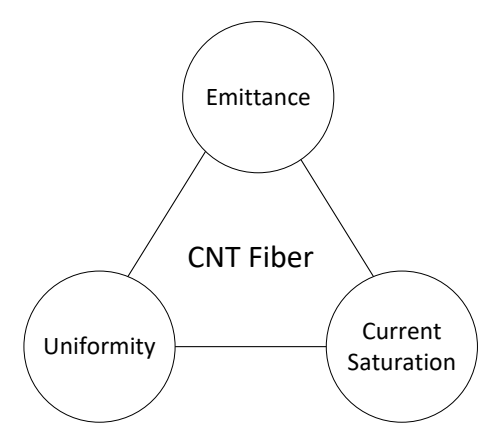


Figure 5.1 The results of this study showed that these three criteria determining brightness are interconnected. Non-uniform emission leads to a local high current density, which eventually results in current saturation, local heating, breakdowns, and unstable performance. Emission non-uniformity was caused by the formation of stray emitters, which enhanced the radial field and increased emittance as a result.

were born and annihilated during emission. There was an increase in the total number of spots as the voltage increased, which correlated with the increase in current. 5) There were instances where the pattern changed completely, which correlated with sudden spikes in voltage and current readings. In the optical microscopy images taken after the samples were tested, the occurrence of tiny and high-aspect ratio stray fibrils was observed.

The conclusion was that during emission individual building blocks comprising the fibers (individual fibrils and nanotubes) became loose and formed the stray emitters. Due to the high aspect ratio of these stray emitters, they strongly enhanced the field locally (diverting the field away from the main cathode surface) and became the dominant emission sources. Because of the high current and thus thermal load such fibrils became hot and underwent a series of micro- and macro-breakdowns. The breakdowns further promoted the formation of even more stray emitters. In some instances, this was an infinite self-inflicted process. Moreover, breakdowns and locally hot cathodes are undesirable in vacuum electron devices, as they set the system in unstable operation. The alignment of the stray fibrils was random, they enhanced the radial field as well as the normal one. The high radial field caused a large transverse spread, resulting in high emittance and low brightness. Therefore, as long as the stray emitter issue is not mitigated, cathodes made from CNT fibers cannot be practically useful.

The studies described in Ch.2 provided insights into the mechanism of current saturation in CNT fibers. The output current not being able to rise above an upper saturated limit was a main factor limiting brightness of the fiber cathodes. Therefore, studying this effect in depth could potentially offer a remedy for improving the brightness. In the literature, the saturation effect was historically associated with "external effects", most often with the vacuum space-charge effect. Indeed the space charge effect was proved to be the main cause of the saturation for metal emitters, but the metal-like treatment could be deficient for CNT fibers as CNT is a semiconductor material. The locally confined emission regions observed in Ch.2 led to formulate a hypothesis that the current density reaching saturation could be caused by the finite number of carriers moving along the near-surface depletion region at saturated drift velocity. In other words, the current, being

the ratio between the charge and time, could be restricted due to limited charge traveling at finite transit-time.

Ch.3 was dedicated to testing of this hypothesis. To achieve this goal, the experimental current density had to be evaluated. A computer vision algorithm was developed in Ch.3 to extract the emission area from the experimentally measured micrographs. It was able to produce accurate results by mitigating various sources of background contamination. To map the emission area on the algorithm-processed micrographs to the actual emission area on the cathode, the magnification factor due to the mean transverse energy (MTE) of emitted electrons was taken into account. Finally, the upper and lower limits of the experimental current density were determined as functions of the applied electric field. The results were compared with the current densities calculated in the framework of canonical 1) Fowler-Nordheim (FN) and 2) Murphy-Good (MG) formulations, and 3) space-charge limited emission model, as well as with 4) the newly proposed transit-time limited emission model.

The conclusions were as follows: 1) The experimental current density remained constant as the field increased. The emission area was linearly dependent on the output current as the field increased. 2) Both FN and MG formulations failed to explain the experimental data, which further corroborated the fact that canonical metal-centric field emission models are not applicable to non-metals. 3) The upper saturated limit of the experimental current density was two orders of magnitude lower than that predicted by the Child-Langmuir model, which also ruled out the space charge effect. 4) Only the transit-time-limited emission model accurately predicted the experimental saturation current density. Although the total number of carriers in the fibers was very large, localized emission caused such a high local current density (thereby electron demand) that the electrons could not be supplied instantaneously and only could be resupplied from the bulk to the surface via transporting the charge through a depleted region. 5) Non-uniform emission was the leading cause of the saturation. In an ideal case, a uniform emission would distribute the current load evenly over the entire emitting surface, thereby preventing the saturation effect.

The results of Ch.2 and Ch.3 showed that the three criteria given in Fig.5.1 are intertwined.

Non-uniformity led to strong emission current localization causing the current saturation. Non-uniformity itself was caused by the stray emitter formation because the stray fibril emitters enhanced the transverse field causing the emittance to inflate. Therefore, the formation of stray fibril emitters was recognized as the main practical bottleneck for designing CNT fiber cathodes. Ch.4 was based on a hypothesis that mechanical support might prevent the formation of the stray emitter. Earlier attempts showed that simply placing the fibers in tight metal or quartz tubes did not work. Therefore, in Ch.4, the chosen method was electroplating. A few fibers were placed side-by-side, twisted, and electroplated with Ni, then the tip was cut with a femtosecond laser. The samples were tested in the same field emission microscope. The observations were as follows: 1) The samples produced single uniform emission spots right on the optical axis suggesting that emittance and brightness greatly improved, as compared to the earlier designs. 2) No formation of stray emitters was observed under an optical microscope upon completing the emission experiments.

Additional experiments coupled with detailed electrostatics and beam dynamics simulations revealed that 1) The whole cathode surface actively and uniformly emitted electrons at all times. 2) The current density (and apparent brightness) was so high that the output current had to be kept to less than  $100 \mu A$  not to damage the imaging screen. 3) The small spot size outgrowth was due to the radial electric field defined by the geometry of the cathode, with little to no effect due to MTE.

To evaluate the limitation of the new cathode design in terms of current, the sample was conditioned carefully. It was observed that the emission current was lower at any given voltage as compared to the old designs, which was expected because of the absence of stray emitters. However, because the emittance was thousands of times better, the cathode brightness was strikingly better. It was concluded that electroplating the fibers is a very effective yet simple way to suppress stray fibers and achieve a brightness level of practical interest. This result marked an important milestone in the history of CNT-based field emitters, as exceptional low emittance characteristics of single CNTs had never been translated to large area CNT fiber emitters before. This translation was necessary to meet the drive beam requirements in many technologies.

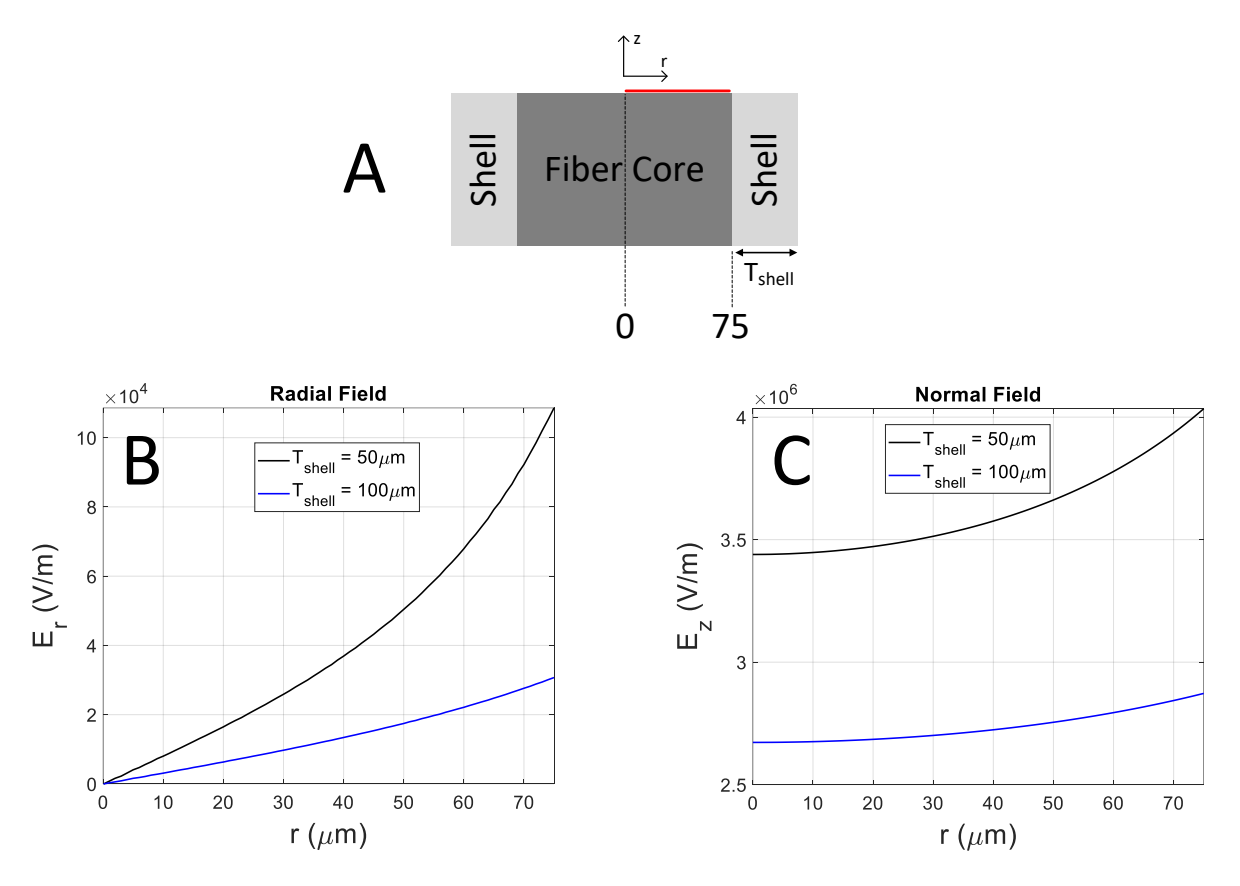


Figure 5.2 The plots show the radial and normal surface fields right above the cathode for different Ni shell thicknesses. A) The solid red line indicates the line where the fields were plotted, which extends from the center axis to the edge of the fiber core.  $T_{\text{shell}}$  represents the thickness of the Ni shell. B) It shows the radial field  $E_r$  over the surface, with r denoting the distance from the center axis of the fiber. Doubling the shell thickness results in a five-fold decrease in the radial field  $E_r$  on the surface. C) It shows the normal field  $E_z$  over the surface.

## 5.1 Optimization and Final Remarks

The promising performance of the electroplated fibers was demonstrated in the thesis. However, to make practical use of the cathodes, they must also be tested in a real electron gun configuration and optimized accordingly, which is not within the scope of this thesis. The electric field distribution over the cathode will be determined by the gun design, so it will differ from the field in the field emission microscope. Hence, the cathode design must be optimized based on the gun design. This section provides information to future researchers interested in optimizing electroplated CNT fiber cathodes for electron guns.

The benefit of the electroplated shell is two-fold: i) it prevents the formation of stray emitters and

ii) decreases the effect of the fringing electric field on the cathode. Suppressing the radial fringing field is as important as suppressing stray emitters. The intrinsic emittance reported in Sec.4.4 is the ultimate emittance that can be obtained from these cathodes. The normalized emittance is conserved as long as a Hamiltonian can be defined for the system. Therefore, nonlinear effects such as space-charge and radial fringing field near the cathode surface can cause emittance growth [8]. The fringing field can be reduced to almost zero by making the shell very thick. However, there is a trade-off. The increasing shell thickness simultaneously decreases the normal field leading to an increase in the operating voltage. To keep the operating voltage reasonable, optimization must be performed. As an example, in Fig.5.2, the shell thickness of  $50 \,\mu\text{m}$  and  $100 \,\mu\text{m}$  were simulated in COMSOL, and the normal and radial fields over the emitting CNT surface were plotted for comparison. As seen in the figure, doubling the shell thickness reduced the peak radial field by about 5 times. On the other hand, the normal field decreased by only about 1.3 times, which would not significantly affect the operating voltage. If the same tested CNT fibers had a thicker shell, it could enhance the brightness thanks to the defocusing fringing field being mitigated.

### 5.2 Future Work

In this work, the cathodes were tested by placing a flat measurement screen very close to the cathode surface and parallel to it in the emission microscope. The purpose of the microscope was to observe and characterize the nature of the initial emitted beam in close proximity to the emitting surface, providing valuable information about the initial beam and emission uniformity. Electroplated fibers showed promising performance according to the microscopy results. However, further investigation is required to demonstrate their actual potential as an electron source for high-power radiation sources.

Different applications require different electron gun designs operated in DC, pulsed, or pulsed RF/microwave modes. In this work, only the DC condition was tested. To assess the applicability of electroplated cathodes in different scenarios, they must be actually tested in RF and pulsed modes. As mentioned in Sec.4.4, multiple studies have reported similar average current values for pulsed mode compared to the DC measurements conducted in this work. Therefore, it is expected that

electroplated cathodes can provide many amperes of peak current in pulsed or RF mode. In pulsed mode, the cathodes should be tested for various pulse widths, repetition rates, and peak voltages. In RF mode, they should be tested under different operating frequencies and peak voltages.

In a practical electron gun, the anode, which accelerates the emitted beam, typically has a hole or grid to allow the accelerated beam to exit the gun. The shape of the anode is optimized to ensure that the peak field occurs at the cathode surface. Therefore, the future gun geometries will differ from the parallel plate configuration used in the emission microscope. Consequently, the emittance will be a function of the gun geometry and hence will differ significantly from the reported value in this study. Actual and careful tests will be necessary to evaluate the output emittance of guns. For example, a widely employed technique to measure effective emittance is the "Pepper-Pot" technique. In this method, a drift space is introduced after the gun exit, and a grid with known hole spacing and diameter is placed down the drift space. A screen is positioned at a certain distance from the grid. The drifting electron beam passes through the grid and is projected onto the screen. By analyzing the distances between the spots on the projection image and by utilizing the known values of the gap and the grid hole spacing, the emittance can be measured. The described measurement is recommended for electroplated fibers in the future.

Lastly, the lifetime of the electroplated fibers needs to be assessed. In this study, the electroplated fibers were operated for more than 50 hours during experiments without showing degradation. However, there were time gaps between experiments, allowing sufficient time for the samples to cool down. To obtain more realistic estimations of the lifetime, future samples should be continuously operated for longer periods of time (hours to days) and in different modes, as specified.

# **BIBLIOGRAPHY**

- [1] Stanislav S. Baturin and Sergey V. Baryshev. "Electron emission projection imager". In: *Review of Scientific Instruments* 88.3 (2017), p. 033701. URL: https://doi.org/10.1063/1.4977472.
- [2] Valery Dolgashev et al. "Geometric dependence of radio-frequency breakdown in normal conducting accelerating structures". In: *Applied Physics Letters* 97.17 (2010), p. 171501. URL: https://doi.org/10.1063/1.3505339.
- [3] S. C. Leemann, A. Streun, and A. F. Wrulich. "Beam characterization for the field-emitter-array cathode-based low-emittance gun". In: *Phys. Rev. ST Accel. Beams* 10.7 (2007), p. 071302. URL: https://doi.org/10.1103/PhysRevSTAB.10.071302.
- [4] Jonathan D Jarvis. "Development of high-brightness electron sources for free-electron lasers". Ph.D. thesis. Vanderbilt University, 2009. URL: https://www.proquest.com/docview/898735436.
- [5] M. J. Rhee. "Refined definition of the beam brightness". In: *Physics of Fluids B: Plasma Physics* 4.6 (1992), pp. 1674–1676. URL: https://doi.org/10.1063/1.860076.
- [6] Soichiro Tsujino. "On the brightness, transverse emittance, and transverse coherence of field emission beam". In: *Journal of Vacuum Science & Technology B* 40.3 (2022), p. 030801. URL: https://doi.org/10.1116/6.0001776.
- [7] Josiah Willard Gibbs. *Elementary Principles in Statistical Mechanics*. Cambridge University Press, 2010. URL: https://doi.org/10.1017/CBO9780511686948.
- [8] K. T. McDonald and D. P. Russell. "Methods of emittance measurement". In: *Frontiers of Particle Beams; Observation, Diagnosis and Correction*. Springer Berlin, 1989, pp. 122–132. URL: https://doi.org/10.1007/BFb0018284.
- [9] B.G. Streetman and S. Banerjee. *Solid State Electronic Devices*. 7th ed. Pearson, 2015. URL: https://books.google.com/books?id=-nnznQEACAAJ.
- [10] D.R. Hamilton et al. *Klystrons and Microwave Triodes*. McGraw-Hill, 1948. URL: https://books.google.com/books?id=eW8hAAAMAAJ.
- [11] A.S. Gilmour. *Klystrons, Traveling Wave Tubes, Magnetrons, Crossed-field Amplifiers, and Gyrotrons*. Artech House, 2011. URL: https://books.google.com/books?id=l\_1egQKKWe4C.
- [12] A Delâge and PB Sewell. "Study of space charge limitation of thermionic cathodes in triode guns". In: *Scanning Electron Microscopy* 3.1 (1984), p. 17. URL: https://digitalcommons.usu.edu/electron/vol3/iss1/17/.

- [13] Russell H. Varian and Sigurd F. Varian. "A High Frequency Oscillator and Amplifier". In: *Journal of Applied Physics* 10.5 (1939), pp. 321–327. URL: https://doi.org/10.1063/1. 1707311.
- [14] Evgeny L. Saldin, Evgeny A. Schneidmiller, and Mikhail V. Yurkov. *The Physics of Free Electron Lasers*. Springer Berlin, 2000. URL: https://doi.org/10.1007/978-3-662-04066-9.
- [15] G. Margaritondo and Primoz Rebernik Ribic. "A simplified description of X-ray free-electron lasers". In: *Journal of Synchrotron Radiation* 18.2 (2011), pp. 101–108. URL: https://doi.org/10.1107/S090904951004896X.
- [16] C.W. Roberson and B. Hafizi. "Wavelength and emittance requirements in free-electron lasers". In: *IEEE Journal of Quantum Electronics* 27.12 (1991), pp. 2508–2511. URL: https://doi.org/10.1109/3.104126.
- [17] Takio Tomimasu. "What limits the wavelength of an FEL? Challenge at the shortest wavelength lasing limit of linac-based FELs using the FELI linac with a thermionic gun". In: *Nuclear Instruments and Methods in Physics Research* 393.1 (1997), pp. 230–233. URL: https://doi.org/10.1016/S0168-9002(97)00479-8.
- [18] Natnael Behabtu et al. "Strong, Light, Multifunctional Fibers of Carbon Nanotubes with Ultrahigh Conductivity". In: *Science* 339.6116 (2013), pp. 182–186. URL: https://doi.org/10.1126/science.1228061.
- [19] S. B. Fairchild et al. "Strongly anisotropic field emission from highly aligned carbon nanotube films". In: *Journal of Applied Physics* 129.12 (2021), p. 125103. URL: https://doi.org/10.1063/5.0038937.
- [20] M. Cahay et al. "Hysteresis during field emission from chemical vapor deposition synthesized carbon nanotube fibers". In: *Applied Physics Letters* 105.17 (2014), p. 173107. URL: https://doi.org/10.1063/1.4900787.
- [21] Y. Feng and J. P. Verboncoeur. "Transition from Fowler-Nordheim field emission to space charge limited current density". In: *Physics of Plasmas* 13.7 (2006), p. 073105. URL: https://doi.org/10.1063/1.2226977.
- [22] Don Shiffler et al. "Demonstration of an Acid-Spun Single-Walled Nanotube Fiber Cathode". In: *IEEE Transactions on Plasma Science* 40.7 (2012), pp. 1871–1877. URL: https://doi.org/10.1109/TPS.2012.2195328.
- [23] Alan J. Theiss et al. "High-Average-Power W-band TWT Development". In: *IEEE Transactions on Plasma Science* 38.6 (2010), pp. 1239–1243. URL: https://doi.org/10.1109/TPS. 2010.2041794.
- [24] S S Dhillon et al. "The 2017 terahertz science and technology roadmap". In: Journal

- of Physics D: Applied Physics 50.4 (2017), p. 043001. URL: https://doi.org/10.1088/1361-6463/50/4/043001.
- [25] S.M. Lewis et al. "Design of a High Gradient THz-Driven Electron Gun". In: *Proc.* 10th International Particle Accelerator Conference (IPAC'19). JACoW Publishing, 2019, pp. 2098–2100. URL: https://doi.org/10.18429/JACoW-IPAC2019-TUPTS077.
- [26] Steven B. Fairchild et al. "Carbon Nanotube Fiber Field Emission Array Cathodes". In: *IEEE Transactions on Plasma Science* 47.5 (2019), pp. 2032–2038. URL: https://doi.org/10.1109/TPS.2019.2900219.
- [27] D. Shiffler et al. "Carbon velvet field-emission cathode". In: *Review of Scientific Instruments* 73.12 (2002), pp. 4358–4362. URL: https://doi.org/10.1063/1.1516853.
- [28] D. Shiffler et al. "Emission uniformity and emission area of explosive field emission cathodes". In: *Applied Physics Letters* 79.18 (2001), pp. 2871–2873. URL: https://doi.org/10.1063/1.1415408.
- [29] Dmitri E. Tsentalovich et al. "Influence of Carbon Nanotube Characteristics on Macroscopic Fiber Properties". In: *ACS Applied Materials & Interfaces* 9.41 (2017), pp. 36189–36198. URL: https://doi.org/10.1021/acsami.7b10968.
- [30] Xuan Wang et al. "High-Ampacity Power Cables of Tightly-Packed and Aligned Carbon Nanotubes". In: *Advanced Functional Materials* 24.21 (2014), pp. 3241–3249. URL: https://doi.org/10.1002/adfm.201303865.
- [31] Peng Zhang et al. "Temperature Comparison of Looped and Vertical Carbon Nanotube Fibers during Field Emission". In: *Applied Sciences* 8.7 (2018). URL: https://doi.org/10.3390/app8071175.
- [32] S B Fairchild et al. "Morphology dependent field emission of acid-spun carbon nanotube fibers". In: *Nanotechnology* 26.10 (2015), p. 105706. URL: https://doi.org/10.1088/0957-4484/26/10/105706.
- [33] Stanislav S Baturin, Tanvi Nikhar, and Sergey V Baryshev. "Field electron emission induced glow discharge in a nanodiamond vacuum diode". In: *Journal of Physics D: Applied Physics* 52.32 (2019), p. 325301. URL: https://doi.org/10.1088/1361-6463/ab2183.
- [34] George Fursey. Field Electron Emission from Metals. Springer US, 2005. URL: https://doi.org/10.1007/b139052.
- [35] Oksana Chubenko et al. "Locally Resolved Electron Emission Area and Unified View of Field Emission from Ultrananocrystalline Diamond Films". In: *ACS Applied Materials & Interfaces* 9.38 (2017). PMID: 28862838, pp. 33229–33237. URL: https://doi.org/10.1021/acsami.7b07062.

- [36] Ville Satopaa et al. "Finding a "Kneedle" in a Haystack: Detecting Knee Points in System Behavior". In: 31st International Conference on Distributed Computing Systems Workshops. 2011, pp. 166–171. URL: https://doi.org/10.1109/ICDCSW.2011.20.
- [37] H. Chen, V. Tagliamonti, and G. N. Gibson. "Internuclear Separation Dependent Ionization of the Valence Orbitals of I<sub>2</sub> by Strong Laser Fields". In: *Phys. Rev. Lett.* 109.19 (2012), p. 193002. URL: https://doi.org/10.1103/PhysRevLett.109.193002.
- [38] Richard G. Forbes. "The Murphy–Good plot: a better method of analysing field emission data". In: *Royal Society Open Science* 6.12 (2019), p. 190912. URL: https://doi.org/10.1098/rsos.190912.
- [39] Stanislav S Baturin, Alexander V Zinovev, and Sergey V Baryshev. "Current saturation in nonmetallic field emitters". In: *arXiv* 1710.03692 (2017). URL: https://doi.org/10.48550/arXiv.1710.03692.
- [40] O. Chauvet et al. "Magnetic anisotropies of aligned carbon nanotubes". In: *Phys. Rev. B* 52.10 (1995), R6963–R6966. URL: https://doi.org/10.1103/PhysRevB.52.R6963.
- [41] David Estrada et al. "Reduction of hysteresis for carbon nanotube mobility measurements using pulsed characterization". In: *Nanotechnology* 21.8 (2010), p. 085702. URL: https://doi.org/10.1088/0957-4484/21/8/085702.
- [42] B. Gao et al. "Four-Point Resistance of Individual Single-Wall Carbon Nanotubes". In: *Phys. Rev. Lett.* 95.19 (2005), p. 196802. URL: https://doi.org/10.1103/PhysRevLett.95.196802.
- [43] A. F. Yatsenko. "On a model of photo-field-emission from p-type semiconductors". In: *physica status solidi* (a) 1.2 (1970), pp. 333–348. URL: https://doi.org/10.1002/pssa. 19700010218.
- [44] J. W. Luginsland, A. Valfells, and Y. Y. Lau. "Effects of a series resistor on electron emission from a field emitter". In: *Applied Physics Letters* 69.18 (1996), pp. 2770–2772. URL: https://doi.org/10.1063/1.117670.
- [45] Taha Y. Posos et al. "Field emission microscopy of carbon nanotube fibers: Evaluating and interpreting spatial emission". In: *Journal of Vacuum Science & Technology B* 38.2 (2020), p. 024006. URL: https://doi.org/10.1116/1.5140602.
- [46] Jiahang Shao et al. "In Situ Observation of Dark Current Emission in a High Gradient rf Photocathode Gun". In: *Phys. Rev. Lett.* 117.8 (2016), p. 084801. URL: https://doi.org/10.1103/PhysRevLett.117.084801.
- [47] Jiahang Shao et al. "High power conditioning and benchmarking of planar nitrogen-incorporated ultrananocrystalline diamond field emission electron source". In: *Phys. Rev. Accel. Beams* 22.12 (2019), p. 123402. URL: https://doi.org/10.1103/PhysRevAccelBeams.22.123402.

- [48] J. B. Cui and J. Robertson. "Field emission from chemical vapor deposition diamond surface with graphitic patches". In: *Journal of Vacuum Science & Technology B* 20.1 (2002), pp. 238–242. URL: https://doi.org/10.1116/1.1434972.
- [49] Eugeni O. Popov et al. "Local current–voltage estimation and characteristization based on field emission image processing of large-area field emitters". In: *Journal of Vacuum Science & Technology B* 36.2 (2018), p. 02C106. URL: https://doi.org/10.1116/1.5007006.
- [50] S. A. Lyashenko et al. "Field electron emission from nanodiamond". In: *Technical Physics Letters* 35 (2009), pp. 249–252. URL: https://doi.org/10.1134/S106378500903016X.
- [51] Pavel Serbun et al. "Stable field emission of single B-doped Si tips and linear current scaling of uniform tip arrays for integrated vacuum microelectronic devices". In: *Journal of Vacuum Science & Technology B* 31.2 (2013), 02B101. URL: https://doi.org/10.1116/1.4765088.
- [52] R. Schreiner et al. "Field emission from surface textured extraction facets of GaN light emitting diodes". In: 26th International Vacuum Nanoelectronics Conference (IVNC). 2013, pp. 1–2. URL: https://doi.org/10.1109/IVNC.2013.6624721.
- [53] F.A.M. Köck, J.M. Garguilo, and R.J. Nemanich. "Direct correlation of surface morphology with electron emission sites for intrinsic nanocrystalline diamond films". In: *Diamond and Related Materials* 13.4 (2004), pp. 1022–1025. URL: https://doi.org/10.1016/j.diamond. 2004.01.008.
- [54] Taha Y. Posos, Oksana Chubenko, and Sergey V. Baryshev. *FEPic.* 2021. URL: https://github.com/schne525/FEPic.
- [55] R. L. Perry. "Experimental Determination of the Current Density-Electric Field Relationship of Silicon Field Emitters". In: *Journal of Applied Physics* 33.5 (1962), pp. 1875–1883. URL: https://doi.org/10.1063/1.1728850.
- [56] Kenneth A. Dean and Babu R. Chalamala. "Current saturation mechanisms in carbon nanotube field emitters". In: *Applied Physics Letters* 76.3 (2000), pp. 375–377. URL: https://doi.org/10.1063/1.125758.
- [57] Pavel Serbun. "A systematic investigation of carbon, metallic and semiconductor nanostructures for field-emission cathode applications". PhD thesis. University of Wuppertal, 2014.
- [58] Eric Minoux et al. "Achieving High-Current Carbon Nanotube Emitters". In: *Nano Letters* 5.11 (2005), pp. 2135–2138. URL: https://doi.org/10.1021/nl051397d.
- [59] C. Ducati et al. "Influence of cluster-assembly parameters on the field emission properties of nanostructured carbon films". In: *Journal of Applied Physics* 92.9 (2002), pp. 5482–5489. URL: https://doi.org/10.1063/1.1512969.

- [60] Alex Rodriguez and Alessandro Laio. "Clustering by fast search and find of density peaks". In: Science 344.6191 (2014), pp. 1492–1496. URL: https://doi.org/10.1126/science.1242072.
- [61] P.W Verbeek, H.A Vrooman, and L.J Van Vliet. "Low-level image processing by max-min filters". In: *Signal Processing* 15.3 (1988), pp. 249–258. URL: https://doi.org/10.1016/0165-1684(88)90015-1.
- [62] Debangshu Mukherjee et al. "mpfit: a robust method for fitting atomic resolution images with multiple Gaussian peaks". In: *Advanced Structural and Chemical Imaging* 6.1 (2020), p. 1. URL: https://doi.org/10.1186/s40679-020-0068-y.
- [63] Tony Lindeberg. "Feature detection with automatic scale selection". In: *International Journal of Computer Vision* 30.2 (1998), pp. 79–116. URL: https://doi.org/10.1023/A: 1008045108935.
- [64] Ralph Howard Fowler and L. Nordheim. "Electron emission in intense electric fields". In: *Proceedings of the Royal Society of London. Series A, Containing Papers of a Mathematical and Physical Character* 119.781 (1928), pp. 173–181. URL: https://doi.org/10.1098/rspa. 1928.0091.
- [65] Gongxiaohui Chen et al. "Mean transverse energy of ultrananocrystalline diamond photocathode". In: *Applied Physics Letters* 114.9 (2019), p. 093103. URL: https://doi.org/10.1063/1.5084167.
- [66] Tanvi Nikhar et al. "Evidence for Anti-Dowell-Schmerge Process in Photoemission from Diamond". In: *arXiv* 2011.00722 (2020). URL: https://doi.org/10.48550/arXiv.2011.00722.
- [67] V. Filip et al. "Modeling the electron field emission from carbon nanotube films". In: *Ultramicroscopy* 89.1 (2001), pp. 39–49. URL: https://doi.org/10.1016/S0304-3991(01) 00107-3.
- [68] Oksana Chubenko, Stanislav S. Baturin, and Sergey V. Baryshev. "Theoretical evaluation of electronic density-of-states and transport effects on field emission from n-type ultrananocrystalline diamond films". In: *Journal of Applied Physics* 125.20 (2019), p. 205303. URL: https://doi.org/10.1063/1.5085679.
- [69] J. P. Barbour et al. "Space-Charge Effects in Field Emission". In: *Phys. Rev.* 92.1 (1953), pp. 45–51. URL: https://doi.org/10.1103/PhysRev.92.45.
- [70] A. Sommerfeld and H. Bethe. "Elektronentheorie der Metalle". In: *Aufbau Der Zusammenhängenden Materie*. Handbuch der Physik 24.2. Springer Berlin, 1933, pp. 333–622. URL: https://doi.org/10.1007/978-3-642-91116-3\_3.
- [71] E. L. Murphy and R. H. Good. "Thermionic Emission, Field Emission, and the Transition

- Region". In: *Phys. Rev.* 102.6 (1956), pp. 1464–1473. URL: https://doi.org/10.1103/PhysRev.102.1464.
- [72] J. M. Houston. "The Slope of Logarithmic Plots of the Fowler-Nordheim Equation". In: *Phys. Rev.* 88.2 (1952), pp. 349–349. URL: https://doi.org/10.1103/PhysRev.88.349.
- [73] Richard G. Forbes. "Comments on the continuing widespread and unnecessary use of a defective emission equation in field emission related literature". In: *Journal of Applied Physics* 126.21 (2019), p. 210901. URL: https://doi.org/10.1063/1.5117289.
- [74] L. W. Nordheim and Ralph Howard Fowler. "The effect of the image force on the emission and reflexion of electrons by metals". In: *Proceedings of the Royal Society of London*. A 121.788 (1928), pp. 626–639. URL: https://doi.org/10.1098/rspa.1928.0222.
- [75] R. E. Burgess, H. Kroemer, and J. M. Houston. "Corrected Values of Fowler-Nordheim Field Emission Functions v(y) and s(y)". In: *Phys. Rev.* 90.4 (1953), pp. 515–515. URL: https://doi.org/10.1103/PhysRev.90.515.
- [76] Richard G. Forbes. "Simple good approximations for the special elliptic functions in standard Fowler-Nordheim tunneling theory for a Schottky-Nordheim barrier". In: *Applied Physics Letters* 89.11 (2006), p. 113122. URL: https://doi.org/10.1063/1.2354582.
- [77] Richard G. Forbes. "Comment on "Advanced field emission measurement techniques for research on modern cold cathode materials and their applications for transmission-type x-ray sources" [Rev. Sci. Instrum. 91, 083906 (2020)]". In: *Review of Scientific Instruments* 91.10 (2020), p. 107101. URL: https://doi.org/10.1063/5.0026142.
- [78] Peng Zhang et al. "Field emission from carbon nanotube fibers in varying anode-cathode gap with the consideration of contact resistance". In: *AIP Advances* 7.12 (2017), p. 125203. URL: https://doi.org/10.1063/1.5008995.
- [79] Richard G. Forbes. "The theoretical link between voltage loss, reduction in field enhancement factor, and Fowler-Nordheim-plot saturation". In: *Applied Physics Letters* 110.13 (2017), p. 133109. URL: https://doi.org/10.1063/1.4979320.
- [80] J. W. Luginsland, Y. Y. Lau, and R. M. Gilgenbach. "Two-Dimensional Child-Langmuir Law". In: *Phys. Rev. Lett.* 77.22 (1996), pp. 4668–4670. URL: https://doi.org/10.1103/PhysRevLett.77.4668.
- [81] Kenneth A. Dean and Babu R. Chalamala. "Field emission microscopy of carbon nanotube caps". In: *Journal of Applied Physics* 85.7 (1999), pp. 3832–3836. URL: https://doi.org/10.1063/1.369753.
- [82] Niels De Jonge et al. "High brightness electron beam from a multi-walled carbon nanotube". In: *Nature* 420.6914 (2002), pp. 393–395. URL: https://doi.org/10.1038/nature01233.

- [83] S. T. Purcell et al. "Hot Nanotubes: Stable Heating of Individual Multiwall Carbon Nanotubes to 2000 K Induced by the Field-Emission Current". In: *Phys. Rev. Lett.* 88 (10 2002), p. 105502. URL: https://doi.org/10.1103/PhysRevLett.88.105502.
- [84] KBK Teo et al. "Carbon nanotube technology for solid state and vacuum electronics". In: *IEE Proceedings-Circuits, Devices and Systems* 151.5 (2004), pp. 443–451. URL: https://doi.org/10.1049/ip-cds:20040408.
- [85] Yunhan Li, Yonghai Sun, and JTW Yeow. "Nanotube field electron emission: principles, development, and applications". In: *Nanotechnology* 26.24 (2015), p. 242001. URL: https://doi.org/10.1088/0957-4484/26/24/242001.
- [86] Kenneth Jensen et al. "Nanotube radio". In: *Nano letters* 7.11 (2007), pp. 3508–3511. URL: https://doi.org/10.1021/nl0721113.
- [87] YM Wong et al. "Field emission triode amplifier utilizing aligned carbon nanotubes". In: *Diamond and related materials* 14.11-12 (2005), pp. 2069–2073. URL: https://doi.org/10.1016/j.diamond.2005.09.025.
- [88] Yong Mui Wong et al. "Characterization and CMRR modeling of a carbon-nanotube field-emission differential amplifier". In: *IEEE transactions on electron devices* 56.5 (2009), pp. 738–743. URL: https://doi.org/10.1109/TED.2009.2015418.
- [89] Taha Y. Posos, Oksana Chubenko, and Sergey V. Baryshev. "Confirmation of Transit Time-Limited Field Emission in Advanced Carbon Materials with a Fast Pattern Recognition Algorithm". In: *ACS Applied Electronic Materials* 3.11 (2021), pp. 4990–4999. URL: https://doi.org/10.1021/acsaelm.1c00789.
- [90] R. A. Millikan and Carl F. Eyring. "Laws Governing the Pulling of Electrons out of Metals by Intense Electrical Fields". In: *Phys. Rev.* 27 (1 1926), pp. 51–67. URL: https://doi.org/10.1103/PhysRev.27.51.
- [91] K Mohammed Jasim, RD Rawlings, and DRF West. "Operating regimes for laser surface engineering of ceramics". In: *Journal of materials science* 27.7 (1992), pp. 1937–1946. URL: https://doi.org/10.1007/BF01107223.
- [92] Alexandr Klimov et al. "Electron beam evaporation of alumina ceramics at forevacuum pressure range". In: *AIP Conference Proceedings* 1772.1 (2016), p. 040003. URL: https://doi.org/10.1063/1.4964562.
- [93] S. van der Geer and M. de Loos. *General Particle Tracer (Pulsar Physics)*. 2022. URL: http://pulsar.nl/.
- [94] T. C. Back et al. "Electron emission characteristics of wet spun carbon nanotube fibers". In: *AIP Advances* 9.6 (2019), p. 065319. URL: https://doi.org/10.1063/1.5098328.

- [95] Steven B. Fairchild et al. "Field Emission Cathodes Fabricated from Bulk Carbon Nanotube Fibers and Films". In: *21st International Conference on Vacuum Electronics (IVEC)*. IEEE, 2020, pp. 19–20. URL: https://doi.org/10.1109/IVEC45766.2020.9520634.
- [96] J. B. Rosenzweig et al. "Next generation high brightness electron beams from ultrahigh field cryogenic rf photocathode sources". In: *Phys. Rev. Accel. Beams* 22 (2 2019), p. 023403. URL: https://doi.org/10.1103/PhysRevAccelBeams.22.023403.
- [97] Niels de Jonge et al. "Optical Performance of Carbon-Nanotube Electron Sources". In: *Phys. Rev. Lett.* 94 (18 2005), p. 186807. URL: https://doi.org/10.1103/PhysRevLett.94.186807.